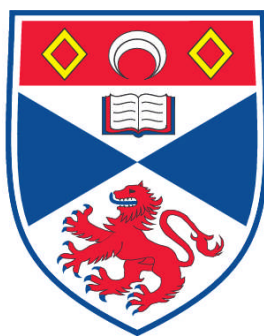


**MATERIAL CHARACTERISATION, PHASE TRANSITIONS,
ELECTROCHEMICAL PROPERTIES AND POSSIBLE FUEL CELL
APPLICATIONS OF $\text{Nd}_{2-x}\text{Pr}_x\text{CuO}_4$ AND $\text{Nd}_{2-x-y}\text{La}_y\text{Pr}_x\text{CuO}_4$
SYSTEMS**

Chami N.K. Patabendige

**A Thesis Submitted for the Degree of PhD
at the
University of St. Andrews**



2012

**Full metadata for this item is available in
Research@StAndrews:FullText
at:**

<http://research-repository.st-andrews.ac.uk/>

Please use this identifier to cite or link to this item:

<http://hdl.handle.net/10023/3181>

This item is protected by original copyright

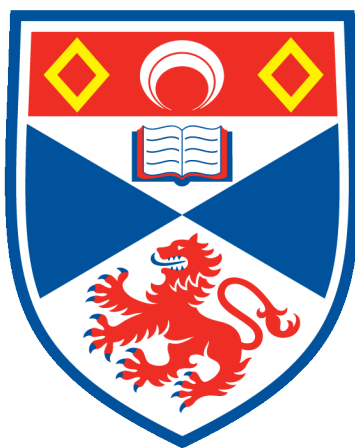
***Material characterisation, phase transitions,
electrochemical properties and possible fuel cell
applications of $\text{Nd}_{2-x}\text{Pr}_x\text{CuO}_4$ and $\text{Nd}_{2-x-y}\text{La}_y\text{Pr}_x\text{CuO}_4$
systems***

A thesis submitted for the degree of Doctor of Philosophy

by

Chami N.K Patabendige, B.Sc (Chem.Hons), AMRSC

Supervised by Prof. John T.S. Irvine



University of
St Andrews

Submitted in March 2012

Declaration

I, Chami Nilasha Kahakachchi Patabendige, hereby certify that this thesis, which is approximately 31,000 words in length, has been written by me, that it is the record of work carried out by me and that it has not been submitted in any previous application for a higher degree.

I was admitted as a research student in November 2007 and as a candidate for the degree of Ph.D in November 2008; the higher study for which this is a record was carried out in the University of St Andrews between 2007 and 2011.

Date

Signature of candidate

I hereby certify that the candidate has fulfilled the conditions of the Resolution and Regulations appropriate for the degree of Ph.D in the University of St Andrews and that the candidate is qualified to submit this thesis in application for that degree.

Date

Signature of supervisor

In submitting this thesis to the University of St Andrews we understand that we are giving permission for it to be made available for use in accordance with the regulations of the University Library for the time being in force, subject to any copyright vested in the work not being affected thereby. We also understand that the title and the abstract will be published, and that a copy of the work may be made and supplied to any bona fide library or research worker, that my thesis will be electronically accessible for personal or research use unless exempt by award of an embargo as requested below, and that the library has the right to migrate my thesis into new electronic forms as required to ensure continued access to the thesis. We have obtained any third-party copyright permissions that may be required in order to allow such access and migration, or have requested the appropriate embargo below.

The following is an agreed request by candidate and supervisor regarding the electronic publication of this thesis:

Access to printed copy and electronic publication of thesis through the University of St Andrews.

Date

Signature of candidate

Date

Signature of supervisor

ACKNOWLEDGEMENTS

I am deeply indebted to my supervisor Prof. John T.S. Irvine for his help, encouragement, enthusiasm and great support during last three years. I couldn't have wished for a better supervisor. A big thank to the past and present members of the JTSI group for their help and advice, especially Dr Abul .K Azad, Dr Paul Connor, Dr Mark Cassidy, Dr Christian Savaniu and Dr David Miller.

Dr. Aurelie. Rolle, Prof. Rose.N. Vannier and Mrs. Laurence Burylo are acknowledged for helping with the temperature dependent X-ray diffraction experiments at UCCS, Lille, France. Thanks are also owed to Alliance: Franco-British Partnership Programme, who supported my exchange to Lille.

I also wish to express my thanks to ISIS spallation source at Rutherford Appleton Laboratory, UK for their help with my neutron diffraction studies.

I would like to thank Prof. Wuzong Zhou for his assistance and valuable discussions on TEM analysis. Thanks also go to the technical staff at the University of St. Andrews, in particular, Mrs. Sylvia Williamson for helping me with thermal analysis, Mr Ross Blackley for supporting me with the X-ray and TEM analysis and also Mrs Julie Nairn for supporting in various ways.

I am grateful to Mr. David Shepherd and Dr. Christopher D. Syme for proof reading this thesis and for invaluable suggestions. Thanks also go to Mrs. Rani Shepherd for helping me in various ways in St. Andrews.

On a personal note, I would like to thank my husband for his advice and encouragement throughout this work and my lovely daughter and son whose smiles always cheers me up. Also my parents, my brother and sisters have been invaluable in supporting me during the past three years and all of my friends in and out of chemistry for their support, friendship and guidance.

Finally, I wish to express my thanks to EPSRC and International Copper Agency for funding through the award of studentship.

Abstract

The well-known lanthanide cuprates exist in two principal forms, T and T', which behave as p-type and n-type conductors, respectively. In order to understand the structural properties and crystal chemistry from the T to T' phase, the $\text{Nd}_{1.8-x}\text{La}_x\text{Pr}_{0.2}\text{CuO}_4$ (NLPCO) system was studied varying the La substitution ratio ($0 \leq x \leq 1.8$) and then characterised using high temperature X-ray powder diffraction. From analysis of the X-ray diffraction patterns obtained at room temperature, there are clearly five distinguishable regions for the NLPCO system. They are, (1) monophasic T' solid-solution (2) two phase mixture T' + T'' (3) monophasic T'' solid-solution (4) two phase mixture T'' + O and finally (5) monophasic O phase solid-solution.

The T'' form has previously been suggested as an ordered form of T'; however here we show via high temperature X-ray diffraction studies that it is a non-transformable metastable phase formed on quenching of the T phase via an orthorhombically distorted variant. Also neutron diffraction and selected area electron diffraction (SAED) studies confirmed that the T'' phase is 4- fold Cu coordinated. The structural, magnetic and electrical properties of this NLPCO series have been investigated for the selected compositions using X-ray diffraction, magnetization measurements, thermal analysis and conductivity measurements.

The aim of the second half of this work was to discover the basic high temperature electrical characteristics of $\text{Nd}_{2-x}\text{Pr}_x\text{CuO}_4$ and investigate how this matches with those required for components on the SOFC cathode side to identify which dopant level shows highest conductivity and whether it is stable at different temperatures. The idea was to make a new concept in SOFC cathodes and current collector development, using n-type conductors instead of p- type conductors and to try to produce a high conductivity material which is

stable under the chemical and thermal stresses that exist while under load that can be used in cathode or current collector applications.

The $\text{Nd}_{2-x}\text{Pr}_x\text{CuO}_4$ (NPCO) series has been studied over a range of dopant levels ($x=0.15 - 0.25$) and maximum conductivity of 86.7 Scm^{-1} has been obtained for the composition where $x = 0.25$. Also NPCO shows n-type semiconductor behaviour which gives operational advantages when operating at mild oxygen deficiency.

AC impedance studies have been carried out on symmetrical cells to investigate the performance of NPCO as a cathode material. These studies mainly focused on polarization resistance and the activation energies of the cells. Low R_p values and low activation energies are obtained for a composite cathode compared to pure cathode material. Two configurations of NPCO as cathode materials were tested, pre-fired and in-situ fired. Pre-fired NPCO exhibited better performance than in-situ fired NPCO. Both in-situ and pre-fired current collecting NPCO still showed lowest activation energies which suggest good catalytic activity. From all of these studies, it is evident that the praseodymium doped neodymium cuprate material shows considerable promise as a potential cathode material for solid oxide fuel cell applications.

TABLE OF CONTENTS

Chapter 1- Introduction

1.0 Fuel cell	1
1.1 Solid oxide fuel cell	4
1.1.1 SOFC anode	7
1.1.2 SOFC cathode	8
1.1.3 SOFC electrolyte	11
1.1.4 SOFC interconnects	12
1.2 SOFC cathode	14
1.2.1 Perovskites for SOFC cathode	15
1.2.1.1 Lanthanum manganite cathodes	16
1.2.1.2 Other magnetite cathodes	17
1.2.1.3 Lanthanum cobaltite cathodes	17
1.2.1.4 Lanthanum ferrite cathodes	18
1.2.2 K_2NiF_4 -type materials for SOFC cathodes	18
1.2.3 Cuprates based materials for SOFC cathodes	20
1.3 Crystal chemistry of Ln_2CuO_4 structures	22
1.3.1 T' - Nd_2CuO_4 structure	25
1.3.2 T - La_2CuO_4 structure	26
1.3.3 T^* structure	28
1.3.4 T'' structure	29
1.4 Properties of La_2CuO_4 and Nd_2CuO_4 structures	30
1.5 Phase relationship and structural transition in $Nd_{2-y}La_yCuO_4$ system	31

1.6 Semiconductor material	36
1.6.1 Intrinsic semiconductors	36
1.6.2 Extrinsic semiconductors	36
1.6.3 N-type and P-type semiconductors	37
1.6.4 Fermi level and band theory for extrinsic semiconductors	37
1.7 $\text{Nd}_{2-x}\text{Pr}_x\text{CuO}_4$ system (NPCO)	39
1.8 $\text{Nd}_{1.8}\text{La}_x\text{Pr}_{0.2}\text{CuO}_4$ system (NLPCO)	40
Chapter 2- Experimental techniques and their theoretical background	42
2.0 Introduction	42
2.1 Solid state reaction method	42
2.2 X-ray diffraction	44
2.2.1 Single crystal X-ray diffraction	47
2.2.2 Powder X-ray diffraction	47
2.2.3 Rietveld refinement	49
2.2.4 FullProf software	50
2.2.5 General Structure Analysis System (GSAS)	50
2.3 Electron diffraction	50
2.4 Selected area electron diffraction	51
2.5 Scanning electron microscopy	52

2.6 Energy dispersive X-ray spectroscopy	52
2.7 Neutron diffraction	54
2.8 Thermal analysis	55
2.8.1 Differential Thermal Analysis	56
2.8.2 Differential scanning calorimetry	57
2.8.3 Thermogravimetric analysis	58
2.9 Magnetization measurement	59
2.10 Electrical measurement	62
2.10.1 Conductivity	62
2.10.2 Two point measurement (lead compensated 2 point measurement)	63
2.10.3 Four point measurement	65
2.10.4 Van der pauw measurement	67
2.11 Impedance measurement	70
2.11.1 Impedance spectroscopy	72
2.11.2 Equivalent circuit	75
2.11.3 Capacitance values	76
2.11.4 Activation energy	77
Chapter 3- Praseodymium doped Neodymium Cuprates as a cathode material	78
3.0 Introduction	78
3.1 Methods used	81

3.1.1 Characterisation of praseodymium doped neodymium copper oxide	81
3.1.2 Cathode testing	83
3.1.2.1 Pt as a current collector	83
3.1.2.2 NPCO as a current collector	85
3.2 Results and Discussions	88
3.2.1 Characterisation of praseodymium doped neodymium copper oxide	88
3.2.1.1 X-ray analysis data	88
3.2.1.2 Microstructure of the pellets	90
3.2.1.3 Two point measurement	92
3.2.1.4 Four point measurement	93
3.2.2 Cathode testing	102
3.2.2.1 Pt as current collector	103
3.2.2.2 NPCO as current collector	109
3.3 Conclusions	115

Chapter 4- Material characterisation, Structural transitions and phase relationship in La Doped $\text{Nd}_{2-x}\text{Pr}_x\text{CuO}_4$

4.0 Introduction	118
4.1 Methods used	118
4.2 Results and discussions	121
4.2.1 Phase characterization	121
4.2.1.1 Room temperature x-ray analysis	121
4.2.1.2 In situ x-ray analysis	128
4.2.2 Thermal analysis	139

4.2.3 Electrical characterization	143
4.2.4 Magnetisation measurements	147
4.3 Conclusions	149
Chapter 5- T'' non-transformable phase from quenching of La_2CuO_4 (T) type structures	
5.0 Introduction	151
5.1 Methods used	151
5.2 Results and discussions	154
5.3 Conclusions	164
Chapter 6-Conclusions	165
References	167

Abbreviations and symbols

AC-	Alternative current
AFC-	Alkaline fuel cells
CGO-	Gadolinia doped ceria
DC-	Direct current
DSC-	Differential scanning calorimetry
DTA-	Differential thermal analysis
ED	Electron diffraction
EDX-	Energy dispersive X-ray spectroscopy
FC-	Field cooled
GDC-	Gadolinia-doped ceria
GSAS-	General Structure Analysis System
HREM-	High resolution electron microscopy
ICDD-	International centre for diffraction data
IS-	Impedance spectroscopy
LEED	Low energy electron diffraction
LSC-	(La,Sr)CoO ₃
LSCF-	(La,Sr)(Co,Fe)O ₃
LSGM-	Lanthanum-strontium-gallium magnesium oxide
LSGMC-	(La,Sr) (Ga,Mg,Co)O ₃
LSM-	Strontium doped Lanthanum Manganite
MCFC-	Molten carbonate fuel cells
NLPCO-	Nd _{1.8-x} La _x Pr _{0.2} CuO ₄
NPCO-	Nd _{2.0-x} Pr _x CuO ₄
PAFC-	Phosphoric acid fuel cells

PEMFC-	Polymer electrolyte membrane fuel cell
PXRD-	Powder X-ray diffraction
RE-	Rare earth
Rp-	Polarisation resistance
SAED-	Selected area electron diffraction
ScSZ-	Scandia stabilized zirconia
SDC-	Samaria-doped ceria
SEM-	Scanning electron microscope
SOFC-	Solid oxide fuel cells
SQUID-	Superconducting quantum interference device
STA-	Simultaneous thermal analysis
TEC-	Thermal expansion co-efficient values
TEM-	Transmission electron microscope
TGA-	Thermogravimetric analysis
TPB-	Triple phase boundary
YBCO123-	$\text{YBa}_2\text{Cu}_3\text{O}_{7-y}$
YSZ-	Yttria stabilized zirconia
ZFC-	Zero field cooled

Chapter 1- Introduction

1.0 Fuel cell

From the time of the Industrial Revolution, mankind has been releasing huge amounts of carbon dioxide and other greenhouse gases into the environment through the burning of fossil fuels which have contributed to global warming. Hence many researchers have shown interest in producing energy which does not depend on fossil fuels to minimise environmental pollution. For this purpose, researchers have carried out numerous laboratory experiments to move towards environmentally friendly methods for energy production, storage and conversion without burning any fossil fuels (1-13).

The fuel cell is one such substitute technology being developed and promises to be more efficient, reliable, environmentally friendly, and cost effective. Fuel cells can operate almost continuously as long as the essential flows are maintained. Fuel cells produce electricity and heat by electrochemically combining fuel and oxidant in the presence of an electrolyte. Inside the cell, reactants flow towards the cell, and reaction products flow out of the cell. Fuel cells are different from electrochemical cell batteries as batteries consume reactant, which must be refilled and they store electrical energy chemically in a closed system. In addition to that, electrodes within a battery react and change when the battery is discharged or charged, but a fuel cell's electrodes are catalytic and reasonably stable. So long as fuel is supplied, the fuel cell will generate power continuously. It is important that it converts chemical energy into electrical energy via an electrochemical process, not a combustion process. Hence, the process is quiet, clean and highly efficient (many times more efficient than fuel burning). Also fuel cells are flexible for fuels and oxidants as a hydrogen cell uses hydrogen as fuel and oxygen as oxidant. The inputs are hydrogen and oxygen; outputs are DC power, water and heat. In practice, hydrogen is the best fuel for most applications and it is an environmentally

clean fuel. From the end of the 20th century, the motor industry has been increasingly interested in fuel cell development. This research is motivated by environmental legislation for pollution control. The motor industry's current strategy is for fuel cells to be powering millions of vehicles by 2020.

As well as hydrogen, other fuels include hydrocarbons and alcohols. Other oxidants include air, chlorine and chlorine dioxide. Some fuel cells can also use carbon monoxide and natural gas as a fuel. In these reactions, carbon monoxide reacts with water producing hydrogen and carbon dioxide, while natural gas reacts with water producing hydrogen and carbon monoxide, so these hydrogen and carbon monoxide produced can be used as fuel.

In addition to very little emissions and multi-fuel capability, there are other benefits as well, they are highly efficient, reliable, flexible, economical, scalable, durable, easy to maintain and process unique operating characteristics. As well as reducing air pollution, they may also reduce noise pollution. In addition, the waste heat from a fuel cell can be used to provide hot water for used for domestic heating. The use of fuel cells in both stationary and mobile power applications can offer significant advantages for the sustainable conversion of energy.

The basic physical structures of all fuel cells are mainly the same, and contain an electrolyte layer in contact with an anode and a cathode electrode on each side. The electrolyte provides a good physical barrier to avoid mixing of the oxidant and the fuel, while at the same time it allows for transporting ionic species between the two electrodes. The electrodes in the fuel cell are porous, and are used to increase the triple phase interface between the electrode, electrolyte and the gas/liquid, and they also separate the bulk gas phase from the electrolyte.

There are five major classes of fuel cells. Typically the classification of fuel cells depends on the type of electrolyte used, although there are many other important differences as well.

There are solid oxide fuel cells (SOFC), polymer electrolyte membrane (PEMFC), alkaline fuel cells (AFC), phosphoric acid fuel cells (PAFC) and molten carbonate fuel cells (MCFC) (14). The principle of power generation is the same for all of these fuel cells, which is that the Gibbs free energy change due to the fuel oxidation is converted to electrical energy according to the following equation :-

$$\Delta G = nFE \quad (1.1)$$

where,

ΔG = Free energy of reaction

n = Number of moles of electrons transferred in the balance equation

F = Faraday's constant, the charge on a mole of electrons=95,486 C/mol

E = Cell potential (V) under specific condition

Where the ideal efficiency,

$$\eta = \Delta G / \Delta H = (\Delta H - T\Delta S) / \Delta H \quad (1.2)$$

where,

η = Efficiency

ΔG = Gibbs free energy (in kJ)

ΔH = Enthalpy change

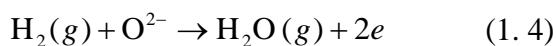
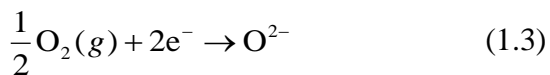
S = Entropy change (in kJ.K⁻¹)

T = Temperature (in K)

The ideal potential corresponds to the open circuit voltage if the electrolyte is an ideal ionic conductor. From the above equation, a large ideal efficiency can be obtained at low temperatures; however, it is not possible to obtain the ideal efficiency in the real fuel cell operation. This is due to the ohmic resistance of the materials, and some slow chemical reactions at electrolyte/electrode interface affect some energy losses, the result is that the actual efficiency is much lower than the ideal efficiency. As such, efficiency losses decrease with increasing temperature and high temperature fuel cells such as SOFC and MCFC have advantages in the energy conversion efficiency compared to low temperature fuel cells (14).

1.1 Solid oxide fuel cell

A solid oxide fuel cell is made entirely from solid state materials. This entire solid state ceramic construction minimises hardware corrosion, is resistant to gas crossover from one electrode to the other and also allows for flexible design shapes. The porous electrodes in SOFCs are separated by a gastight electrolyte. Electrolyte is a solid, nonporous metal oxide which contains a fast ion conductor that rapidly conducts oxide ions (O^{2-}) and allows oxygen to be transported from oxygen to a fuel rich atmosphere on the other side of the cell, when connected to an external electrical circuit. The cathode is generally an oxide material that catalyses the reduction of oxygen (1.3) and also facilitates the transport of the ionic species to the electrolyte. The anode facilitates the oxidation of the fuel, typically hydrogen or reformed hydrocarbons (1.4).



SOFC electrolytes are ionically conducting oxides. Fuel cell stacks contain an electrical interconnect, which connects single cells together in series or in parallel. Interconnects function to conduct the electrons through an external circuit. Doped lanthanum chromite or high temperature metals are commonly used materials for SOFC interconnects.

The composition of each component should be chemically and thermally compatible with each SOFC component. Many complex metal oxides containing rare earths are used as SOFC materials. The reason for this is that rare earth containing oxides have reasonably good chemical stability which are resistance to SOFC operating conditions. Also, the compositional flexibility in complex oxides with rare earth, transition metals or alkaline earth metals show many different structural arrangements such as perovskites, spinels or fluorite structures. These structures exhibit high ionic or mixed ionic conductivity (hole, electron, oxide ion or proton) or catalytic activity which is essential for SOFC operation. Several experiments and numerical investigations have been carried out to investigate the electrochemical mechanisms taking place at SOFC components and to optimise the performance of the fuel cell.

Currently, SOFC operate at relatively high temperatures of around 1000 °C, therefore high reaction rates can be achieved without using expensive catalysts, and hence they allow for highly efficient conversion to power. However, lowering the SOFC's operation temperature to about 700–800 °C is a major target in current SOFC research. Lowering the operating temperature could also offer several benefits such as reduced degradation, being able to replace ceramic interconnect with low cost metallic materials, ease of fabrication and also to minimise sealing problems (14). However, reduction of the operation temperature is sometimes unfavourable, because electrochemical processes that limit the current output of

the cell (ion transport in the electrolyte, anodic reactions and cathodic reactions etc.) are thermally activated processes and become considerably slower at low temperatures.

The ideal voltage (E^0) from a single cell under open circuit condition is close to 1.0V DC according to the Nernst equation, but the useful voltage (V) under load in real conditions, when current passes through the cell, is given by equation 1.5 (15).

$$V = E^0 - IR - \eta_a - \eta_c \quad (1.5)$$

where

I =current passing through the cell

R = Electrical resistance of the cell

η_a =Polarisation losses associated with the anode side

η_c =Polarisation losses associated with the cathode side

To minimise the IR losses, it is useful to fabricate a dense, gas tight electrolyte membrane as thin as possible (16, 17). Also, efforts to reduce the cathodic and anodic polarization resistance in SOFCs can be beneficial to overall performance.

The major components of an individual SOFC cell include the electrolyte, the cathode, and the anode. Currently used materials for these purposes are briefly described below.

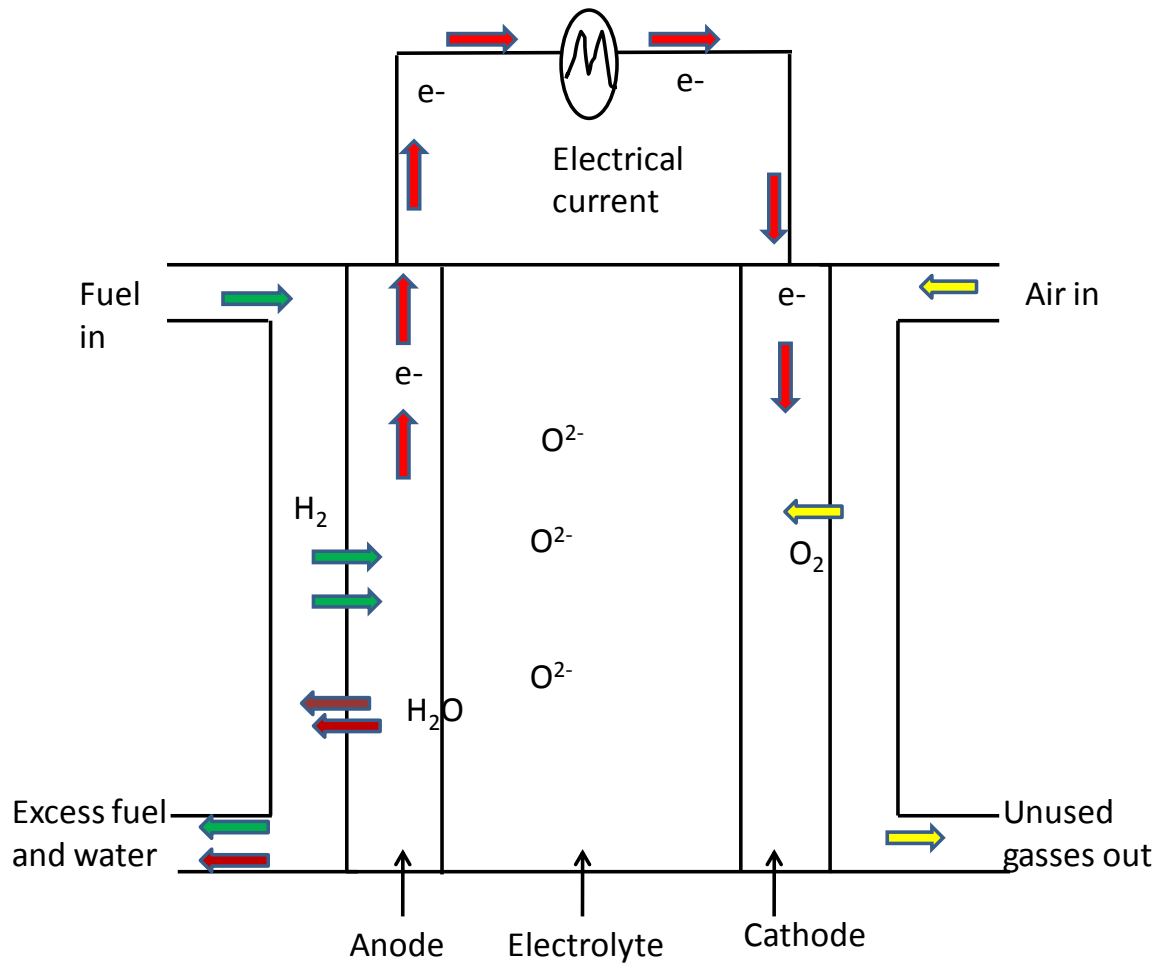


Figure 1.1: Schematic diagram of a SOFC fuel cell

1.1.1 SOFC anode

The anode facilitates the oxidation of the fuel. As shown in figure 1.1 fuel is oxidized by incoming oxygen ions which releases electrons that flow through the external circuit. Electrical conductivity, porosity, thermal expansion compatibility and the ability to function in a reducing atmosphere are the key requirements for an SOFC anode. A wide range of materials have been considered as anode materials for SOFCs (18).

The most common material for an SOFC anode is the cermets of nickel and yttria stabilized zirconia (Ni –YSZ). In Ni-YSZ cermet, YSZ has many functions such as providing structural support for separated Ni particles, preventing Ni particles from sintering while matching the thermal expansion co-efficient and enhancement of adhesion of the anode to the electrolyte (19). Also NiO-YSZ slurries are used, where NiO is reduced to Ni by a firing process. The required porosity is achieved by using pore formers such as carbon, starch or thermosetting resins. These pore formers will be burned out during the firing process while leaving pores behind. Ni –YSZ provides high catalytic activity and stability which is a more desirable quality for SOFC anode side application (20) but it has some drawbacks due to poor stability against carbon deposition. Carbon deposition by thermal decomposition of hydrocarbons is observed in actual SOFC conditions, which degrades nickel. There are other commonly used anode materials as well such as Ni-ScSZ (scandia stabilized zirconia), Ni-Ceria, etc. Again, it has similar drawbacks due to poor stability against carbon deposition and degradation is observed by nickel sintering during long term operation. Cu-cerium oxides anodes are also being studied as an alternative anode material as copper is a good electrical conductor and is compatible with cerium oxide electrolyte fuel cells but has poor catalytic activity of hydrocarbons (21).

1.1.2 SOFC cathode

The cathode facilitates the reduction of the oxygen molecule, which means, as shown in figure 1.1. oxygen reacts with incoming electrons from the external load to become oxygen ions that move through the electrolyte. The cathode has more or less the same requirements, as the anode, such as electrical conductivity, porosity, thermal expansion compatibility and additionally must be stable in an oxidizing atmosphere. The porosity is more important as it

allows oxygen molecules to reach the electrode-electrolyte interface. The mechanism at the cathode involves various chemical reaction steps.

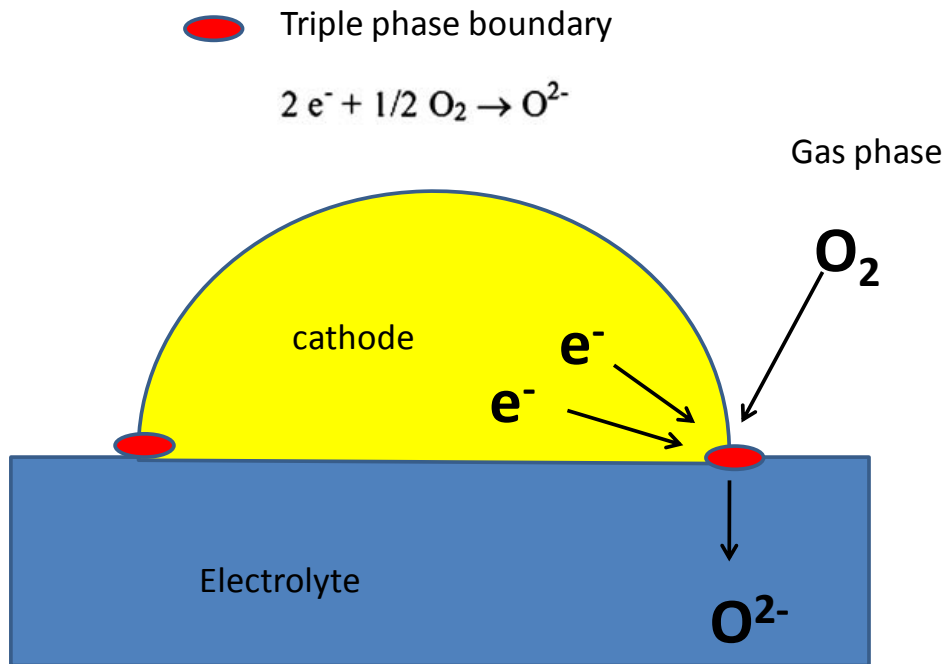


Figure 1.2: Schematic diagram for triple phase boundary

It is believed that the electrochemical reactions occur at the triple phase boundary (TPB) as shown in figure 1.2, where the oxygen ion conductor, electronic conductor, and the gas phase come into contact with each other. If there is any breakdown in the connectivity of one of these phases in the TPB, the reaction cannot take place (22). In addition to that, any barrier to access for ions, gasses or electrons to the reaction area, makes it inactive. Microstructure and composition clearly affect the size and distribution of the TPBs. The rate determining steps depend on material composition, operating conditions and microstructure.

As stated before, the choice of cathode material is a trade-off between a number of factors, such as high electrical conductivity, catalytic activity for oxygen reduction, chemical stability

with other components and low interactions with electrolyte. However the number of cathode materials has become well established within SOFC applications. At present, the most commonly used cathode material is p-type lanthanum manganite (LaMnO_3). Doping with rare earth elements (such as Sr, Ce and Pr) will improve the conductivity. The most common and well established material for this purpose is strontium doped lanthanum manganite ($(\text{La,Sr})\text{MnO}_3$) which is known as LSM. LSM has high electronic (hole) conductivity, high chemical stability in an oxidizing atmospheres at high temperatures ($\sim 1000^\circ\text{C}$), and the thermal expansion matches with YSZ (23). There are also some drawbacks with LSM, such as it forms insulating La_2ZrO_7 at the interface between YSZ and LSM, which may degrade the electrode performance (24, 25, 26).

The optimization of these materials is always a key issue to improve the performance of the fuel cell but improvement of catalytic activity for the oxygen reduction reaction is most important. There are other interesting materials under investigation e.g.; $(\text{La,Sr})(\text{Co,Fe})\text{O}_3$ (LSCF) (27), $(\text{La,Ca})\text{MnO}_3$, cobalt based oxides such as $(\text{La,Sr})\text{CoO}_3$ (LSC), SmCoO_3 , etc.

Rare earth cobaltite materials offer significant amounts of oxygen vacancies, and exhibit mixed conduction of an electron /or hole and the oxide ion, which can increase the reaction area of the cathode reaction and reduce the reaction over-potential. LSC has both high electronic conductivity and catalytic activity, however, similarly to LSM, it reacts with YSZ at SOFC operating at around 1000°C , which results in an increase of the over-potential. SmCoO_3 also offers advantages, such as high catalytic activity as well as disadvantages, such as high reactivity with YSZ and high thermal expansion.

The choice of cathode materials also depends on the electrolyte materials used, as extra care must be taken in order to match the thermal expansion coefficients and to avoid undesirable

interface reactions. Most of the La based cathode materials react with YSZ at high operating temperatures and form an insulating $\text{La}_2\text{Zr}_2\text{O}_7$ phase (28, 29, 30). Thus, lowering the operation temperature may help to avoid the formation of $\text{La}_2\text{Zr}_2\text{O}_7$ and make it possible to use a cobaltite based materials as the SOFC cathode. In SOFCs which operate at lower temperatures, around 600-700 °C, materials such as $(\text{Sm},\text{Sr})\text{CoO}_3$ (31) , $(\text{Ba},\text{La})\text{CoO}_3$ (32) and $(\text{La},\text{Sr})(\text{Fe},\text{Co})\text{O}_3$ (33) can be used as the SOFC cathode material. Due to the comparably high activation energy (often >1.5 eV) (34-39) of the oxygen reduction reaction, the cathode needs particular consideration when the operation temperature is decreased.

Most of the materials currently used for SOFC cathodes have advantages as well as disadvantages. Efforts to reduce the cathodic polarization resistance in SOFCs can be beneficial to overall performance. Therefore, it is still worth investigating new materials and to optimise current materials for better SOFC performance.

1.1.3 SOFC Electrolyte

The electrolyte is the other important component in fuel cells which facilitates the oxide ion to migrate from one electrode to the other in order to complete the electrical circuit. Electrolyte materials must have high ionic conductivity and a high transport number of ions. Oxide ion conducting metal oxides are usually used as SOFC electrolytes. Certain perovskites stabilized zirconias, conduct ions in a certain temperature range so such electrolytes could be used as oxygen ion conductors in fuel cells (40). YSZ (of 3, 8, or 10 % yttria) are the typical material currently used as SOFC electrolytes. It provides reasonable conductivity at temperatures above 700 °C while providing negligible electronic conductivity at these temperatures. YSZ has a high mechanical strength and high chemical stability over

wide range of oxygen potentials at high temperatures, and fine sinterable powders are commercially available and easy for thin preparation. However, its ionic conductivity is *ca.* 0.13 Scm^{-1} at 1000°C , which is not as high as those electrolytes in other types of fuel cell and conductivity gradually, degrades during long term operation (14). As mentioned before, most of La-based cathode materials react with YSZ and form the insulating $\text{La}_2\text{Zr}_2\text{O}_7$. But with ceria-based electrolytes such as $\text{M}_2\text{O}_3\text{-CeO}_2$ ($\text{M}=\text{Gd},\text{Sm}$), this issue is not a concern. Ceria based electrolytes offer higher ionic conductivity than YSZ (0.32 Scm^{-1} at 1000°C) with lower activation energy and can be used for low temperature SOFCs. Therefore, samaria-doped ceria (SDC) and gadolinia-doped ceria (GDC) are under consideration as SOFC electrolyte material due to their higher ionic conductivities at reduced operating temperatures (41-45). There are also some disadvantages such as mixed conduction of oxides ion and electrons causing undesirable efficiency losses and isothermal lattice expansion at the fuel side is also observed. Other materials also under investigation such as scandia-stabilized zirconia (ScSZ), $(\text{La},\text{Sr})(\text{Ga},\text{Mg},\text{Co})\text{O}_3$ (LSGMC), $(\text{La},\text{Sr})(\text{Ga},\text{Mg})\text{O}_3$ (LSGM), etc. But some of the materials (e.g. ScSZ) are not cost effective.

1.1.4 SOFC Interconnect

Several fuel cells can be used in combination in order to achieve desired voltage and current. It means that these cells need to be connected together by interconnects to the electrical contact to the cathode, while at the same time protecting it from the reducing anode atmosphere. Working in high temperature SOFC cells with a harsh environment means that interconnects must fulfil firm requirements such as pure (100%) electrical conductivity, no porosity to avoid mixing fuel and oxidant, be compatible with other SOFC materials and

exhibit thermal expansion compatibility. Interconnects are exposed simultaneously to reducing and oxidizing atmospheres.

LaCrO₃ doped with rare earth elements (Ca, Mg, Sr) are used for SOFC interconnects at operating temperature of around 1000 °C due its improved conductivity. Interconnects are usually applied to the anode by plasma spraying and then the entire cell is co-fired. The reduction of component costs (either in processing, or in raw materials) directly improve the energy affordability. Therefore the economic motivation to use the usual metals for the interconnects is leading the intermediate and low temperature SOFCs. At operating temperatures in the 900-1000 °C range, the use of interconnects made of nickel-based alloys possible (46). At or below 800 °C, ferritic steels can be used as interconnects. Below 700 °C it is possible to use readily available and cheap materials such as stainless steel (47) as interconnect materials.

Optimization of cathode, anode, electrolyte and interconnects is essential in order to achieve good electrochemical performance for SOFCs. All materials currently being used for SOFC application have some advantages as well as some disadvantages. However, there is still a need to investigate and explore new materials which may offer advantages for better performance.

1.2 SOFC cathode

In this section, we pay more attention to the SOFC cathode material as we try to optimise materials for SOFC cathode side applications. As stated before, a number of cathode materials have been researched for SOFCs and some of these materials are approaching commercial reliability. However, there is still need to explore interesting materials which may offer advantages for the performance, robustness and durability of the system. Efforts to reduce the cathodic polarization have resulted in numerous studies of a selection of different cathode materials (48, 49).

Currently, SOFC research has been focused on finding new materials to operate at lower temperature, although decreasing the temperature of the cell leads to large over-potentials, mainly associated with cathode reactions. SOFC cathodes require high electronic and ionic conductivity, good catalytic activity for oxygen reduction and good chemical and thermal compatibility with other SOFC components. Ceramics that show longer range crystallographic features such as layering may present many potentially useful properties due to defect structures which can be introduced through doping and which could result in considerable levels of ionic and electrical conductivity. Therefore, oxide-based materials which exhibit significant conductivity are of great interest for SOFC cathodes and current collector applications. In this section, SOFC cathode materials are described in more detail using different types of materials. These include commonly used conventional perovskite materials (e.g. LSM) and K_2NiF_4 -type materials (e.g. Ln_2NiO_4 where $Ln=La, Nd$ and Pr), and finally cuprate based cathode materials (electron doped Nd_2CuO_4) are considered.

1.2.1 Perovskites for SOFC cathode

A perovskite type oxide-based material has the general formula ABO_3 , where the A and B cations have a total charge of +6. Figure 1.3 shows the typical structure of cubic perovskite but most perovskite structures do not exhibit cubic structure, but are distorted. Most of these distortions (such as cation displacements in the octahedra and the tilting of the octahedron) are correlated to the properties of the A and B cations. In most of the perovskite-based SOFC cathode materials, the A site cation is a combination of rare and alkaline earths (e.g La and Sr, Ca or Ba), and the B site cation is a reducible transition metal (e.g Mn, Fe, Co, Ni). The redox catalytic mechanism is commonly given by the B site cations rather than A site cation (50). The lower valence A cations are bigger in size and they are coordinated to twelve oxygen anions while B cations reside in a smaller spaces and are coordinated to six oxygen anions. Partial substitution or full substitution of A or B cations, with different valence cations, can be achievable for ABO_3 type perovskite structures.

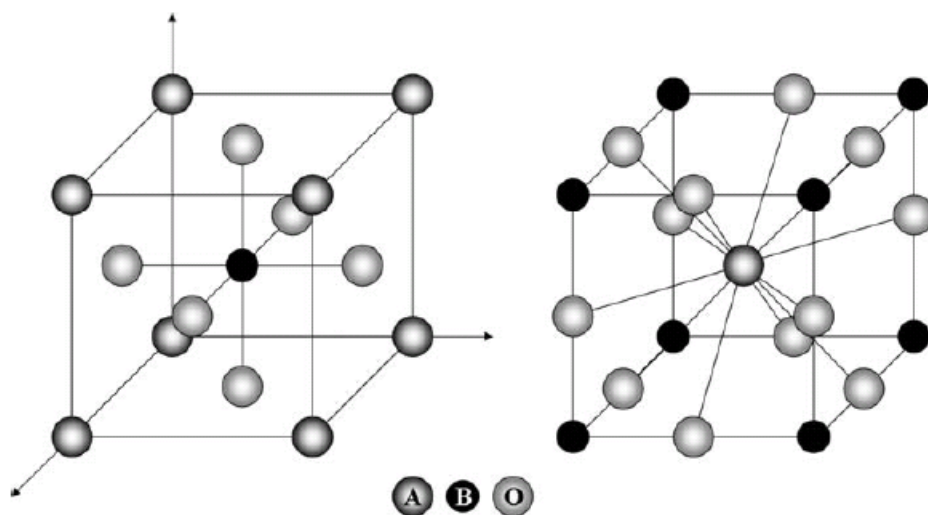


Figure 1.3: Schematic diagram of the cubic perovskite for ABO_3 type structures (51)

Perovskite-based materials are commonly used for SOFC cathode applications with the formulas such as $(\text{La,Sr})\text{MO}_3$ where $\text{M} = \text{Mn, Co, Fe}$. These materials are mixed with electronic/ionic conductors and exhibit better ionic transport properties (due to its oxygen over-stoichiometry), electronic conductivity (due to its metal mixed valence), better catalytic activity for the oxygen reduction and compatible thermal expansion properties (52 -55).

Mn-based cathodes are used for zirconia based systems working at above 800 °C, while $\text{M} = \text{Co}$, Co/Fe are used for lower temperature SOFCs based upon ceria electrolytes. Currently, most of the cathodes are based upon high oxidation transition ions such as Mn, Fe, Co, and Ni in an oxide lattice (51). On heating these types of oxides, or applying a bias, they lose oxygen and the transition metal ions become reduced, the lattice expands significantly or may even decompose. These materials are normally classified as p-type conductors. Perovskite-based SOFC cathode materials are briefly discussed below in different categories; they are lanthanum manganite based cathodes, other magnetite cathodes, lanthanum cobaltite cathodes and finally lanthanum ferrite cathodes.

1.2.1.1 Lanthanum manganite cathodes

For lanthanum manganite, the most famous and commonly used dopant for an SOFC cathode is strontium ($\text{La}_{1-x}\text{Sr}_x\text{MnO}_3$), because its size matches that of lanthanum. As stated before, LSM offers good thermal and chemical stability with smaller coefficients of thermal expansion, good compatibility with electrolyte (YSZ) and good electronic conductivity (23,56,57) In addition, it has reasonably good functionality at intermediate temperatures at around 700 °C, and may be used with alternative electrolyte materials. However Mn-doped materials are less active than Co and Fe analogues, therefore use at lower temperatures is more problematic.

1.2.1.2 Other magnetite cathodes

Most of the manganite-based perovskite materials do not offer good enough electrical properties at operational temperatures below 800 °C. Therefore researchers have been studying (LnSr)MnO₃ systems as a SOFC cathode where Ln=La, Pr, Nd, Sm, Gd, Yb or Y (58). Strontium-doped PrMnO₃ cathodes have shown low-over potential values, even at lower operational temperatures (and are used for IT-SOFCs) and exhibit a compatible thermal expansion coefficient with YSZ. Additionally, the formation of unwanted insulating phases with Ln₂Zr₂O₇ can be avoided by using smaller lanthanoids, especially the Nd_{1-x}Sr_xMnO₃, Pr_{1-x}Sr_xMnO₃ and Sm_{1-x}Sr_xMnO₃ systems (59).

Most of the work has focused on the lanthanide manganite materials where the A site is strontium doped, but some work has focused on A site calcium doped magnetite (Pr_{0.7}Ca_{0.3}MnO₃) cathode materials, which show good chemical stability and were thermally compatible ($11.9 \times 10^{-6} \text{ K}^{-1}$) with YSZ electrolyte materials (60).

1.2.1.3 Lanthanum cobaltite cathodes

Cobalt based materials often display better conductivities (electronic and ionic) than other types of perovskite based cathode materials. Hence, the use of cobalt based materials as SOFC cathodes should result in a decrease in the resistance of the cathode polarization. La_{1-x}Sr_xCoO_{3-d} materials have been reported with better electrode activities due to its high dissociation ability of oxygen molecules and high oxygen diffusivity. However, there are some drawbacks such as large amounts of cobalt-based cathode material result in an increased thermal expansion coefficient, which can result in a cracking of the electrolyte or delamination of the cathode/electrolyte interface (61).

1.2.1.4 Lanthanum ferrite cathodes

LaFeO_3 type cathode materials are expected to be more stable than cobaltite type perovskites cathode materials as the Fe^{3+} ion has a more stable electronic configuration ($3d^5$). Doping LaFeO_3 with strontium has shown promising cathode performance (62, 63). Also, ferrite based cathode materials have significantly reduced reactivity with YSZ. In addition, thermal expansion co-efficient values (TEC) of the ferrite perovskites are comparatively close to those of CGO and YSZ electrolyte.

1.2.2 K_2NiF_4 -type materials for SOFC cathodes

Several interesting cathode materials with K_2NiF_4 type structures are currently under investigation as SOFC cathodes due to their excellent electrochemical properties. They are a likely substitute for perovskite materials and show considerable promise as a potential SOFC cathodes. As shown in figure 1.4, K_2NiF_4 type structures are formulated as A_2BO_4 , which is described as a stacking of two layers, A_2O_2 layers with alternating BO_2 layers along the c direction.

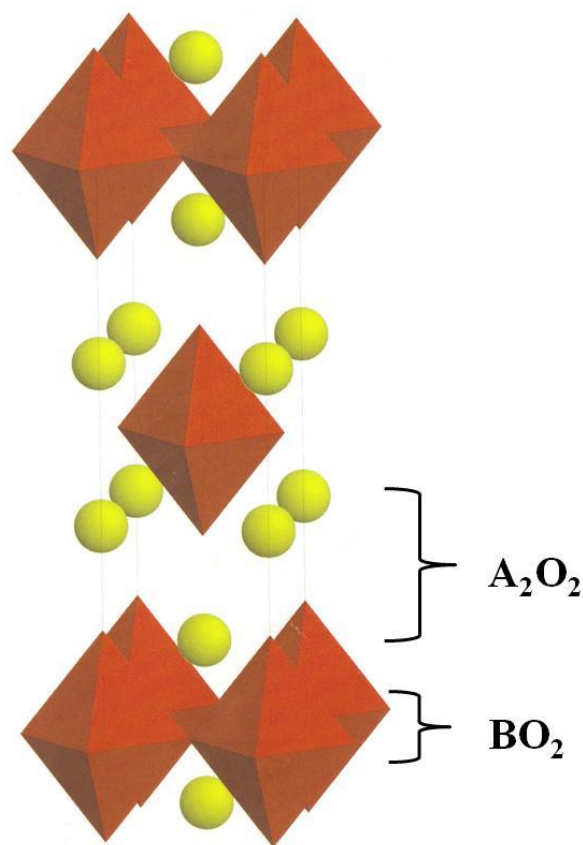


Figure 1.4: Schematic diagram of K₂NiF₄ type structure showing alternating A₂O₂ and BO₂ layers (64)

Significant mixed ionic and electronic conductivity has been reported for these K₂NiF₄ type structures (65). As discussed previously, lowering the operational temperature of SOFCs offers several benefits, therefore Ln₂NiO₄ type structures (Ln = Nd, La, Pr) have been studied by several groups and are reportedly more promising, even at low temperature SOFCs, and also as oxygen separation membranes (53,66-71). These structures typically have high oxygen diffusivity and catalytic activity which is due to the interstitial oxygen in the rock salt layer (53,71). Interstitial oxygen in these structures can be accommodated to promote ionic conductivity (55, 72). Also, the diffusion coefficient and the surface exchange coefficient of K₂NiF₄ type oxides are larger than those of conventional perovskite type oxides.

These materials show p-type electronic conductivity (69) and also offer TECs close to YSZ and CGO electrolytes (71). Long term stability at higher operation temperatures is more important for the SOFC material. As most Lanthanum-based cathode materials react with YSZ and form an insulating phase, researchers have focused on alternative materials for SOFCs with lanthanum free materials. Therefore, $\text{Pr}_2\text{NiO}_{4+\delta}$ has been researched as an SOFC cathode and is reported to have a high intrinsic bulk oxygen diffusion coefficient value ($D^*=2.5\times 10^{-8} \text{ cm}^2 \text{ s}^{-1}$ at 873K) and an oxygen exchange coefficient at the surface of the material of $k\approx 5\times 10^{-7} \text{ cm}^2 \text{ s}^{-1}$, (69). It has also been reported that $\text{Pr}_2\text{NiO}_{4+\delta}$ shows the largest amount of interstitial oxygen ($\delta\sim 0.22$ at room temperature), which is presumably due to the smaller ionic radius of Pr^{3+} which creates large structural stresses that is released by oxygen insertion (73). Because of these excellent electrochemical properties, K_2NiF_4 type oxides look promising as future SOFC cathode materials.

1.2.3 Cuprate based materials for SOFC cathodes

Long-term stability and stability in air with adjacent materials during processing are crucial requirements for the SOFC cathode side applications. Among these are poisoning due to volatile Cr species from the interconnect, balance of plant, and other high temperature plumbing. The presences of Mn and Sr have both been implicated in the sensitivity to Cr (74).

Cu based compounds are currently gaining greater attention within the fuel cell community, as they are good potential candidates as cathodes for SOFC. Recent research has targeted cuprate based materials for possible SOFC applications which show stable conductivity in reducing atmospheres and also allow efficient contact and current distribution. $\text{YBa}_2\text{Cu}_3\text{O}_{7-y}$ (YBCO123) is a well known perovskite related cuprate material widely studied as a possible

cathode material in SOFCs which show p-type conductor behaviour. Unfortunately, it also has a number of drawbacks due to degradation at low oxygen partial pressure or under polarisation condition (75).

Therefore p-type conducting cuprate (CuII/III) superconductors perhaps would offer the high electronic conductivity and fast oxygen diffusion required for a good cathode material though such materials are not particularly stable under load (75). However, Tao and co-workers have demonstrated a successful new concept of using a p-type conductor instead of the conventionally used n-type material as an anode, thus improving performance under load (1). Similarly, an n-type oxide with high electronic conductivity would offer a cathode material more resistance to chemical change on heating or load and its properties may improve under load.

The electron doped Nd_2CuO_4 family shows significant electrical conductivity which is of great interest for SOFC applications. In an n-type conductor, electrons are the charge carriers. To date, most studies of the electron-doped neodymium copper oxide family have studied their crystal chemistry and superconducting behaviour (76-78), but have yielded little information on their high temperature electrical properties. A major interest in this material is electron doping (as opposed to hole doping) as it may shed light on the mechanism of superconductivity (79-80). There are few examples of such highly conducting n-type oxides that are stable under oxidising conditions, with the most important example being studied for this purpose being Ce doped neodymium cuprates ($\text{Nd}_{2-x}\text{Ce}_x\text{CuO}_{4+d}$) (76,81) .

Most of the cathode materials (LSM, LSCF, YBCO123) currently being studied exhibit p-type semi-conductivity but it is expected that n-type conductivity may give operational advantages when operating at mild oxygen deficiency (e.g high oxygen utilization) or high cell polarisation, where the local cathode oxygen partial pressure is reduced. Also, as they

contain neither Mn nor Sr, (both of which have been implicated in nucleating Cr deposition) they may also have benefits in terms of Cr tolerance. Previous work in our group has identified that the highest conductivity of $\text{Nd}_{2-x}\text{Ce}_x\text{CuO}_4$ may exist around a dopant level of $x = 0.20$ and is stable at different temperatures. It also shows high conductivity which is stable to chemical and thermal stress while under load (82). Also, at room temperature the electrical conductivity of these cuprates is metallic/semi-conducting depending on the composition (77, 83).

A_2BO_4 stoichiometry adopts a variety of structures closely related to the K_2NiF_4 structure type. They are T, T', T* and O. All of the reports on these prospective cathode materials have focused on the tetragonal (T) and /or orthorhombic (O) K_2NiF_4 type oxides with less attention given to the reported T' phase structure type materials. $\text{Nd}_{2-x}\text{Ce}_x\text{CuO}_{4\pm\delta}$ (I/II) adopts the T' structure with the space group I4/mmm and displays Cu in square planar arrangements, planes of CuO_2 separated by Nd oxide fluorite layers and has flexibility in oxygen stoichiometry. Cu layers distorted in undoped Nd_2CuO_4 , doping reduces stress as well as introducing donor electrons. It has been reported as having significant total conductivity at temperatures up to 800°C with a semi-conductor/metallic transition at $\sim 500^\circ\text{C}$ (81).

1.3 Crystal chemistry of Ln_2CuO_4 structures

Rare earth (RE) based compounds of general formula A_2BO_4 (2-1-4 compounds) have been studied by several researchers for A (La, Nd) and B (Cu, Ni). Their different properties such as electrical (84-85), magnetic (86-89) and crystallographic transitions (89, 90) have been studied. In the case of $\text{La}_{2-y}\text{Ln}_y\text{CuO}_4$ (Ln = Lanthanide), three different tetragonal equilibrium structures T, T', T* stabilise depending on the size of the lanthanide cation and the value of

the substitution ratio y due to the bond length being matched to the intergrowth interface (76, 77, 91-95).

Table 1.1 summarises the major differences and possible space groups for these phases. The structural features common to all of these phases is the presence of CuO_2 planes but copper coordination can vary within these planes four –fold (T' phase), five –fold (T^* phase) and six-fold (T phase). The structures of T' , T and T^* are shown in figure 1.6, 1.7 and 1.8 respectively.

phase	Cu coordination	Ln-O layer arrangement	Ln coordination	space group
T'	4	Fluorite (F)	8	I4/mmm
T	6	Rock-salt (RS)	9	I4/mmm
T^*	5	F,RS	8,9	P4/nmm

Table 1.1: Major differences and possible space groups for T' , T and T^* phases

With multiple transition metal coordination it is possible as these materials can adopt a wide range of oxygen stoichiometries. The excess oxygen content resides on interstitial sites, as in the transition metal analogues. They are not compensated by cation vacancies as is often observed in ABO_3 type materials. This could lead to interesting electrical behaviour in these ceramics, which may be of interest for electrochemical applications such as solid oxide fuel cells. In this study, two different crystal structures were considered, one of the tetragonal modifications T' , and the orthorhombically distorted K_2NiF_4 -type structure denoted as T/O .

The parent compounds of these structures are Nd_2CuO_4 for T' and La_2CuO_4 for T/O. In these cuprate systems, Cu can be oxidized (formal valence becoming greater than 2) or reduced (formal valence becoming less than 2) either by uptake or removal of oxygen respectively, or through a cationic substitution.

As shown in Figure 1.5, the transition from the T to T' structural preference on going from La to Pr, Nd, Eu or Gd is driven by the lanthanide contraction, with a smaller Lanthanide ion favouring 8 fold rather than 9 fold coordination (96).

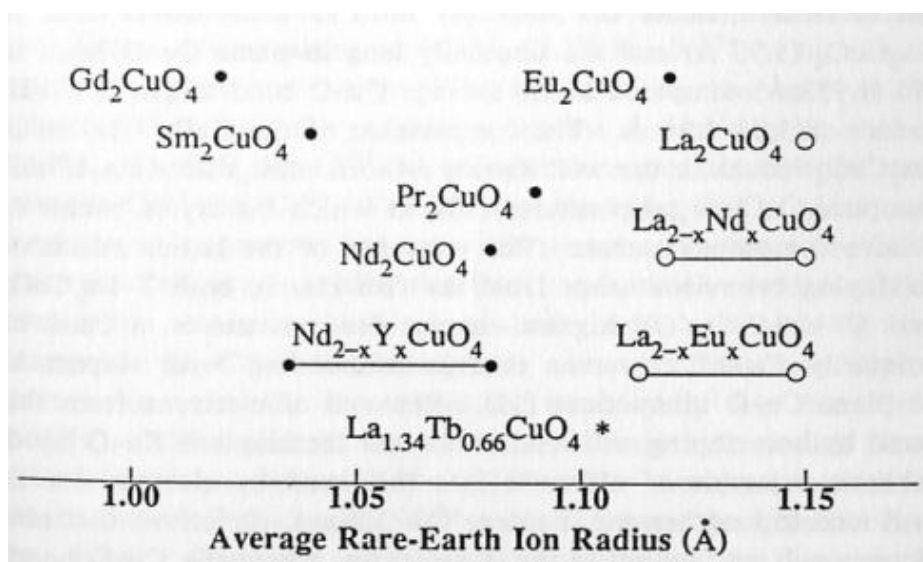


Figure 1.5: Stability fields of the T and T' structures in rare-earth cuprates as a function of average rare-earth ionic radius. Filled circles represent the T' phases, open circles represent the T phase and stars represent the T^* phase (96)

1.3.1 T'-Nd₂CuO₄ Structure

Nd₂CuO₄ shows a typical T' phase structure (figure 1.6). The structure consists of Cu atoms located in flat CuO₂²⁻ layers, with Cu in a strictly square planar coordination, alternating with Nd₂O₂²⁺ layers. The Nd₂O₂²⁺ layers display a fluorite structural arrangement. Nd atoms have an oxygen coordination number of 8 and are located in this layer far from the Cu apical position (97). Rare earth ions of intermediate size (Pr-Gd) exhibit the T' structure.

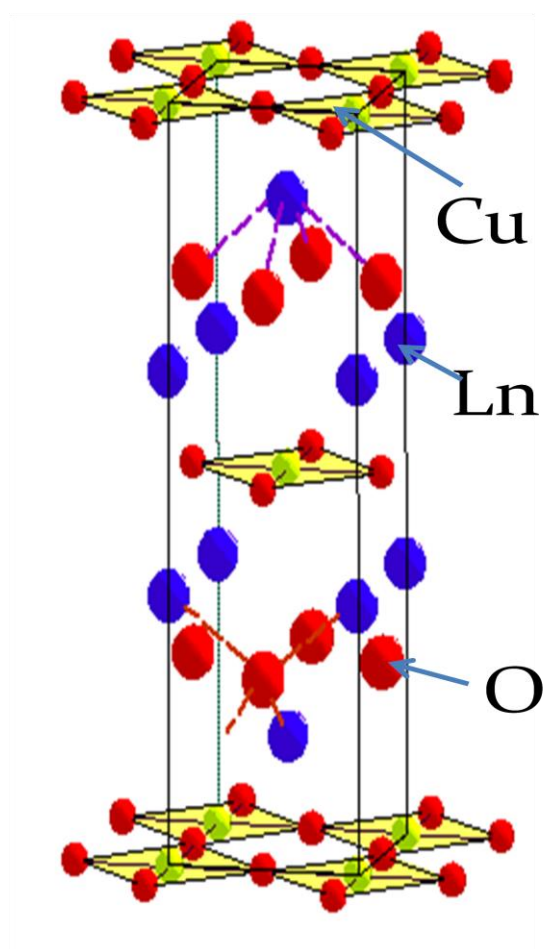


Figure 1.6: Schematic diagram of T'-type structures

Average Cu-O bond length in Nd_2CuO_4 is around 1.973 Å and the average Cu-O bond length in Cu (II) oxides is between 1.93-1.94 Å (96). Therefore in Nd_2CuO_4 , the CuO_2^{2-} layers are in tension and which leads to unusually long in-plane Cu-O bonds in Nd_2CuO_4 . Introducing electrons into this system by electron doping is liable to increase the in-plane Cu-O bond length. Therefore electron doping is favourable for the T' structure where bonds are in tension. Furthermore hole doping in T' - Nd_2CuO_4 is unfavourable.

Cationic substitutions in the T' phase of the $\text{Nd}_{2-x}\text{M}_x\text{CuO}_4$ system involves replacing the trivalent rare earth by a tetravalent ion. In this system, electron doping can be achieved by substituting a tetravalent cation (Ce^{4+} , Th^{4+} , Pr^{4+}) for Nd^{3+} or by substituting a monovalent anion (F^-) for O^{2-} (98).

1.3.2 T- La_2CuO_4 Structure

As shown in figure 1.7, in the La_2CuO_4 (T phase structure), the $\text{La}_2\text{O}_2^{2+}$ layers display a rock salt structure, with La having a total oxygen coordination number of 9. Oxygen atoms are located in the apical positions in the CuO_2^{2-} sheets, above and below Cu. The structure can undergo a slight orthorhombic distortion from the K_2NiF_4 structure. It is normally denoted as an orthorhombic T phase (T/O). Rare earth ions of large size (e.g. La) exhibit T/O structure

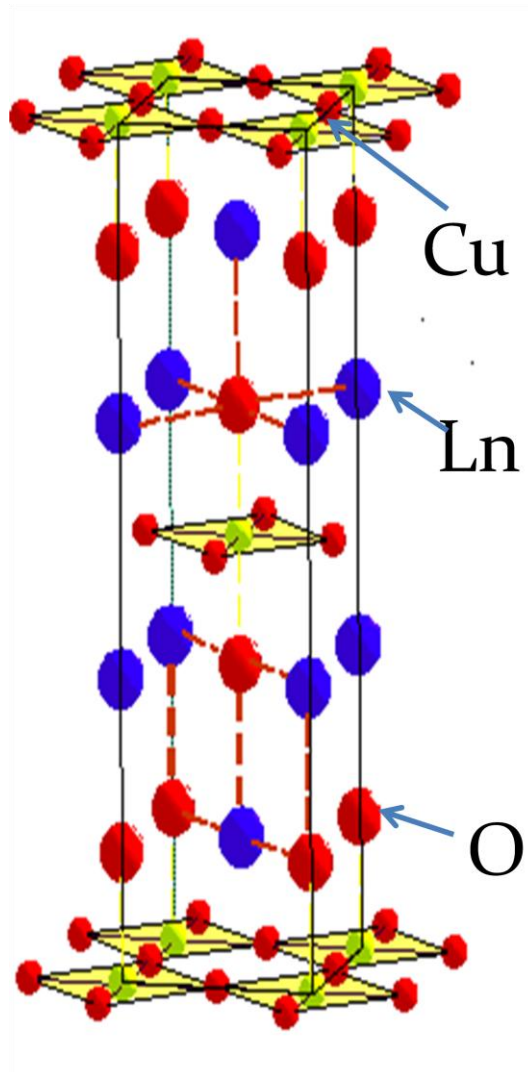


Figure 1.7: Schematic diagram of T type structures

Average Cu-O bond length in La_2CuO_4 is around 1.90 Å and the average Cu-O bond length in Cu (II) oxides is between 1.93-1.94 Å (96). In La_2CuO_4 , the CuO_2^{2-} layers are compacted by the neighbouring $\text{La}_2\text{O}_2^{2+}$, which lead to unusually short in-plane Cu-O bonds in La_2CuO_4 . This compression of the CuO_2^{2-} layers in La_2CuO_4 also results in the well known orthorhombic distortion in this system at low temperatures (99).

Removal of electrons from this system by hole doping is liable to shorten the in plane Cu-O bond. Therefore hole doping is favourable for the T structure where Cu-O bonds are in compression. Relief of the compressive stresses in the Cu-O plane is the driving force for

hole doping in the T structures. Therefore, electron doping in T- La_2CuO_4 is unfavourable. Hole doping can be achieved for the La_2CuO_4 (T/O phase) by partial replacement of the La^{3+} by an alkaline metal, an alkaline earth metal or by the insertion of interstitial oxygen, fluorine or chlorine to the system thereby increasing the formal valence of the copper (100-104).

1.3.3 T* Structure

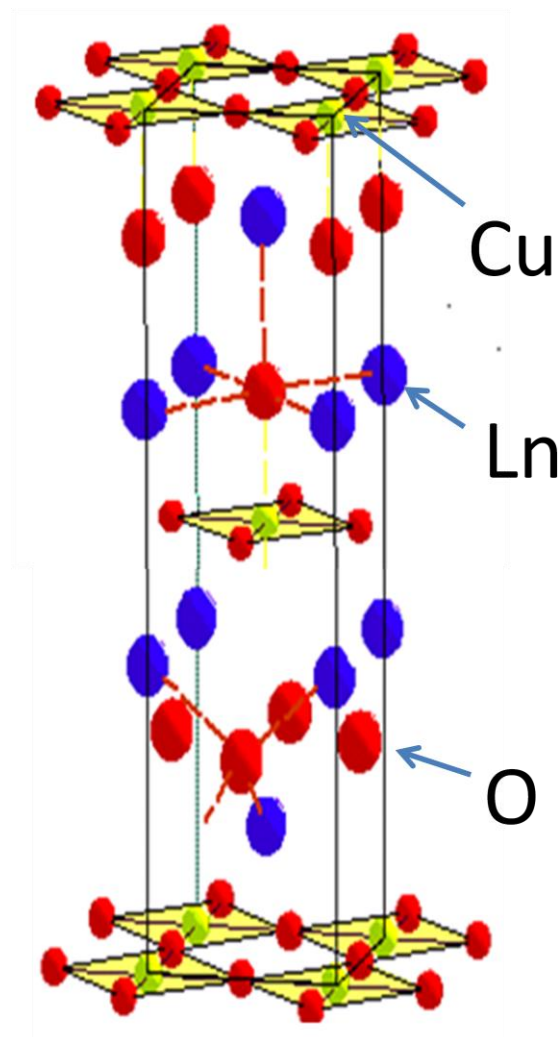


Figure 1.8: Schematic diagram of T* type structure

As shown in figure 1.8, the T^* phase is an intergrowth of the T and T' structure, which is evidenced when the rare earth ion site is occupied by two ions of very dissimilar radii. T^* phase has Cu five-fold coordination with the oxygen atoms occupying both the apical oxygen (4d) and fluorite-type oxygen sites (4e). It alternates between rock salt layers of the T structure and the fluorite-type layers of the T' structure. For the smaller lanthanides, particularly for Tb and Dy, T^* hybrid structure is formed only over a very narrow range of compositions (92, 94). T^* phases have been reported for the composition $La_{2-x}Tb_xCuO_4$, where $x = 0.6, 0.7$ (105), and $La_{1.1}Dy_{0.9}CuO_4$ (92).

Due to bond-length matching, smaller Ln^{3+} ions preferentially locate in the fluorite-type layers (106). In the case of $La_{2-y}Ln_yCuO_4$, the thermodynamic stability of the T^* phase can be improved by the partial substitution with Sr^{2+} which leads to a wider compositional range for $La_{2-y}Ln_yCuO_4$ ($Ln=Nd, Sm, Eu, Gd, Tb$ and Dy)(94). And also it has been reported that Sr-doped materials become superconducting ($T \approx 30$ K) after annealing in high-pressure oxygen (107).

1.3.4 T'' Structure

Interestingly, another phase called T'' has been reported for the $Ln_{2-x}Ln'_xCuO_{4\pm\delta}$ family which has similar X-ray diffraction patterns to T' , but has larger a and c parameters compared to the T' phase. It has been suggested that T'' contains unique cation ordering of roughly $3(Ln):1(Ln')$ in the $Ln-O$ layer, and interlayer ordering at the Ln_3Ln' composition and it has been claimed as an equilibrium phase (76, 77, 91, 108).

Studies on $La_{2-y}Nd_yCuO_4$ and $La_{2-y}Pr_yCuO_4$ systems have reported slightly larger a and c cell parameters for the T'' phase appearing as a line phase at $y \approx 0.5$ ($La=1.5$) composition, and also suggested it is an ordered form of T' (76, 77, 91). Ideal Cu co-ordinations for T' , T^* , T

are 4, 5 and 6 respectively. However, there is no solved crystal structure for the T'' phase in the literature. Therefore it is very important to identify the new T'' phase, and to gain a better understanding of the oxygen occupancies within these phase transitions (T to T''). Hypotheses on the T'' phase in the literature have not yet been confirmed and some are in disagreement with our studies. Therefore we have fully explored this system in detail using temperature dependent X-ray diffraction, selected area electron diffraction (SAED), neutron diffraction and conductivity measurements as described in chapter 5.

1.4 Properties of La_2CuO_4 and Nd_2CuO_4 structures

Due to different structural arrangements, Nd_2CuO_4 (T') and La_2CuO_4 (T) show different properties, for example T' - Nd_2CuO_4 is a semiconductor while T - La_2CuO_4 is metallic. Nd_2CuO_4 and La_2CuO_4 are the parent compounds of the electron and hole-doped high- T_c superconductors respectively. La_2CuO_4 is a superconducting material when doped with holes either by replacing some of the La with Sr, Ba, Ca, or Na (e.g. $\text{La}_{1.85}\text{Sr}_{0.15}\text{CuO}_4$ is superconducting at 38 K (109) or by introducing excess oxygen into the structure (e.g., $\text{La}_2\text{CuO}_{4.13}$ is superconducting at 38 K (110)). T' structure of Nd_2CuO_4 superconducts only when electron-doped, for example $\text{Nd}_{1.85}\text{Ce}_{0.15}\text{CuO}_4$ is superconducting at 24 K (98) and $\text{Nd}_{1.85}\text{CuO}_{3.6}\text{F}_{0.4}$ is superconducting at 27 K (111). The properties of the T' and T phases also strongly depend on oxygen stoichiometry, for example superconductivity in $\text{Nd}_{1.85}\text{Ce}_{0.15}\text{CuO}_4$ can be altered by changes as small as 1% in oxygen content (112,113). The properties of $\text{La}_2\text{CuO}_{4+\delta}$ also depend on the oxygen stoichiometry, for example $\text{La}_2\text{CuO}_{4+\delta}$ is an anti-ferromagnetic semiconductor where the Neel temperature is 257 K (114). But this anti-ferromagnetic behaviour disappears with small changes (1%) in oxygen stoichiometry.

As δ becomes positive, holes are introduced into the structure which tend toward metallic behaviour (96). Therefore oxygen stoichiometry is a crucial factor for the determination of the properties of Nd_2CuO_4 and La_2CuO_4 .

Both these materials have a layered structure and good conductivity properties could be expected as a result. Both T and T' phases show very good performance as electrodes, with p-type and n-type conducting properties, respectively. As discussed previously, both these p- and n-type cuprates are expected to be good candidates for SOFC applications. T phase displays high oxygen diffusivity and catalytic activity, which is caused by interstitial oxygen in the rock salt layer (75) and T' phase type oxides ($\text{Nd}_{2-x}\text{Ce}_x\text{CuO}_4$) which exhibit n-type behaviour, are also of interest and are studied as interesting cathode materials (82).

P-type cuprate superconductors offer high electronic conductivity and fast oxygen diffusion, which is required for a good cathode material and n-type cuprates with high electronic conductivity may offer higher resistance to chemical change on heating or load, which is desirable for a good cathode material. Therefore, both these structures are important in the SOFC community as they display good electrical properties and currently being investigated as potential candidate for SOFC cathode.

1.5 Phase relationship and structural transition in $\text{Nd}_{2-y}\text{La}_y\text{CuO}_4$ system

$\text{La}_{2-x}\text{Ln}_x\text{CuO}_4$ ($\text{Ln} = \text{Nd-Y}$) have been investigated by several researchers to understand the crystal chemistry and stability of the related phases of T, T', O and T* structures (76, 77, 91, 94,116,117). Bringley and co-workers proposed an ionic model to discuss the crystal chemistry of these materials and the correlation between the size of the lanthanide cation (Ln) and structure (94). They used the perovskite-like tolerance factor (t) to define the stability

limits of the T, T', and T* phases. As shown in figure 1.9, T structure is found to exist for $0.87 \leq t \leq 0.99$, T' structure occurs for $0.83 \leq t \leq 0.86$ while T* structure occurs in a very narrow region closest to the boundary of the T/T' stability field. They also found that T* phases become quite stable when RE = Tb, Dy. They explain that there is competition between copper ions and lanthanide ion and for bonding with the apical oxide in La_2CuO_4 . In the T' phase, the Cu-O bond length elongates with respect to the equatorial Cu-O in the T phase, and the Nd-O bond distances are shorter than the La-O bond distance. It has been suggested that the RE-O layer is the main driving force in this T-T' transition in $\text{La}_{2-x}\text{Nd}_x\text{CuO}_4$ system (94).

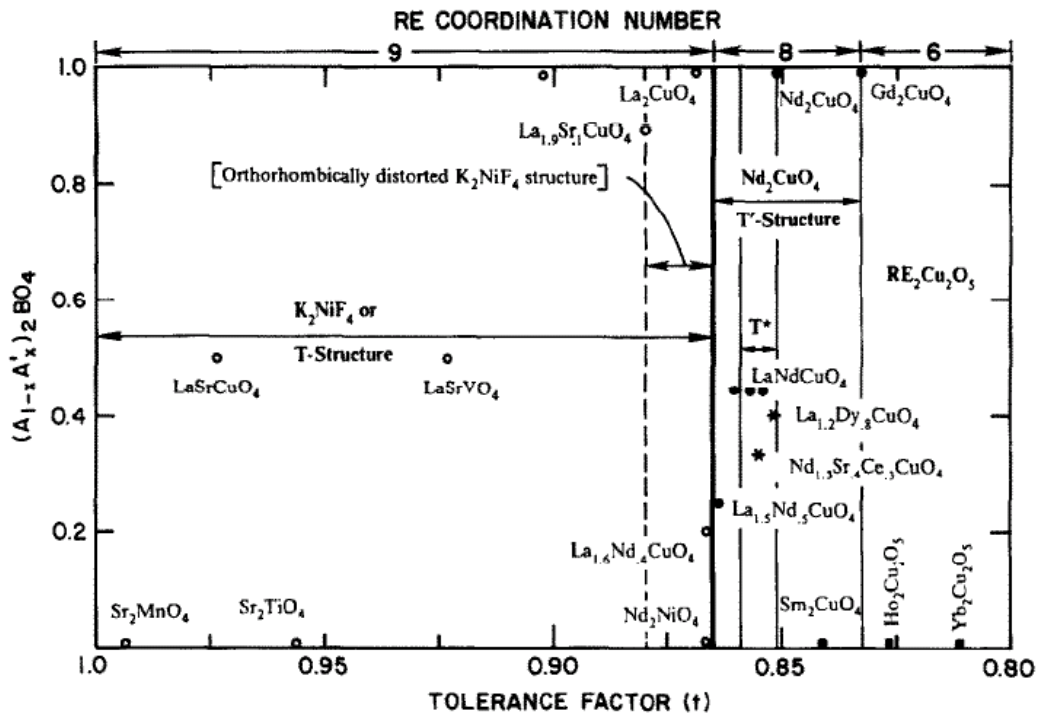


Figure 1.9: Composition of discrete phases and solid-solutions exhibiting the T, T', and T* structures found in $(\text{La},\text{RE})_2\text{CuO}_4$ where RE s denotes a rare earth element (94)

The study of the solid solubility of Nd_2CuO_4 (T') and La_2CuO_4 (T) provides a measure of the relative stabilities of these structural phases. Therefore, it is interesting to examine the nature

of the transition from the Nd_2CuO_4 structure to the La_2CuO_4 structure by examining the crystal structures and electrical properties of the solid solutions. Changing the lanthanide ion from Nd^{3+} to La^{3+} leads to the related T structure. It is known that in $\text{La}_{2-x}\text{Nd}_x\text{CuO}_4$, phases with $x < 0.5$ exhibit the T structure and phases with $x > 0.6$ exhibit the T' structure (118). It has been reported that a more condensed structure was obtained for the T structure compared to T' phase, for example the volume of LaNdCuO_4 for T' (I4/mmm, Z=2), T (I4/mmm, Z=2) and O (Cmca, Z=4) were 195.328 \AA^3 , 174.10 \AA^3 and 354.82 \AA^3 respectively (119).

Studies on $\text{Nd}_{1.85-x}\text{La}_x\text{Ce}_{0.15}\text{CuO}_4$ and $\text{Nd}_{1.85-x}\text{La}_x\text{Th}_{0.15}\text{CuO}_4$ systems have shown that the with increasing lanthanum content, T' phase may transform to the T phase without any evidence of the T^* phase and the solubility limit for La is increased by the presence of Ce (117), hence evidence for the T^* phase for $\text{La}_{2-x}\text{Nd}_x\text{CuO}_4$ is very rare in the literature. Therefore, most of the studies on the $\text{La}_{2-x}\text{Nd}_x\text{CuO}_4$ system that have been reported show two major phases (T' , T). However, some research groups have identified another new phase called T'' (76, 77, 91, 108). T'' has been reported to have a similar X-ray diffraction pattern to T' , but slightly larger a and c parameters compared to the T' phase. As shown in figure 1.10, there are five distinguishable regions for $\text{La}_{2-x}\text{Nd}_x\text{CuO}_4$ at room temperature. They are (1) monophasic T' solid-solution (2) two phase mixture $\text{T}' + \text{T}''$ (3) monophasic T'' (4) two phase mixture $\text{T}'' + \text{O}$ and (5) monophasic O-phase solid-solution.

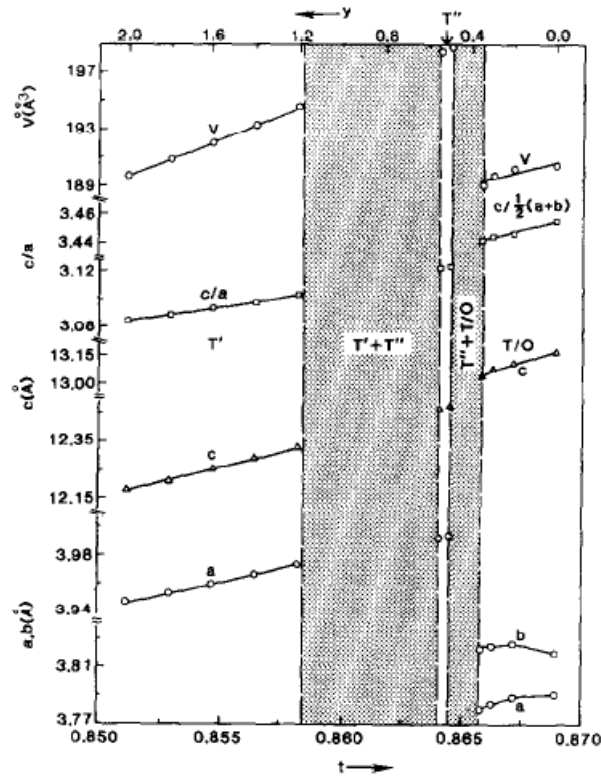


Figure 1.10: Variation of room temperature lattice parameters with tolerance factor (t) or y for the $\text{La}_{2-y}\text{Nd}_y\text{CuO}_4$ system (77)

In the $\text{La}_{2-y}\text{Nd}_y\text{CuO}_4$ system, it is claimed that the T'' phase appears as a line phase at $y \approx 0.5$ ($\text{La} = 1.5$) composition where the $\text{Nd}:\text{La}$ ratio is roughly around 3:1 (76,77,91). The two phase ($T' + T''$) region was observed at $0.6 \leq y \leq 1.1$ for $\text{La}_{2-y}\text{Nd}_y\text{CuO}_4$. Work carried out at 950°C in air by Singh *et al.* (116) evidenced the T structure in the $0 \leq y \leq 0.17$ range, and T' in the $0.25 \leq y \leq 2$, whereas Wang *et al.* (117) reported a two phase ($T' + T$) region with $0.4 \leq y \leq 1.1$ for samples prepared in oxygen at 1100°C . Bringley *et al.* (95) observed two phases for $0.8 \leq y \leq 1.0$, and they found that prolonged heating (>100 hr) in air at 1050°C , with intermediate regrinding, produced the single phase T' , when the samples were quenched. They also suggested that the T' solid solubility field narrows at higher temperature and/or higher oxygen activity and that phase relationships depend strongly upon synthesis and

annealing conditions. Reported phase relationships in these systems vary and depend on the synthetic route, firing temperature and the stability/metastability fields of the closely related T, T'', and T* phases.

1.6 Semiconductor materials

A semiconductor is a substance that has conductivity ($\sim 10^3$ to 10^{-8} Scm^{-1}) in between an insulator and conductor, This can be due either to the dopant or to temperature effects. Generally semiconductors are crystalline solids, but amorphous and liquid semiconductors are also identified. Semiconductor materials are commonly used in modern electronics, such as radios, telephones, computers, and many other electronic devices. Semiconductors fall into two main categories; intrinsic and extrinsic.

Semiconductor band gaps are small enough, such that a small increase in temperature promotes a sufficient numbers of electrons from the valence band to the conduction band. This creates electron holes, or unoccupied levels in the valence band, and very loosely held electrons in the conduction band. The conductivity of intrinsic semiconductors is reasonably low at room temperature. Conductivity can be considerably improved by the doping processes making it an extrinsic semiconductor. The negative charge of the electrons is balanced by an equivalent positive charge in the centre of the dopant atoms. Hence, the net electrical charge of the semiconductor material is not changed.

1.6.1 Intrinsic semiconductors

Intrinsic semiconductors are also called pure semiconductors and they do not contain any dopant species. Therefore the number of charge carriers is determined by the properties of the material itself instead of the amount of impurities. In an intrinsic semiconductor, the number of electrons in the conduction band is equal to the number of holes in the valence band. The electrical conductivity of intrinsic semiconductors can be due to crystal defects or to thermal excitation.

1.6.2 Extrinsic semiconductors

An extrinsic semiconductor is a semiconductor that has been doped with other substances in order to change their conductive properties. This means that their electronic properties and conductivity may change in a controlled manner by adding specific dopants to the intrinsic material. Dopant atoms come from different elements than the atoms of the intrinsic semiconductor. The electrical conductivity may be changed, not only by the number of dopant atoms, but also by the type of dopant which may produce 10^3 - 10^6 increase in conductivity. Therefore, specific properties of extrinsic semiconductors depend on the specific dopant added to them.

Dopant atoms act as either donors or acceptors to the intrinsic semiconductor atoms and change its electron and hole carrier concentrations at thermal equilibrium. Depending on the carrier, concentrations of an extrinsic semiconductor, they are classified as either n-type or p-type. Electrical properties of these types of semiconductors make them essential components of many electronic devices, solar cells, fuel cells, etc.

1.6.3 N-type and P-type semiconductors

Electrons are the charge carriers for n-type semiconductors, while p-type semiconductors carry current mainly as electron deficiencies called holes. A hole has a positive electric charge, equal and opposite to the charge on an electron. Applying an external voltage to the sample, both the electron and the hole can move across the material. Flows of holes occur in a direction opposite to the flow of electrons in a semiconductor. In an n-type semiconductor, the dopant donates extra electrons which considerably increases the conductivity. However, in a p-type semiconductor, the dopant creates extra holes which similarly increase the conductivity. Therefore, both n- and p-type semiconductors are important for many applications.

1.6.4 Fermi level and band theory for extrinsic semiconductors

The Fermi level is important to describe the behaviour of extrinsic semiconductors and also helps to explain the different behaviours between insulators, metals and intrinsic and extrinsic semiconductors. The Fermi level of a substance is defined as the highest occupied energy level found in that substance at absolute zero temperature (0 K).

In band theory for semiconductors, there are mainly two bands to consider. The fully occupied lowermost band, called the valence band and the (almost unoccupied) uppermost band is called the conduction band. Only when electrons are excited to the conduction band can current flow in these materials. One of the main mechanisms for electrons to be excited to this conduction band is due to thermal activation. Therefore, conductivity of semiconductors is strongly dependent on the temperature of the material.

Donor impurity atoms contain more valence electrons than the atoms they replace in the intrinsic semiconductor lattice and provides extra valence electrons to a semiconductor's conduction band. These excess electrons increase the electron carrier concentration of the semiconductor, making it n-type. Acceptor impurity atoms contain less valence electrons than the atoms they replace in the intrinsic semiconductor, it accepts electrons from the semiconductor's valence band and provides extra holes to the intrinsic semiconductor. These extra holes increase the hole carrier concentration of the semiconductor, making it p-type.

Band theory of n-type semiconductors shows that they have a Fermi level higher than the intrinsic Fermi energy level and it lies closer to the conduction band, while p-type semiconductors have Fermi energy levels below the intrinsic semiconductors and lie closer to the valence band. N-type and p-type semiconductors show that extra energy levels have been added by the dopant (Figure 1.11). In n-type materials, extra electron energy levels lie near to the top of the band gap, hence they can be more easily excited into the conduction band, while in p-type materials, creation of an acceptor energy level, close to the valence band, allows excitation of valence band electrons, leaving mobile holes in the valence band. The n- and p-type labels specify which charge carrier is its majority carrier. The opposite carrier is called the minority carrier, which is present due to thermal excitation at a much lower concentration compared to the majority carrier.

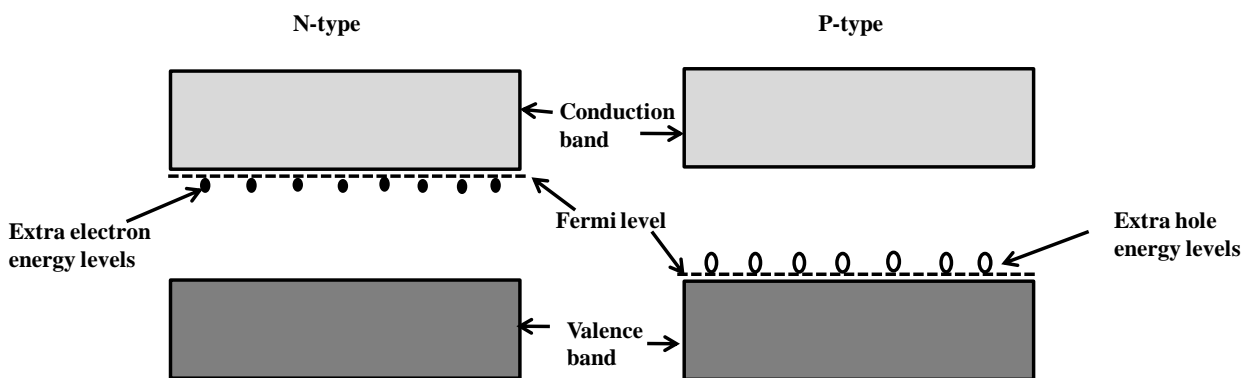


Figure 1.11: Schematic diagrams for band structures of extrinsic semiconductors

1.7 $\text{Nd}_{2-x}\text{Pr}_x\text{CuO}_4$ system (NPCO)

Another possible system of interest as a SOFC cathode material is the n-type semiconductor praseodymium doped neodymium cuprates ($\text{Nd}_{2-x}\text{Pr}_x\text{CuO}_{4\pm\delta}$). Similar to Nd_2CuO_4 , Pr-doped Nd_2CuO_4 exhibits T' phase. As with the Ce doping described previously, the aim is to incorporate tetravalent cations into the structure both to introduce donor electrons and to relieve some of the stress in the CuO planes to improve the conductivity. However, praseodymium exists in several non-stoichiometric oxide phases with a mixture of Pr^{4+} and Pr^{3+} cations present, a common example being Pr_6O_{11} . This mixture of oxidation states and the resulting oxygen non-stoichiometry is of considerable interest in SOFC cathode applications as it may be advantageous for the adsorption of oxygen species during oxygen reduction or for the enhancement of mixed ionic-electronic conductivity within the bulk of the material. Therefore, doping with Pr can be useful for electrocatalysis of the oxygen reduction process.

Therefore in this thesis, Pr doped Nd_2CuO_4 has been investigated to probe the basic high temperature electrical characteristics and how this matches with those required for components on the SOFC cathode side. Furthermore, the aim of this work was to make a new concept in SOFC cathode and current collector development, using n-type conductors instead of p-type conductors and try to produce a high conductivity material which are stable to the chemical and thermal stress that exist while under load that can be used in cathode or current collector application. Electrocatalytic properties were investigated for $\text{Nd}_{2-x}\text{Pr}_x\text{CuO}_4$ as a cathode material and then evaluated performances on both ceria doped gadolinia (CGO) and yttria stabilised zirconia (YSZ) based electrolytes using area specific resistance values.

1.8 $\text{Nd}_{1.8}\text{La}_x\text{Pr}_{0.2}\text{CuO}_4$ system (NLPCO)

As described before, La_2CuO_4 (T) and Nd_2CuO_4 (T') are well known as the parent phases of the p- and n-type cuprate superconductor families with ideal Cu co-ordinations of 4 and 6, respectively (101,98). These multiple copper coordinations play an important role in the choice of possible dopants and their properties. Due to these different crystal structures they exhibit different properties, for an example Nd_2CuO_4 (T') is semiconducting while La_2CuO_4 (T) is metallic. Therefore it is interesting to study the structural transition T' to T using Nd_2CuO_4 - La_2CuO_4 . Many researchers have explored this system, and reported that the $\text{Nd}_{2-y}\text{La}_y\text{CuO}_4$ bond length matching across the intergrowth interface stabilizes mainly three different structures T/O, T', T'' depending on the La substitution ratio (y) (76,77,91,108,116,117), but the phase relationship between these systems in literature varies and is strongly dependent on the synthetic route, firing temperature and the stability/metastability fields of these closely related phases.

To study the T' phase stability with respect to T, T* and O phases, lanthanum-doped neodymium praseodymium cuprate ($\text{Nd}_{2-x-y}\text{La}_y\text{Pr}_x\text{CuO}_4$) systems were used. Co-doping with La and Pr into the Nd_2CuO_4 (T') causes more distortion to the T' structure. Increasing the lanthanum content, the T' phase may transform to the T phase with possibly an intermediate phase occurring. There is no literature on phase transformation of $\text{Nd}_{2-x-y}\text{La}_x\text{Pr}_y\text{CuO}_4$ system. Therefore this system has been fully explored in this thesis with different techniques. $\text{Nd}_{2-x-y}\text{La}_y\text{Pr}_x\text{CuO}_4$ materials have been produced with composition over the range $0 \leq y \leq 1.8$ and $x=0.2$. Doping with Pr^{4+} (Pr_6O_{11}) relieves some of the strain in these Cu-O layers, and also introduces electrons to the system which promotes n-type behaviour. The aim has been to keep Pr level constant while changing the ratio of La and Nd ($\text{Nd}_{1.8-x-y}\text{La}_x\text{Pr}_y\text{CuO}_4$) and study any crystal change along this series.

In order to introduce the maximum number of electrons in to the system while avoiding the formation of ex-solution phases a Pr dopant concentration of $x=0.2$ was used and kept constant all over the series. According to our knowledge there is no high temperature phase characterisation study for these systems in literature. Therefore in this work we investigated the high temperature X-Ray analysis for T, T', T'' and O phases to get a better understanding about this system. Also as has already been discussed these materials exhibit a layered structure; this will lead to highly anisotropic behaviour especially with respect to conductivity. Therefore the structural, magnetic and electrical properties of $\text{Nd}_{2-x-y}\text{La}_x\text{Pr}_y\text{CuO}_4$ (NLPCO) materials have been investigated for the selected compositions.

Chapter 2- Experimental techniques and their theoretical background

2.0 Introduction

All the materials studied in this PhD have been synthesised by solid state methods and characterised by different techniques, therefore in this chapter, experimental techniques and their theoretical backgrounds are briefly summarised. They include solid state reaction methods, X-ray diffraction, electron diffraction, neutron diffraction, thermal analysis, magnetization method, conductivity measurements and impedance measurements.

2.1. Solid state reaction methods

A solid state reaction is also referred to as a dry media reaction or as a solventless reaction. It is a chemical reaction in which solvents are not used whatsoever. In a conventional reaction the reactants are placed in a solvent (organic or aqueous) so that they can chemically react to form new substance. After the reaction is completed, it is capable to extract the new product from the solvent by different methods such as solvent extraction or evaporation techniques. But in a solid-state reaction, however it allows the reactants to chemically react without the presence of any solvent. With normal reactions it is necessary to remove the residual solvent from the resulting product after a reaction has occurred. But producing a material from a solid state reaction mean able to bypass the purification process and also is more environmentally friendly since there are no solvents, there is no waste to eliminate at the end of the reaction. Eliminating the solvent from the reaction means that a solid state reaction may produce more

products than a conventional reaction can. And also elimination of solvents means that products will cost less and will make those products cheaper to buy.

Preparation of $\text{Nd}_{1.8-x}\text{La}_x\text{Pr}_{0.2}\text{CuO}_4$ family was carried out by the following solid state reaction method. Hygroscopic powders (Nd_2O_3 , Pr_6O_{11} , and La_2O_3) were dried for 30 minutes at temperatures up to 900 °C. Stoichiometric amounts of Nd_2O_3 (Alfa-Aeser 99.9%), Pr_6O_{11} (Alfa-Aeser 99.9%), CuO (Aldrich 99+ %) and La_2O_3 (Aldrich 99.99%) were then weighed and ground in acetone. These mixtures were then dried and calcined in air at 850 °C for 36 hours. Following this, powders were reground using a planetary ball mill and the heat treatment (850°C for 36 hours) repeated. T'' phases were obtained by calcinations at 950 °C for 24 hours.

Preparation of composition in the $\text{Nd}_{2-x}\text{Pr}_x\text{CuO}_4$ family was carried out using following solid state reaction method. Hygroscopic powders were dried for 30 minutes at temperatures up to 900 °C. Stoichiometric amount of Nd_2O_3 (Alfa-Aeser 99.9%), Pr_6O_{11} (Alfa-Aeser 99.9%), CuO (Aldrich 99+ %) were weighed and ground in Acetone. Then the mixtures were dried and treated in air up to 850°C for 36 hours. Resulting powders were reground (using a planetary ball mill) and the heat treatment was repeated (850 °C for 36 hours). Annealing and quenching experiments were carried out by using standard muffle furnace.

2.2. X-ray diffraction

X-ray diffraction has been in use as the fingerprint of crystalline materials and the determination of their structure. X-ray diffraction is one of the most important characterization tool nowadays used in solid state chemistry and materials science. Each crystal structure has its distinctive X-ray diffraction pattern. Once the material has been identified, X-ray diffraction can be used to determine its structure (e.g how the atoms are packed together in the crystalline state, interatomic distances and angles etc.) Also, the size and shape of the unit cell of the compound can be determined by this technique. X-ray diffraction yields the atomic structure of materials which is based on the elastic scattering of X-rays from the electron clouds of the individual atoms in the compound. Diffraction occurs when waves interact with a regular structure whose repeat distance is about the same as the wavelength. X-rays are electromagnetic radiation which has wavelengths on the order of a few angstroms, which is nearly the same size as an atom.

When certain geometric requirements are achieved, X-rays scattered from a crystalline solid can constructively interfere, producing a diffracted beam. Relationship among several factors are combined in Bragg's Law (120),

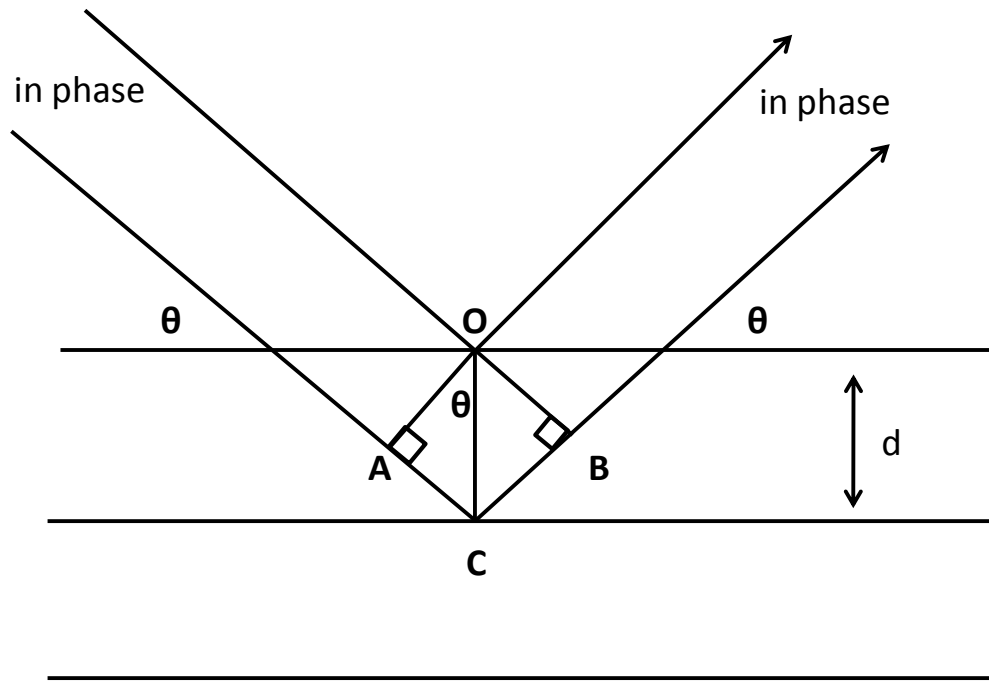


Figure 2.1: Reflection of x-rays from two planes of atoms in a solid

For constructive interference between these waves, the path difference must be an integral number of wavelengths.

Therefore, 2nd wave is in phase after reflection if only,

$AC + CB$ is an integer multiple of λ (e.g. $n\lambda$)

Since,

$$AC = CB; 2AC = n\lambda$$

$$\sin \theta = AC/d; AC = d \sin \theta$$

This leads to the Bragg equation,

$$n\lambda = 2d \sin \theta$$

2.1

1) n = an integer (1,2,3)

2) d = d spacing (The distance between similar atomic planes measured in angstroms)

3) θ = The diffraction angle in degrees

4) λ = wavelength of the incident X-radiation in Angstrom

Bragg's law shows that the sine of the diffraction angle ($\sin \theta$) is inversely related to the lattice spacing (d) in a crystalline sample.

Miller indices are a notation system in crystallography for planes and directions in crystal (Bravais) lattices. They are defined by three integers (h , k and l). Combining these two approaches gives relationship between the interplanar distance and lattice spacing.

For an example, for the cubic system, relationship is given below.

$$d = \frac{a}{\sqrt{h^2 + k^2 + l^2}} \quad 2.2$$

where,

a = lattice spacing of the cubic crystal

h, k, l = Miller indices of the Bragg plane

X-ray diffraction can be used either to single crystal samples or powder samples. In this work, X-ray diffraction of powders was used to characterize the materials with different doping levels to identify the structural transition along the solid solution range.

2.2.1 Single crystal X-ray diffraction

Single crystal X-ray diffraction is a non-destructive analytical technique and it provides detailed information about the internal lattice of crystalline substance (e.g. unit cell dimensions, bond-lengths, bond-angles, and details of site-ordering). This technique is directly related to single-crystal refinement, where the data generated from the X-ray analysis is interpreted and refined to obtain the crystal structure.

2.2.2 Powder X-ray diffraction (PXRD)

Powder diffraction has played a major role in structural physics, chemistry and materials science over the last thirty years. Important advances in structural studies of materials ranging from high temperature superconductors, complex metal oxides, zeolites, high pressure research, and temperature dependant research have relied heavily on this technique. The sample is typically a polycrystalline powdered material which is composed of many crystallites, thus it is possible that more than one crystal can satisfy Braggs's law. Hence from a powder, the diffracted beams are cones of electron density reflected from the Miller planes (hkl), which resemble rings on the screen. These rings can be indexed and integrated to obtain a powder pattern. PXRD is generally used to identify unknown substances, by comparing diffraction data against a database (i.e. the International Centre for Diffraction Data- ICDD). Rietveld refinement can be used to obtain the structural information of materials.

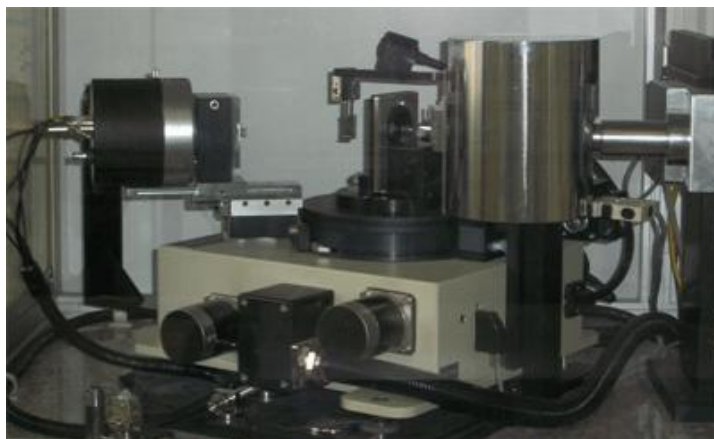


Figure 2.2: Image of the Stoe STADI/P powder diffractometer used in the lab with transmission geometry



Figure 2.3: Image of the Stoe STADI/P powder diffractometer used in the lab with reflection geometry

Phase purity, identity and homogeneity were confirmed by X-ray powder diffraction using following instruments in this work.

Phase purity was examined by X-ray diffraction analysis of powders on a Stoe STADI/P powder diffractometer (using Phillips transmission mode and George reflection mode

diffractometers). Incident radiation was generated using a CuK α 1 source (CuK α 1 = 1.54056 Å).

In-situ X-ray diffraction analysis of powders were collected at room temperature on a Bruker Axs D8 advance diffractometer equipped with a Lynxeye detector in the 10-90° range (CuK α =1.54 Å).

The high temperature diffraction data were collected in the 10–90° range, on a Bruker Axs D8 advance diffractometer equipped with a high temperature Anton Paar HTK 1200N chamber and a one dimensional X-ray detector VÅNTEC-1 (CuK α =1.54 Å).

2.2.3 Rietveld refinement

Rietveld refinement was developed by Hugo Rietveld (121,122) for the characterisation of crystalline materials. X-ray and neutron diffraction of powder samples results in a pattern characterised by reflections (peaks in intensity) at certain positions. Also the height, width and positions of these reflections are useful to determine many aspects of the crystal structure. The Rietveld method uses a least squares approach to refine a theoretical line profile until it matches the measured profile.

Solving a structure from powder diffraction data normally requires a long procedure. But nowadays several crystallographic software suites are available which makes data handling much easier.

In this research, ‘FullProf’ (123) was used to refine cell parameters at room temperature and also temperature dependant X-ray diffraction data. ‘GSAS’ (124) was used to refine cell parameters of room temperature neutron diffraction data.

2.2.4 FullProf software (123)

FullProf is a software program which is capable of Rietveld analysis (structure profile refinement) of neutron or X-ray powder diffraction data collected as a function of the scattering variable 2θ . Moreover, it also can be used as a Profile Matching tool, without the knowledge of the structure. Single crystal refinements can also be performed alone or in combination with powder data.

2.2.5 General Structure Analysis System (124)

GSAS is a software package for the refinement of structural models to both x-ray and neutron diffraction data. Similar to the FullProf it can be used with both single-crystal and powder diffraction data (Rietveld analysis), or even both simultaneously. Neutron data can be either from single-wavelength instruments or time-of-flight instrumentation.

2.3 Electron diffraction

Electron diffraction (ED) is a technique used to study matter by firing electrons at a sample and observing the resulting interference pattern. This technique is similar X-ray and neutron diffraction. Electrons can also be regarded as a wave. Electrons have the wavelengths orders of magnitude smaller than the interplanar spacing in most crystals (e.g for 100 keV electrons $\lambda < 3.7 \times 10^{-12}$ m. Typical lattice parameters for crystals are around 0.3 nm). This technique is frequently used in solid states physics and chemistry.

Low energy electron diffraction which is known as LEED is a surface science technique which is used to determine the surface structures of crystalline materials by bombarding with

low energy electrons ($\sim 10\text{-}200\text{ eV}$) and then obtained diffracted electrons as spots on a phosphorescent screen.

ED experiments are usually performed in a transmission electron microscope (TEM), or a scanning electron microscope (SEM) as electron backscatter diffraction. Electrons are accelerated by an electrostatic potential in order to attain the desired energy and determine their wavelength before they interact with the sample.

Electron diffraction is a collective scattering phenomenon with electrons being scattered by atoms in a regular array. As in X-ray diffraction the scattering event can be described as a reflection of the beams at planes of atoms. According to Bragg's law, wavelength λ of the electrons is known, therefore interplanar distances can be calculated from ED patterns.. Therefore similar to X-ray and neutron diffractions, electron diffraction is also a valuable tool in crystallography. Also, high resolution electron microscopy (HREM) and electron diffraction can be used to study the cation ordering and defects in crystals.

2.4 Selected area electron diffraction

Selected area electron diffraction (SAED), is a crystallographic experimental technique that can be performed inside a transmission electron microscope which can be analyzed to give information about the structure of the specimen. SAED is referred to as 'selected area' because it allows selecting and recording the diffraction pattern from the specific area of the specimen by user. In TEM a thin crystalline specimen is subjected to a parallel beam of high-energy electrons. The atoms act as a diffraction grating to the electrons which are diffracted. Therefore some fraction of them will be scattered to particular angles which determined by the crystal structure of the sample, while others keep on passing through the sample without deflection. Hence the image on the screen of the TEM will be a progression of spots and each

spot corresponding to a diffraction condition of the sample's crystal structure. SAED patterns are a projection of the reciprocal lattice and these SAED patterns can be used to identify crystal structures and also it can be used to measure lattice parameters.

2.5 Scanning electron microscopy

Scanning electron microscope is a type of electron microscope which focuses a beam of high energy electrons to scan the surface of a specimen. Electrons interact with the atoms that make up the sample producing signals which allows an image to be created by analysis of the secondary electrons and back-scattered electrons. SEM provides a variety of information about the sample (e.g surface topography, composition, and other properties such as electrical conductivity). SEM also has many advantages over the traditional light microscope such as SEM shows higher magnification, higher resolution and large depth of field yielding a characteristic three dimensional appearance useful for understanding the surface structure of a specimen.

2.6 Energy dispersive X-ray spectroscopy

The interaction of an electron beam with a sample produces variety of emissions including X-rays. These characteristic X-rays are used to identify the composition and measure the abundance of elements in the sample. A specific technique is known as Energy dispersive X-ray spectroscopy (EDX) which is used for the elemental analysis and chemical characterization of a sample. Its characterization abilities are due in large part to the basic principle that each element has a unique atomic structure allowing X-rays that are characteristic of an element's atomic structure to be identified. The elemental ratios can be determined from the EDX spectra and therefore this data can be used to examine the doping level, compositional percentage of a given sample area.

In this work selected area electron diffraction patterns for the T'' phase were collected in different orientations on a Jeol JEM-2011 electron microscope operated at 200 kV (figure 2.4).

Scanning electron microscopy Joel JSM-5600 was used to identify the morphology the sample (figure 2.5). EDX was used to identify some compositions of the sample.



Figure 2.4: Image of Jeol JEM-2011 electron microscope used in the lab

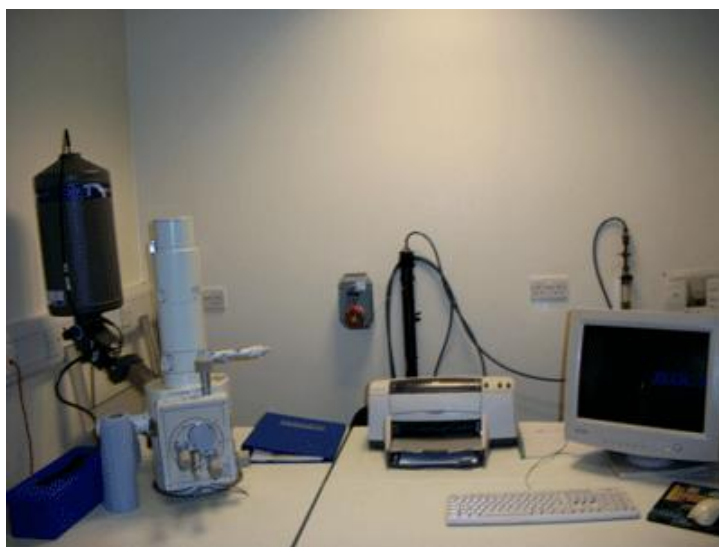


Figure 2.5: Image of Jeol JSM-5600 scanning electron microscopy used in the lab

2.7 Neutron diffraction

Neutron diffraction is a technique where neutrons are used to determine the atomic or magnetic structure of a material. It is similar to X-ray diffraction but due to the different scattering properties of neutrons compared to X-rays, complementary information can be obtained.

A neutron beam is used to perform a diffraction experiment on a crystalline sample and it will scatter at a limited number of well-defined angles according to Bragg's law. These diffraction investigations are possible because thermal neutrons have energies with equivalent wavelengths near 0.1 nm and are therefore ideally suited for inter atomic interference studies in crystal structures. Neutron diffraction has the ability to show strong well defined diffraction peaks with low d-spacing at low temperatures. Neutrons are uncharged, therefore it can penetrate deeply, thus it is easy to study the bulk and can be used in furnace, cryostat, and pressure cells. There are certain types of chemical structures which can be investigated

more readily by neutron diffraction than by X-ray diffraction. The most important application of neutron diffraction in crystallography is the structure determination of crystals which contain both heavy and light atoms (e.g hydrogen). The interaction of the magnetic moment of the neutron with the orbital and spin moments in magnetic atoms makes neutron scattering a unique tool for the study of a wide variety of magnetic phenomena. As a result, detailed information can be obtained on both the magnitude and orientation of magnetic moments in substances, which displays magnetic properties.

High resolution and high intensity time-of-flight neutron powder diffraction (NPD) data were collected for T'' phase using GEM diffractometer at the ISIS spallation source at Rutherford Appleton Laboratory, UK. The sample (ca. 5 g) was loaded into a thin-walled, cylindrical vanadium can and placed in the sample chamber in ambient condition.

2.8 Thermal analysis.

Thermal analysis is a technique where the physical properties of materials can be studied as they change with temperature. Several methods were used in this work but they are distinguished from one another by the property which is measured.

- Differential thermal analysis (DTA): temperature difference
- Differential scanning calorimetry (DSC): heat difference
- Thermogravimetric analysis (TGA): mass

Simultaneous thermal analysis (STA) normally refers to the simultaneous application of thermogravimetry and differential scanning calorimetry to one and the same sample in a single instrument. The test conditions are entirely the same for the TGA and DSC signals (e.g same atmosphere, gas flow rate, vapour pressure of the sample, heating rate, etc). The

essence of all these techniques is that the sample's response is recorded as a function of temperature and time.

Temperature can be controlled in a predetermined way, either by continuous increase or decrease in temperature at a constant rate or by carrying out a series of determinations at different temperatures with isothermal measurements. In addition to that it can control its environment with different atmospheres, e.g. measurements can be carried out in air or under an inert gas (e.g. nitrogen or helium). Moreover, measurements can be carried out under reducing or oxidizing atmospheres. This technique can be used to study phase transitions of the materials.

2.8.1 Differential Thermal Analysis

DTA is a thermal analysis techniques used to determine the thermal properties and phase changes of a material. It involves heating or cooling a test sample against an inert reference under the same conditions while recording any temperature difference between the sample and reference. Thermal conductivities and the heat capacities of the test and reference samples are not the same. This differential temperature is then plotted against time or against temperature. Changes in the sample which lead to the absorption or evolution of heat can be obtained relative to the reference sample. The baseline of the DTA curve should display discontinuities at the transition temperatures and the slope of the curve at any point will depend on the microstructure formation at that particular temperature.

2.8.2 Differential scanning calorimetry

Differential scanning calorimetry is a thermoanalytical technique in which the difference in the amount of heat required to increase the temperature of a sample and reference is measured as a function of temperature. Both the sample and the reference are maintained at equal temperature throughout the experiment. Temperature program for a DSC analysis is designed that the sample holder temperature increases linearly as a function of time. The reference sample should have a well defined heat capacity over the range of temperatures to be scanned.

The principal of this technique is that when a sample undergoes a physical transformation (e.g. phase transitions) more or less heat will need to flow to it than the reference to maintain both at the same temperature. Whether less or more heat must flow to the sample depends on whether it is an exothermic or endothermic process. When the sample undergoes exothermic processes such as crystallization less heat is required to raise the sample temperature. By observing the difference in heat flow between the sample and reference, DSC can measure the amount of heat absorbed or released by the sample during such transitions. Also it is used to observe more subtle phase changes (e.g. glass transitions).

2.8.3 Thermogravimetric analysis

Similar to the DTA and DSC, TGA also is a thermo analytical technique. TGA performs on samples that determine changes in weight with temperature. It involves heating a sample in an inert or different atmosphere and then measuring the change in weight. The weight change over particular temperature ranges offers indication of the thermal stability and the composition of the sample. It also provides information on estimation of moisture and

volatiles, oxidative stability, assessment of composition, and decomposition kinetics. TGA uses heat to force reactions and physical changes in materials and also it provides quantitative measurement of mass change in materials associated with transition and thermal degradation.

Simultaneous TGA-DTA/DSC measures both heat flow and weight changes (TGA) in a material as a function of temperature or time in a controlled atmosphere. Simultaneous measurement of these two material properties simplifies the interpretation of the results. Characteristic thermogravimetric curves are given for specific materials and chemical compounds due to unique sequence from physicochemical reactions occurring over specific temperature ranges and heating rates. These unique characteristics are related to the molecular structure of the sample.

In this work thermogravetric analysis was carried out on NETZSCH TG 209 instrument to evaluate the oxygen content (weight loss) at different temperatures and to compare with neutron diffraction results. The initial weight of the sample was about 20 mg. The effect of buoyancy was corrected using pre-empty crucible runs under corresponding gas atmosphere and flow rates. The samples were heated up to 900 °C in the TG furnace at a heating rate of 5 °C min⁻¹ in air.



Figure 2.6: Image of the NETZSCH TG 209 instrument used for thermogravimetric analysis

In order to understand any phase transition behaviour, simultaneous TGA/DSC was carried out using identical test conditions. Sample's response is recorded as a function of temperature.

2.9. Magnetization measurements

Magnetic fields are created mainly by the movement of charges and the intrinsic moment of elementary particles related with a basic quantum property, their spin. Some atoms show zero net magnetic moment due to pairing up of all the electrons; this pairing effectively cancel the moment. Materials which show no net magnetic moment are called diamagnetic materials. Most materials have one or more unpaired electrons which exhibit some magnetism. The magnitude of magnetic moment is the magnetic flux density (B) of a material which is given by eq 2.4.

$$B = \mu H \quad 2.4$$

Where,

B=Magnetic flux density (T)

H= Field Strength (Am^{-1})

μ = Absolute permeability of the medium (Hm^{-1})

The magnetic susceptibility of a material is the degree of magnetization shown by a material when an external magnetic field is applied. The magnetic susceptibility can be obtained by the equation given below

$$M = \chi H \quad 2.5$$

Where,

M= Intensity of magnetization induced by H (Am^{-1})

χ = Magnetic susceptibility

Experimentally, the magnetic susceptibility is measured as a function of temperature. The data obtained is then corrected for diamagnetic interactions using Pascal constants. The data can then be used to describe the magnetic interactions occurring inside the material. Therefore materials can be categorized by their response to externally applied magnetic fields as diamagnetic, paramagnetic and ferromagnetic while these magnetic responses vary significantly in strength. Diamagnetism is a property of all materials and opposes applied magnetic fields, but is very weak. Paramagnetism is stronger than diamagnetism and produces magnetization in the direction of the applied field, and it is proportional to the

applied field. Paramagnetic materials are those with unpaired electron spins, where each atom acts independently, resulting in relatively weak magnetic properties. Ferromagnetic effects are very large and produce magnetizations sometimes in orders of magnitude larger than the applied field. Therefore ferromagnetic effects are much larger than either diamagnetic or paramagnetic effects. Ferromagnetic materials also have unpaired electron spins, but the magnetic moment of each atom is coupled to the others such that the electrons become parallel. A spontaneous magnetization can be seen in these materials even in the absence of an external field. Antiferromagnetic materials have unpaired electrons which are held in such an alignment that results in an equal number of spins in each direction, therefore there is no net magnetization. In ferrimagnetic materials the arrangement of spins are similar to antiferromagnetic materials but the sub lattices have unequal magnetic moment, this results in high magnetic susceptibility in these materials.

The magnetic measurements were carried out on MPMS superconducting quantum interference device (SQUID) magnetometer. Data were collected in a field 500 Oe in the temperature range from 200 K to 5 K. The data was recorded using zero field cooling (ZFC) as well as field cooled (FC). A SQUID magnetometer measures the magnetic moment of a material from which the magnetization and magnetic susceptibility can be determined. It is highly sensitive to the magnetic changes occurring in the sample as a function of temperature when an external magnetic field is applied. SQUID is a very sensitive magnetometer used to measure weak magnetic fields (e.g. sensitive enough to measure low field as low as 5×10^{-18} T) based on quantum effects in a superconducting loop. It is useful for many purposes in physics, chemistry, biology and medicine.

2.10 Electrical measurement

Electrical conductivities were measured using two point and four point techniques.

2.10.1 Conductivity

Electrical conductivity measures a material's ability to conduct an electric current. It is commonly represented by the Greek letter σ and its SI unit is Siemens per metre (Sm^{-1}).

$$\sigma = \frac{1}{\rho} \quad 2.6$$

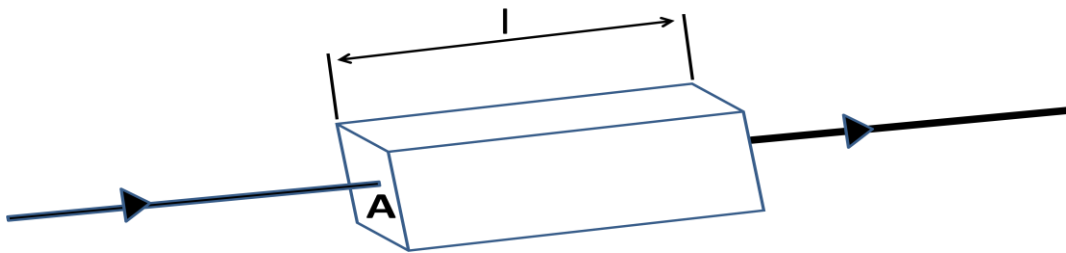


Figure 2.7: A piece of resistive material with electrical contacts on both ends

Electrical resistivity (ρ) is defined by,

$$\rho = \frac{E}{J} \quad 2.7$$

Where

ρ = Static resistivity ($\Omega\cdot\text{m}$)

E = Magnitude of the electric field (Vm^{-1})

J = Magnitude of the current density (Am^{-2})

Many resistors and conductors have a uniform cross section with a uniform flow of electric current and are made of one material.

In this case

$$R = \rho \frac{l}{A} \quad 2.8$$

Where

R = Electrical resistance of a uniform specimen of the material (Ω)

l = Length of the piece of material (m)

A = Cross-sectional area of the specimen (m^2).

The resistance of a given sample will increase with the length while it will decrease with greater cross-sectional area.

2.10.2. Two point measurement (lead compensated 2 point measurement)

In typical resistivity measurements 4 electrical leads (4 leads, two contacts) are attached to a cylindrical sample along a straight line. A current is fed between the two contacts while the voltage is measured across contacts. Current flow should be uniform and parallel between two contacts. The resistivity of the sample can be derived from the voltage drop across contacts, the applied current, and the geometry of the sample. Similar to this, simple

measurement of the electrical resistance of a test sample was measured by attaching four wires to the pellet (figure 2.8), electrical current was passed through the sample using two probes with the remaining two probes measuring voltage between these electrode, so compensating for lead resistance but not compensating for contact potential drop at interface. The voltage drop was measured by a digital voltmeter. Conductivities in air up to 900 °C were obtained.

Usually the resistance of the point of contact (called contact resistance) is much smaller than the resistance of sample, and can thus be ignored. Though, when one is measuring a very small sample resistance, especially under variable temperature conditions, the contact resistance can dominate and entirely obscure changes in the resistance of the sample itself. Effect of the contact resistance can be eliminated using four point DC technique, where the V across contacts is separated.

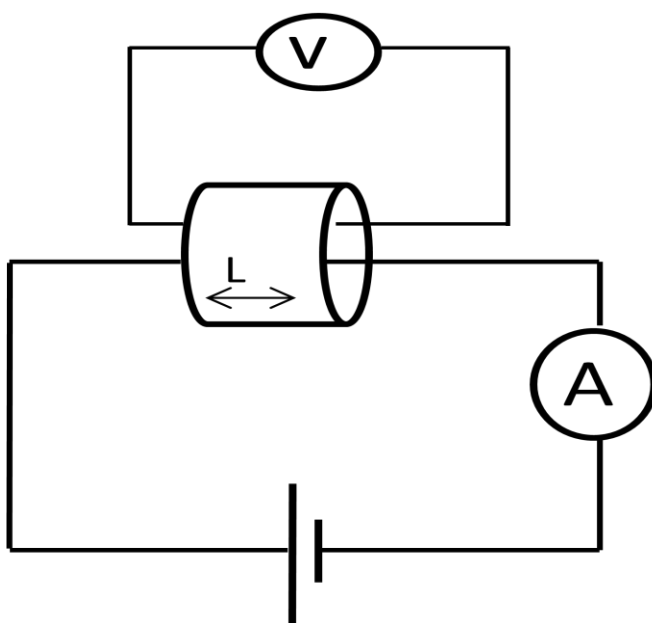


Figure 2.8: A schematic diagram for 2 point DC conductivity test kit

2.10.3 Four point measurement

The four point electrical probe is a very useful technique used widely for the investigation of electrical phenomena. The effects of contact resistance can be eliminated using of a four point probe DC technique (figure 2.9). If the sample has any resistance to the flow of electrical current, then there will be a drop of potential as the current flows along the sample, for example between the two probes labelled 2 and 3 in the figure 2.9. The voltage drop between probes 2 and 3 can be measured by using a digital voltmeter. The resistance of the sample between probes 2 and 3 can be obtained by the ratio of the voltage recording on the digital voltmeter to the value of the output current of the power supply. High impedance of the digital voltmeter minimizes the current flow through the portion of the circuit comprising the voltmeter. Therefore there is no potential drop across the contact resistance associated with probes 2 and 3. Only the resistance associated with the sample between probes 2 and 3 is measured. Therefore the four probe is a widely used technique for conductivity measurements.

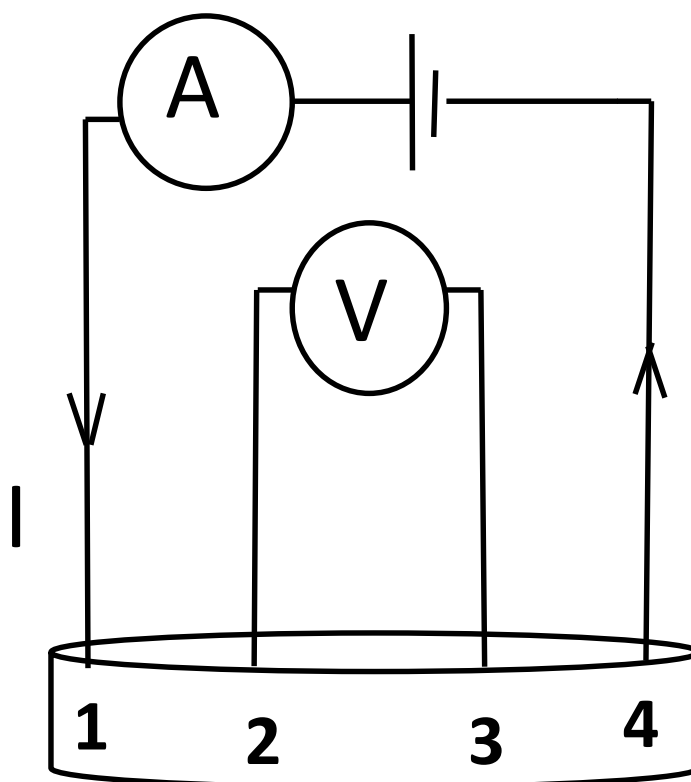


Figure 2.9: A schematic diagram for a 4 point DC conductivity test kit

Conductivities of the sample were obtained by 4 point DC technique. Final powders were uniaxially pressed into pellets using a pressure of 120 Mpa. The resulting 13 mm pellets were fired in air for 10 hours at 950 °C. Conductivity was measured using four point DC technique. Measurements were taken in air up to 900 °C. Effects of oxygen partial pressure were studied by introducing nitrogen or dry argon into the system. Measurement of the conductivity against oxygen partial pressure (measured via a YSZ sensor) were made at 1173K. For these measurements, the conductivity was initially taken in moving from oxidising to reducing conditions where nitrogen /dry argon was allowed to pass into the system. Then the pellet was cooled under reducing atmosphere.



Figure 2.10: The image of four point measurement test set up

2.10.4 Van der Pauw measurement

Determination of accurate geometry of the sample is difficult. Therefore one often used technique to determine the resistivity of the sample is Van der Pauw measurements (125,126). Due to its convenience, it is widely used in research and industry to determine the resistivity of uniform samples. A common geometry for such a measurement has 4 electrical contacts at the four corners (figure 2.10). However, the Van der Pauw technique is applicable for an arbitrary shaped sample, but in order to use this method accurately, the sample thickness must be much less than the width and length of the sample and it is preferable that the sample is symmetrical, thickness of the sample is known and is uniform, the contact areas are indefinitely small, and the contacts are all on the edge of the sample. In addition, there should not be any isolated pores or non conducting islands or inclusions within the sample. Leads from the contacts should be constructed from the same batch of wire and all four contacts should be of the same material (to minimise thermoelectric effects).

Several properties of a material can be obtained from the Van der Pauw measurements such as resistivity of the material, doping type (p-type or n-type) and sheet carrier density of the majority carrier (the number of majority carriers per unit area).

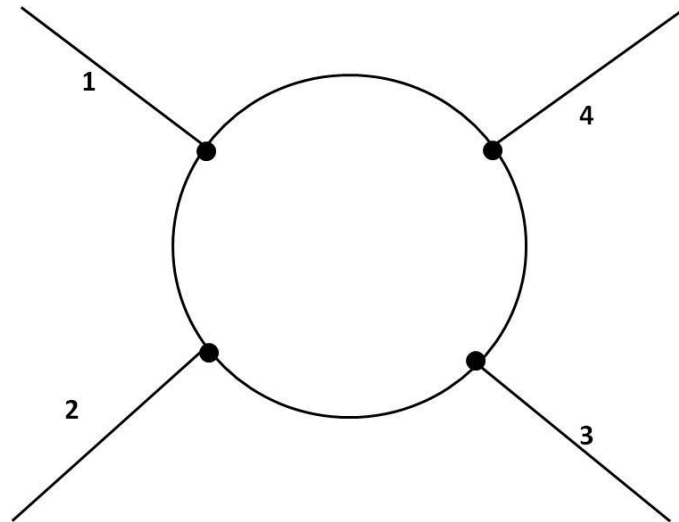


Figure 2.11: A schematic of a Van der Pauw configuration

- Contacts are numbered from 1 to 4 in a counter-clockwise direction
- The current I_{12} is a positive DC current injected into contact 1 and taken out of contact 2 (measured in amperes).
- The voltage V_{34} is a DC voltage measured between contacts 3 and 4 with no externally applied magnetic field (measured in volts).
- The sheet resistance R_S (measured in ohms).

To make a measurement, a current is caused to flow along one edge of the sample (for instance, I_{12}) and the voltage across the opposite edge (in this case, V_{34}) is measured. From these two values, a resistance (for this example, $R_{12,34}$) can be found using Ohm's law:

$$R_{12,34} = \frac{V_{34}}{I_{12}} \quad 2.9$$

Van der Pauw discovered that the sheet resistance of samples with arbitrary shape can be determined from two of these resistances, one measured along a vertical edge (such as $R_{12,34}$) and a corresponding one measured along a horizontal edge (such as $R_{23,41}$). The actual sheet resistance is related to these resistances by the Van der Pauw formula.

$$e^{-\pi R_{12,34}/R_s} + e^{-\pi R_{23,41}/R_s} = 1 \quad 2.10$$

Consequently, it is possible to obtain more precise values for the resistances $R_{12,34}$ and $R_{23,41}$ by making two additional measurements of their reciprocal values $R_{34,12}$ and $R_{41,23}$ and averaging the results.

Then, the Van der Pauw formula becomes

$$e^{-\pi R_{vertical}/R_s} + e^{-\pi R_{horizontal}/R_s} = 1 \quad 2.11$$

Accuracy of the resistance values can be obtained by repeating the resistance measurements after switching polarities of both the current source and the voltage meter. Since this is still measuring the same portion of the sample, just in the opposite direction, the values of $R_{vertical}$ and $R_{horizontal}$ can still be calculated as the averages of the standard and reversed polarity measurements.

Electrical properties were measured using small circular pellets. Powders were uniaxially pressed using a pressure of 120 MPa. The pellets had a diameter of 13 mm with a thickness

of 1-2 mm and were fired in air for 10 hours at 850 °C. In-situ conductivity was measured using a four point DC technique from 900 °C to room temperature in air using Van der Pauw technique for T'' phase.

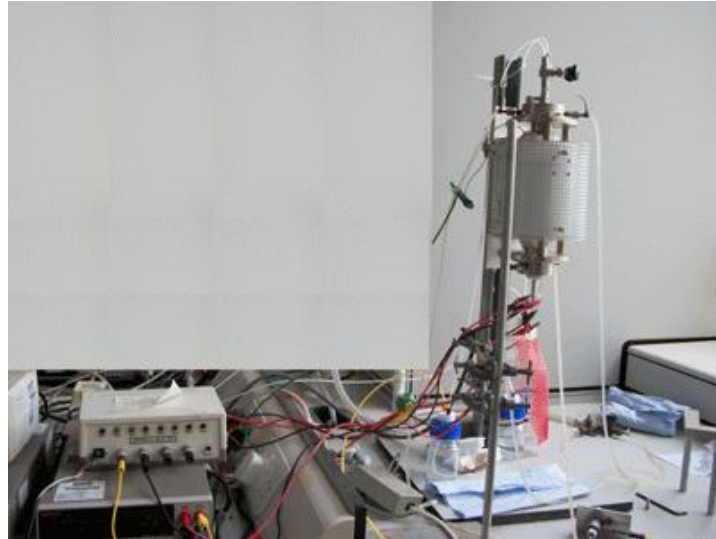


Figure 2.12: The image of Van der Pauw measurement test set up

2.11 Impedance measurement

Impedance (Z) describes a measure of opposition to current flow. Similar to resistance impedance, it is measured in ohms, but it accounts for the effects of capacitance and inductance. Effects of capacitance and inductance vary with the frequency of the current passing through the circuit, hence impedance is more complex than resistance. Therefore impedance varies with frequency. Electrical impedance extends the concept of resistance to AC circuits, describing not only the relative amplitudes of the voltage and current, but also the relative phases. When the circuit is driven with direct current (DC), there is no distinction between impedance and resistance and the latter can be thought of as impedance with zero phase angles. The effect of resistance is constant regardless of frequency.

When Ohm's Law applies directly to resistors in DC or in AC circuits, the form of the current-voltage relationship in AC circuits in general is modified to the form impedance (Z).

$$I = \frac{V}{Z} \quad 2.12$$

Ohms law,

$$I = \frac{V}{R} \quad 2.13$$

For a pure resistor $Z=R$, preserving the form of the DC ohm's law.

Combining impedances has similarities to the combining of resistors, but the phase relationships make it practically necessary to use the complex impedance method for carrying out the operations.

The technique involves applying an AC voltage (V) of varying frequency across the sample.

$$V=V_o \sin \omega t \quad 2.14$$

By convention, the current (I) leads the voltage by $\Phi=90^\circ$, so

$$I=I_o \sin(\omega t + \Phi) \quad 2.15$$

Impedance is a vector quantity and can be defined using complex numbers,

$$Z^* = Z' - jZ'' \quad 2.16$$

complex real imaginary

The magnitude and direction of the complex impedance Z^* can be expressed as real (Z') and imaginary (Z'') components. The complex impedance can be plotted by Cartesian (Z' vs Z'') or polar coordinates ($|Z|$ vs Φ).

Thus ,

$$Z' = |Z| \cos \Phi \quad 2.17$$

$$Z'' = |Z| \sin \Phi \quad 2.18$$

By measuring amplitude and the phase shift (Φ) of the current for any frequency (ω), with a fixed applied voltage (V) the impedance is calculated by using equation 2.12 and Z' and Z'' can be determined by 2.17 and 2.18.

2.11.1 Impedance spectroscopy (IS)

Impedance spectroscopy is a well-defined technique used to investigate and characterise the electrical properties and microstructure of a variety of ceramic material (127). AC impedance spectroscopy was first used by Bauerle (128) to examine the resistivities/conductivities of the different regions (bulk and grain boundary) of solid electrolytes, and effects due to electrodes. AC impedance methods permit easy identification of bulk, grain boundary and electrode effects. AC impedance spectroscopy has the advantage that individual components can be separated e.g. bulk, grain boundary, sample /electrode interface, allowing detailed

characteristics which helps to yield useful information about the physicochemical properties of the system (127). Using AC impedance spectroscopy, it is possible to analyse materials in which ionic conduction strongly predominates (e.g solid and liquid electrolytes, ionically conducting glasses and polymers). Also it has been used to study fuel cells, rechargeable batteries and corrosion and as well as to study dielectric materials with simultaneous ionic and electronic conductivity. Impedance spectroscopy is a versatile technique used nowadays to study the different fuel cell components (anode, cathode and electrolyte) under different atmospheres in order to optimize their electrical performance. Impedance spectroscopy measurements are simple in principle; analysis is generally carried out in the frequency domain, although measurements are sometimes made in the time domain. IS measurements on solids usually involves two identical plane, parallel electrodes. For this work, a frequency response analyser produced by Solartron was used which provide three or four terminal measurements. It is highly digitized, easy to handle and incorporates automatic frequency sweeps and automatic control of the magnitude of the applied ac signal and carries out the measurement automatically with high accuracy. A Solartron frequency response analyser covers very low frequencies to high frequencies (mHz to MHz levels). It determines impedance by correlating at each frequency, the response with two synchronous signals, one in phase with the applied signal and the other phase shifted by 90 degrees. This process yields the in phase and out of phase components of the response and leads to the various immitance components.

According to the application, it is necessary to analyse the data (e.g. when mobile charges are present, five major physical process may influence the data. There are bulk resistive – capacitive effects, electrode reaction, adsorption at the electrodes, bulk generation-recombination effects and diffusion). IS is a very useful technique for characterization of the electrical properties of material electrode systems. Its use for this purpose requires that

connections be known between model and / or equivalent circuit parameters and the basic characterization parameters. Depending on the situation, many different equivalent circuits can be used for IS fitting and no one circuit structure is appropriate for all situations. This can be easily done by using Zview software. ZplotR performs electrochemical impedance spectroscopy measurements which includes powerful ZView software for modelling and analysis (see section 2.8.2).

Cathode testing was carried out for symmetrical cells using impedance spectroscopy. Electrolyte gadolinia doped ceria (CGO) and yttria stabilised zirconia (YSZ) pellets were prepared. 10 mol% gadolinia doped ceria (CGO) and 8 mol% yttria stabilised zirconia (8YSZ) were used as the electrolyte phase in the symmetrical cell testing. Then YSZ and CGO pellets were made and fired for 4 hours at 1400 °C. The required amounts of $\text{Nd}_{1.85}\text{Pr}_{0.15}\text{CuO}_4$ powder, KD-I dispersant and acetone were weighted out and transferred to a milling bottle with an appropriate loading of milling balls. It was ball milled overnight using 160 rpm. Post milling, the contents of the bottle were discharged to a beaker and stirred via a magnetic stirrer while adding the cathode vehicle. The vehicle is a mixture of terpineol, and poly vinyl butyral. The contents of the beaker was stirred continuously in a fume cupboard while the acetone is allowed to evaporate until fully evaporated when the resulting ink was formed. Small amounts of slurry were applied to pellets of 8 mol% yttria stabilised zirconia (8YSZ) and 10mol% gadolinia doped ceria (CGO) by screen painting. The slurry was applied to both sides of the pellets. These layers were then fired in air for one hour at 1000 °C to create 1cm^2 porous electrodes in a symmetrical half cell arrangement. Before testing a Pt paint grid was hand painted on to the surface of the electrodes to facilitate current collection and ensure even current distribution at the triple phase boundary region. Then it was fired at 900 °C for 30 minutes. The specimen was held in an alumina holder with spring loaded Pt contacts within a tube furnace, with a thermocouple located close to the specimen to record

specimen temperatures. Experiments were carried out in air of the furnace. Impedance spectra were measured using a Solartron 1260 frequency response analyser with no DC polarisation using a frequency range of 1Mz to 0.01Hz and applied voltage amplitude of 50mV. Data were collected over a temperature range of 900 °C to 50 °C at 50 °C intervals and analysed using Scribner Associates Z-view software. Different models were tested using different layers arrangements e.g sub layer, 100% Pr-doped Nd_2CuO_4 (NPCO), 50% composite (chapter 3).

2.11.2 Equivalent circuit

Many components of the ceramic material can be obtained by AC impedance spectroscopy e.g bulk, grain boundary. Each component can be considered as consisting of a combination of resistive and capacitive elements. This combination of resistive and capacitive elements called equivalent circuit and depending on the properties of a material different combination will apply.

The resistance and capacitance of an unknown component can be determined by obtaining the real and imaginary impedance over a wide range of frequencies.

The resistance equals the real impedance when the frequency equals zero (at the intercept on the x axis).

The capacitance is called from the equation.

$\omega RC=1$ using frequency (ω) when Z'' is a maximum.

A real ceramic pellet can consist of many such parallel RC elements connected in series.

Computer software is now available to incorporate with these equivalent circuits with different models.

2.11.3 Capacitance values

Capacitance values can be calculated for any RC element and give an indication of what component of the material is being measured (Table 2.1). Similarly the magnitude of the capacitance of a bulk or grain boundary component can give an indication as to the degree of sintering of the ceramic.

Table 2.1 Capacitance values and their possible interpretations (127)

Capacitance (F)	Phenomenon responsible
10^{-12}	Bulk
10^{-11}	Second phase
$10^{-11} - 10^{-9}$	Grain boundary
$10^{-7} - 10^{-5}$	Sample –electrode interface
10^{-4}	Electrochemical reaction

2.11.4 Activation energy

The activation energy of conduction for any component could be obtained by measuring the change with temperature.

The slope of the Arrhenius plot ($\log \sigma T$ vs $1/T$) allowed the activation energy to be calculated.

$$E_A = (2.303 \times \text{slope} \times 1.38 \times 10^{-23}) / 1.6 \times 10^{-19} \quad (\text{eV}) \quad 2.19$$

Chapter 3- Praseodymium doped Neodymium Cuprates as a cathode material

3.0 Introduction

The objective of this chapter is to build upon these initial studies and investigate the structural characteristics and electrochemical properties of the Pr-doped Nd_2CuO_4 (NPCO) system and optimise its properties for SOFC cathode side applications. This chapter is divided into two main categories. The first part of the chapter discusses the characterisation of praseodymium doped neodymium copper oxide. The Pr-doped Nd_2CuO_4 system has been explored with respect to Pr content, temperature and oxygen partial pressure and it includes X-ray analysis data, microstructure of the pellets, two point measurement and finally four point measurement data. The second part of the chapter discusses the AC impedance measurements of electrochemical characteristics, where the use of $\text{Nd}_{2-x}\text{Pr}_x\text{CuO}_4$ as part of a cathode system (using pure NPCO and composite NPCO) was explored. Two types of current collectors were studied (Pt and NPCO).

Most of the AC impedance studies carried out on the cathode performance used idealized current collection with Pt. This however presents two issues, firstly that the utilization of Pt in the system is unrepresentative of a realistic cathode assembly as Pt would not be used in a commercial system. Secondly there are always some questions over the influence of the Pt on the measured performance of the system. With both of these aspects in mind it was decided to investigate the NPCO system which would approach something that would be suitable for integration into real world devices. In this work, therefore, we have explored Pt as well as NPCO for the current collection for symmetrical cell testing. In order to investigate the

performance of system is influenced by electrolyte material, both gadolinia doped ceria (CGO) and yttria stabilised zirconia were used as an electrolyte materials.

Measurements were taken using pure cathode material, as well as 50 % weight composite material with Pt current collector to discover any impact with composite material. Previous work in our lab (82) suggested that these type of materials (Ce doped Nd_2CuO_4) undergo significant microstructural development at typical stack conditioning temperatures (around 900 °C) and that it is also worth combining the current collection with that of an in-situ fired contact. Two fabrication routes for the current collector were investigated in this work; pre-firing and in situ-firing. Candidate structures were assessed in a symmetrical half cell arrangement using AC impedance. Mainly two types (Type 1 and Type 2) of testing arrangements were considered and schematic diagrams for these types are shown below (Figure 3.1 and Figure 3.2).

Type 1 – Pt as current collector

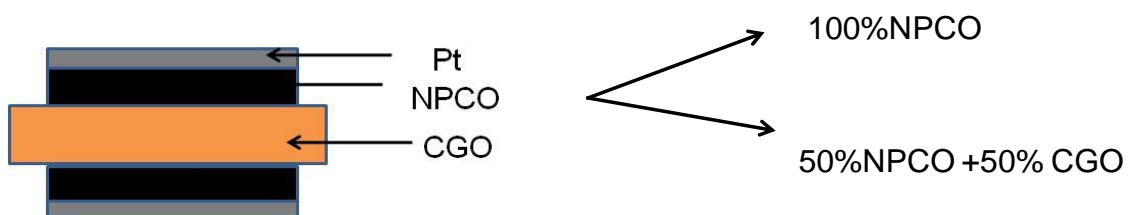


Figure 3.1: Schematic diagram of a symmetrical cell testing pellet used for Pt as current collector

Measurements were taken using 100% weight NPCO cathode material and 50 % weight composite material (NPCO: CGO) with Pt current collector . CGO was used as an electrolyte material for these systems.

Type 2 – NPCO as current collector

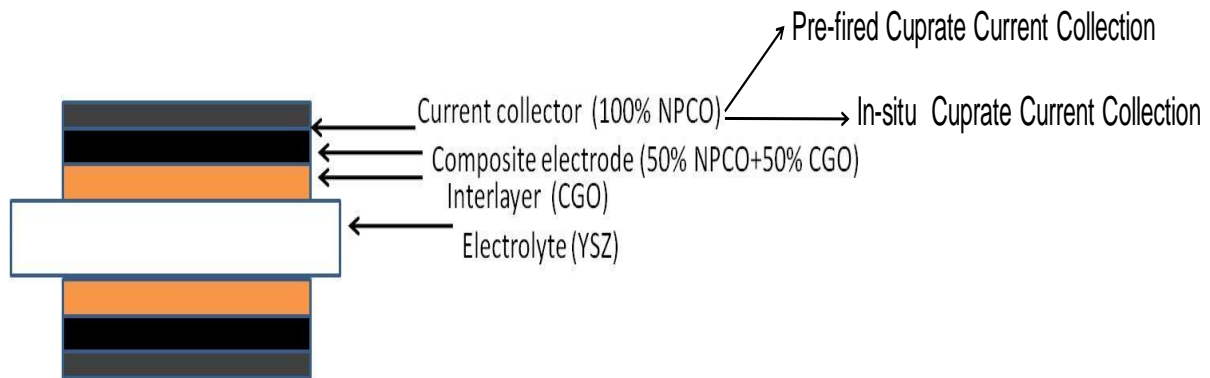


Figure 3.2.: Schematic diagram of a symmetrical cell testing pellet used for NPCO as current collector

For NPCO current collection, yttria stabilised zirconia (YSZ) was used as an electrolyte material while composite NPCO (50% weight NPCO: 50% CGO) was used as a cathode material. In order to prevent the reaction between YSZ and NPCO the CGO interlayer was painted. Furthermore, the porosity of this CGO sub layer also likely to lead to enhanced interfacial regions. Again two configurations were tested with different current collecting layers (an in-situ cuprate current collection and a pre fired cuprate current collection). From all of these studies, it was hoped to determine any possible applications for the NPCO system in SOFC applications.

3.1 Methods used

Experimental work can be divided in to two sub categories such as given below.

3.1.1. Characterisation of praseodymium-doped neodymium copper oxide.

3.1.2 Cathode testing using $\text{Nd}_{2-x}\text{Pr}_x\text{CuO}_4$.

3.1.1 Characterisation of praseodymium-doped neodymium copper oxide

Initial characterisation of praseodymium-doped neodymium copper oxide with respect to Pr content, temperature and oxygen partial pressure was performed to determine stability windows for possible high temperature SOFC applications. Electrical conductivity was determined with respect to both composition and temperature in order to determine which composition has the maximum conductivity and whether this remains so at different temperatures. $\text{Nd}_{2-x}\text{Pr}_x\text{CuO}_4$ (NPCO) materials have been produced as single phase composition over the range $0 < x \leq 0.25$, where $x=0.15$, 0.20 and 0.25 (NPCO15, NPCO20 and NPCO25 and) by a solid-state reaction.

The experimental procedure is given below.

Hygroscopic powders were dried for 30 minutes at temperatures up to 900°C . Stoichiometric amounts of Nd_2O_3 (Alfa-Aeser 99.9%), Pr_6O_{11} (Alfa-Aeser 99.9%), CuO (Aldrich 99+ %) were weighed and ground in acetone. The mixtures were then dried and treated in air up to 850°C for 36 hours. The resulting powders were reground (using a planetary ball mill) and the heat treatment was repeated (850°C for 36 hours). Compositions of NPCO were synthesised where $x=0.15$, 0.20 and 0.25 respectively. Finally the powders were analysed by XRD to identify if the final phase was present.

The powders were uniaxially pressed into pellets using 2 tons of pressure. The resulting 13 mm pellets were fired in air for 10 hours at 950 °C. Porous pellets were obtained with the theoretical density 74%. Conductivities of the pellets were tested using AC and DC techniques using two point measurements and four point measurements.

Two point measurement (4-probe) of the electrical resistance of test samples (NPCO15 and NPCO 25) were measured using AC and DC techniques by attaching four wires to the pellet and then current was passed through the sample using two probes. According to the resistance to the flow of electrical current, then there would be a drop of potential as the current flows along the sample. The voltage drop between those two probes was measured by digital voltmeter.

Conductivities for the pellets (NPCO15, NPCO20 and NPCO25) were also measured using four point DC technique. Measurements were taken in air up to 900 °C. The effect of oxygen partial pressure was studied by introducing one of two gases into the system. Dry argon was used for moderately reduced oxygen partial pressures (down to 10^{-4}) and humidified 5% H₂ in argon was used for lower partial pressures (down to 10^{-20}) which are more representative of SOFC anode conditions. Measurements of the conductivity against oxygen partial pressure (measured via a YSZ sensor) were made at 900 °C. For these measurements, the conductivity was initially taken in moving from oxidising to reducing conditions where hydrogen/dry argon was allowed to pass into the system. In this case, the change in $p(O_2)$ proceeds quite rapidly. The sample was then held under H₂/Argon atmospheres for at least 18½ hours in order to reach equilibration (the system under test) prior to any measurement being taken in the reverse direction (from reducing to oxidizing). The H₂/Argon flow was then turned off, and oxygen was allowed to leak back to the rig by natural leakage. Oxygen partial pressure

was monitored throughout the experiment via a YSZ sensor. The microstructure of the pellet was obtained using a scanning electron microscope.

3.1.2 Cathode testing

Two types of symmetrical cells were prepared and AC impedance was measured.

3.1.2.1 Pt as a current collector

Two types of cathodes were studied, pure (100%) NPCO15 and composites of cuprate and CGO 50:50 (wt%). Powders of NPCO were processed by various milling techniques to form inks which were applied to CGO pellets. These were then characterised by AC impedance.

Experimental procedure is given below.

Samples of NPCO20 were synthesised by solid state methods. Oxide powders, Nd_2O_3 (Alfa-Aeser 99.9%), Pr_6O_{11} (Alfa-Aeser 99.9%), CuO (Aldrich 99+ %) were weighed out in the appropriate stoichiometric ratios and were ground in acetone. The mixture was then dried and heat treated in air at 850°C for 36 hours. The resulting powder was then reground and the heat treatment repeated. The final powders were analysed by XRD in a Phillips diffractometer to identify the phases present.

Apart from that, the electrolyte CGO was prepared. 10 mol % of CGO (CGO10) was used as the electrolyte phase as well as the composite composition. CGO pellets were made and fired for 4 hours at 1400°C .

The required amount of NPCO15 powder, KD-I dispersant and acetone were weighed out and transferred to a milling bottle with an appropriate loading of milling balls (for composite composition, required amount of NPCO15, CGO10, KD-I dispersant and acetone were used). It was ball milled overnight using 160 rpm. Post milling, the contents of the bottle was discharged to a beaker and stirred via a magnetic stirrer while adding the cathode vehicle. The vehicle is a mixture of terpineol, and poly vinyl butyral. The contents of the beaker were stirred continuously in a fume cupboard while the acetone was allowed to evaporate until fully evaporated and the resulting ink was formed.

A small amount of slurry was applied to pellets of 10 mol % of gadolinia doped ceria by screen painting. The slurry was applied to both sides of the pellet. These layers were then fired in air for one hour at 1000 °C to create 1cm² porous electrodes in a symmetrical half cell arrangement.

Before testing, a Pt grid was hand painted on to the surface of the electrodes to facilitate current collection and ensure even current distribution at the triple phase boundary region. Then it was fired at 900 °C for 30 minutes. The specimen was held in an alumina holder with spring loaded Pt contacts within a tube furnace and with a thermocouple located close to the specimen to record specimen temperatures. Impedance spectra were measured using a Solatron 1260 frequency response analyser with no DC polarisation, using a frequency range of 1Mz to 0.01Hz and applied voltage amplitude of 50mV. Experiments were carried out in air and data were collected over a temperature range of 900 °C to 500 °C at 50 °C intervals and analysed using Scribner Associates Z-view software.

As these specimens were symmetrical, they consist of two nominally identical electrodes, therefore all of the data presented has been divided by two to obtain the polarisation resistance (Rp) value of a single electrode. To give a better impression of how the size and

shape of the spectra are in relation to one another, series resistance (R_s) has also been subtracted from the responses. To assess the microstructure of specimens, it was vacuum mounted in epoxy then sectioned and polished to a 1 micron diamond finish. Jeol JSM-5600 scanning electron microscopy was used for the SEM images.

3.1.2.2 NPCO as current collector

In this study 8% yttria stabilised zirconia (8YSZ) was used as the electrolyte and a CGO interlayer was used to prevent the reaction between cathode material and YSZ. Composites 50:50 (wt%) NPCO20 and 10 mol % CGO were used as the cathode material. Two configurations were tested (in-situ NPCO and pre-fired NPCO current collectors). Inks were formed by ball milling of mixed powders in acetone and dispersant, followed by dispersion into terpeneol/PVB vehicle. The experimental procedure is given below.

Samples of NPCO 20 were synthesised by solid state methods. Oxide powders, Nd_2O_3 (Alfa-Aeser 99.9%), Pr_6O_{11} (Alfa-Aeser 99.9%), CuO (Aldrich 99+ %) were weighed out in the appropriate stoichiometric ratios and were ground in acetone. The mixture was then dried and heat treated in air at 850 °C for 36 hours. The resulting powder was then reground and the heat treatment was repeated. The final powders were analysed by XRD with a Phillips diffractometer to identify the phases present.

Previous studies had shown that a 50:50 (by weight) composite of NPCO and 10 mol% gadolinia doped ceria (CGO10) produced a promising cathode structure. Therefore 50% weight NPCO was used as a cathode material for this work. Earlier work had revealed that the cuprate material is sinter active at temperatures of 900 °C -1000 °C and that to minimise

any over densification of the cathode layers a sinter temperature of no more than 1000°C would be required (82).

Therefore a high surface area (36 m²/g) CGO10 (Praxair Specialty Ceramics) was used in composites and interlayer. This material not only exhibits high levels of ionic conductivity in air, but also the fine structure would be more sinter active at the lower firing temperatures required by the NPCO.

To fabricate the composite ink, the NPCO powder was subjected to 30 minutes of high energy planetary ball milling in acetone to reduce the overall particle size from the solid state synthesis; this was then dried to form a refined NPCO powder. This refined powder was then roller ball milled for 18 hours with the CGO and a dispersant in acetone. Following this the slurry was mixed with the organic vehicle and the acetone was allowed to evaporate to form the final slurry. The solids loading of the final slurry was 65 wt%.

The pellets were uniaxially pressed from commercially available powder of YSZ (DKK HSY8) and fired for 4 hours at 1450 °C. To prevent the reaction between YSZ and NPCO, interlayer of CGO10 ink (Praxair 36 m²/g) was screen printed onto either side of the YSZ pellets and prefired at 1200 °C for 2 hours before the application of the cathode. Cathodes layers were applied by screen printing on to both sides of pellets to create a symmetrical half cell arrangement. These layers were fired in air for one hour at 1000 °C to create 1cm² porous electrodes.

Current collector inks were fabricated by mixing a calcined NPCO powder directly into an organic based screen printing ink vehicle using a mortar and pestle. This resulted in a viscous, coarse paste which was applied to the pre-sintered cathode by hand painting. Two

fabrication routes for the current collector were investigated in this work; pre-firing and in situ-firing. In the former, the current collecting layer was fired for 1 hour at 1000 °C prior to testing and for the in situ-firing, the current collector layer was dried at 80 °C after painting and fired within the electrochemical test cycle.

The specimen was held in an alumina holder with spring loaded Pt contacts within a tube furnace, with a thermocouple located close to the specimen to record specimen temperatures. Experiments were carried out in the static air volume of the furnace. Impedance spectra were measured using a Solatron 1260 frequency response analyser with no DC polarisation using a frequency range of 1Mz to 0.1Hz and an applied voltage amplitude of 50 mV. The specimens were heated at a rate of 2 °C min⁻¹ to a furnace temperature of 900 °C and allowed to equilibrate for one hour. In the case of the insitu-fired current collectors this constituted the firing cycle. Data was then collected over a furnace temperature range of 900 °C to 500 °C at 50 °C intervals and analysed using Scribner Associates Z-view software. As these specimens were symmetrical they consist of two nominally identical electrodes, therefore all of the data presented has been divided by two to obtain the R_p value of a single electrode. To give a better impression of how the size and shape of the spectra compare in relation to one another R_s has also been subtracted from the responses.

To assess the microstructure of each electrode, post test specimens were vacuum mounted in epoxy resin then sectioned and polished to a 1 micron diamond finish. Microstructural analysis was carried out by using Jeol JSM-5600 scanning electron microscopy.

3.2 Results and discussion

Results and discussion mainly divided in to two sub categories as shown below,

3.2.1. Characterisation of praseodymium doped neodymium copper oxide

3.2.2. Cathode testing

3.2.1 Characterisation of praseodymium doped neodymium copper oxide ($\text{Nd}_{2-x}\text{Pr}_x\text{CuO}_{4\pm\delta}$)

Basic characterisation was carried out using X-ray analysis data, microstructure of the untested NPCO pellets, two point AC and DC electrical measurements for NPCO15 and NPCO25 compositions and finally four point DC electrical measurement for NPCO15, NPCO20 and NPCO25 compositions with respect to temperature and Oxygen partial pressure.

3.2.1.1 X-ray analysis data

Figure 3.3 shows the x-ray diffraction patterns for the various powders synthesised during this work. $\text{Nd}_{2-x}\text{Pr}_x\text{CuO}_{4\pm\delta}$ materials were produced over the range $0.15 \leq x \leq 0.25$ and these match published patterns for tetragonal T' phase with $I4/mmm$ space group.

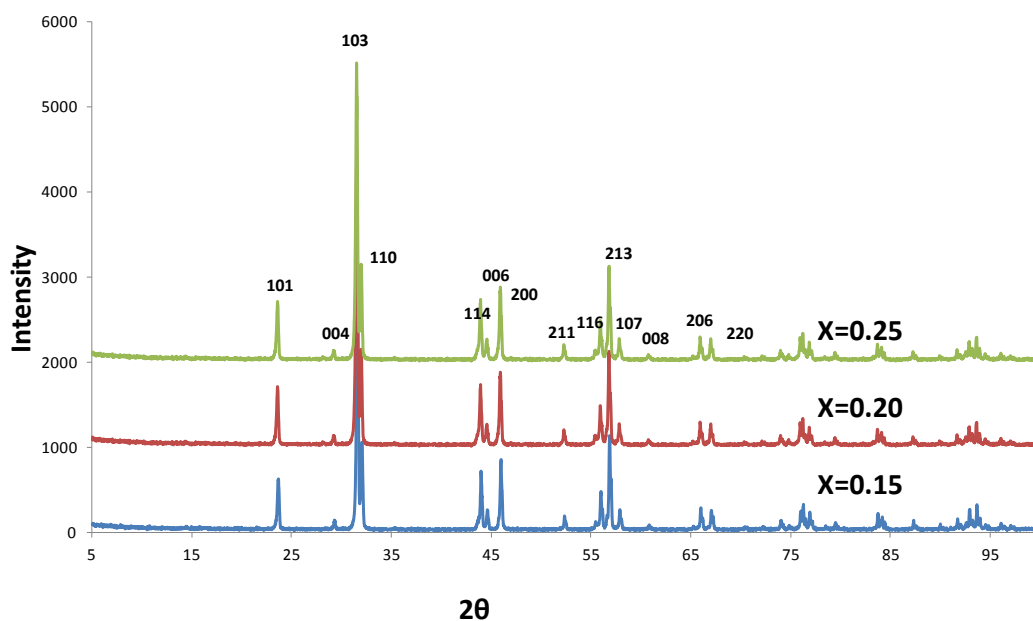


Figure 3.3:. X-ray patterns for the different $\text{Nd}_{2-x}\text{Pr}_x\text{CuO}_4$ compositions

X-ray diffraction data indicate that NPCO is phase pure across all of these dopant concentrations suggesting a wider range of solubility for Pr. This may not be too unexpected when one considers that the atomic radius of Pr is closer in size to Nd.

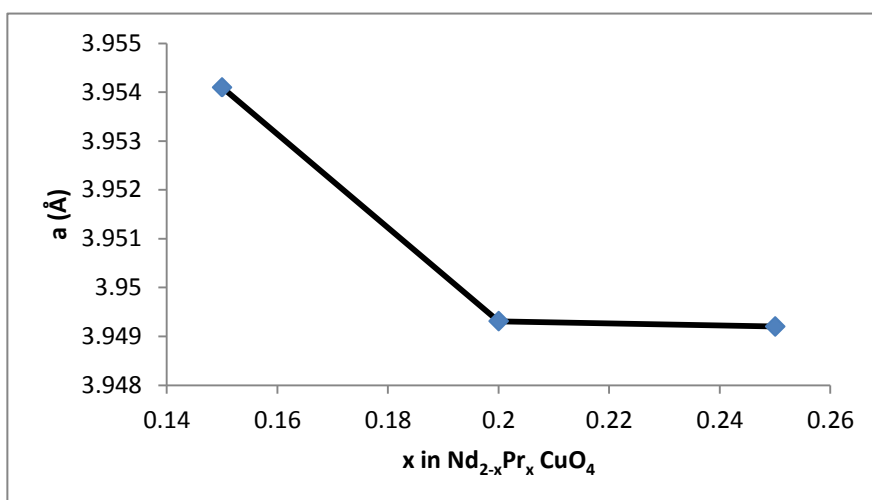


Figure 3.4: Lattice parameters a of $\text{Nd}_{2-x}\text{Pr}_x\text{CuO}_4$ versus x

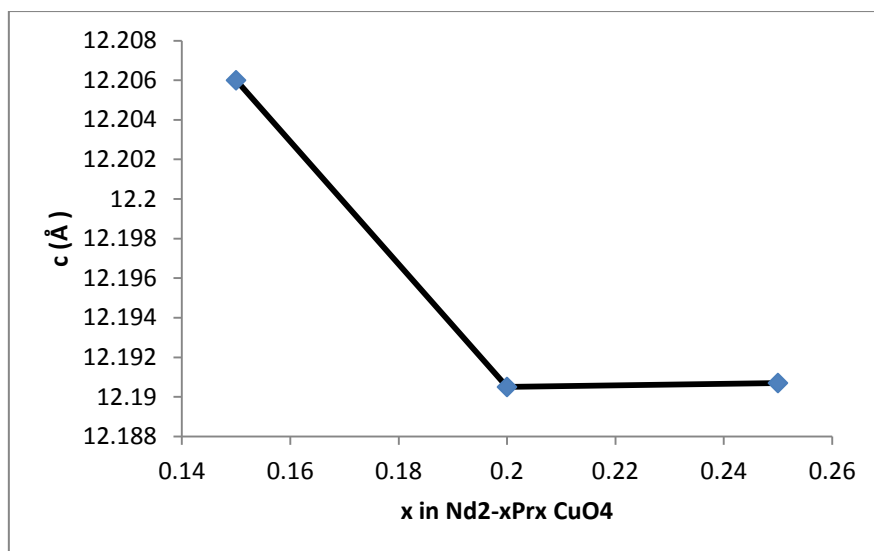


Figure 3.5:. Lattice parameters a of Nd_{2-x}Pr_x CuO₄ versus x

When increasing x the a-axis and c-axis decrease due to the smaller ionic radius of Pr⁴⁺, it also suggests that the limiting point of the solid solution of Nd_{2-x}Pr_xCuO₄ substitution ratio is around x=0.2, but in order to understand the exact value of limiting point, it is much better to synthesise the Nd_{2-x}Pr_xCuO₄ series between substitution ratio 0.2 to 0.25 with smaller increment.

3.2.1.2 Microstructure of the pellets

Electron microscopy can be used for both microstructural characterization and for determining compositional variation within a solid. Figure 3.6 and 3.7 show the SEM images of NPCO15, NPCO25 untested pellets respectively. These figures illustrate that the particle size is *ca* 3-5µm and porous structures of the pellets for NPCO. Porous structure is important for cathode as it facilitate the gas diffusion along the material.

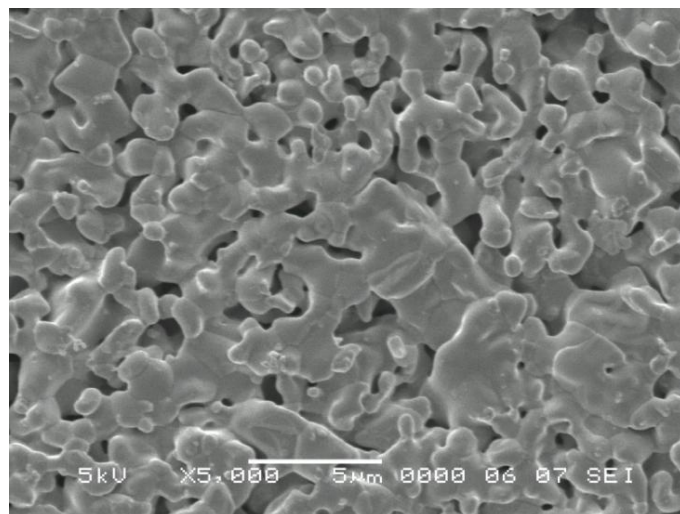


Figure 3.6: SEM image of an untested pellet NPCO15

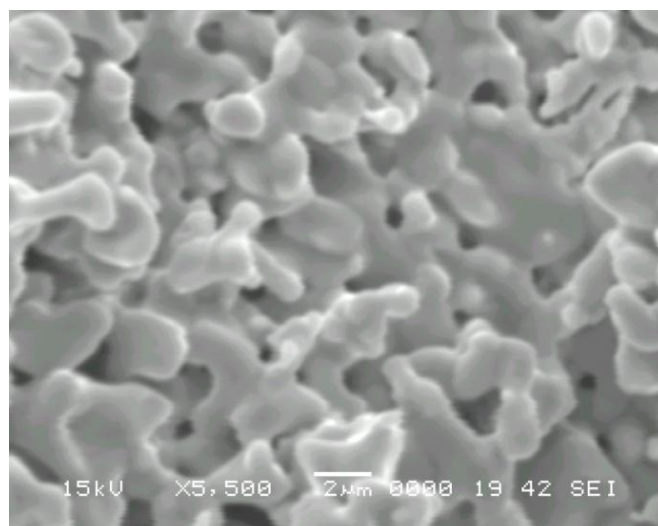


Figure 3.7:. SEM image of an untested pellet NPCO20

3.2.1.3 Two point measurement

DC and AC conductivities were measured using 2 point measurement (lead compensated 2 point measurement). Conductivities in air (NPCO15, NPCO25) up to 900 °C were obtained, but conductivities show (figure 3.8) much lower than expected values (40-80 Scm^{-1}).

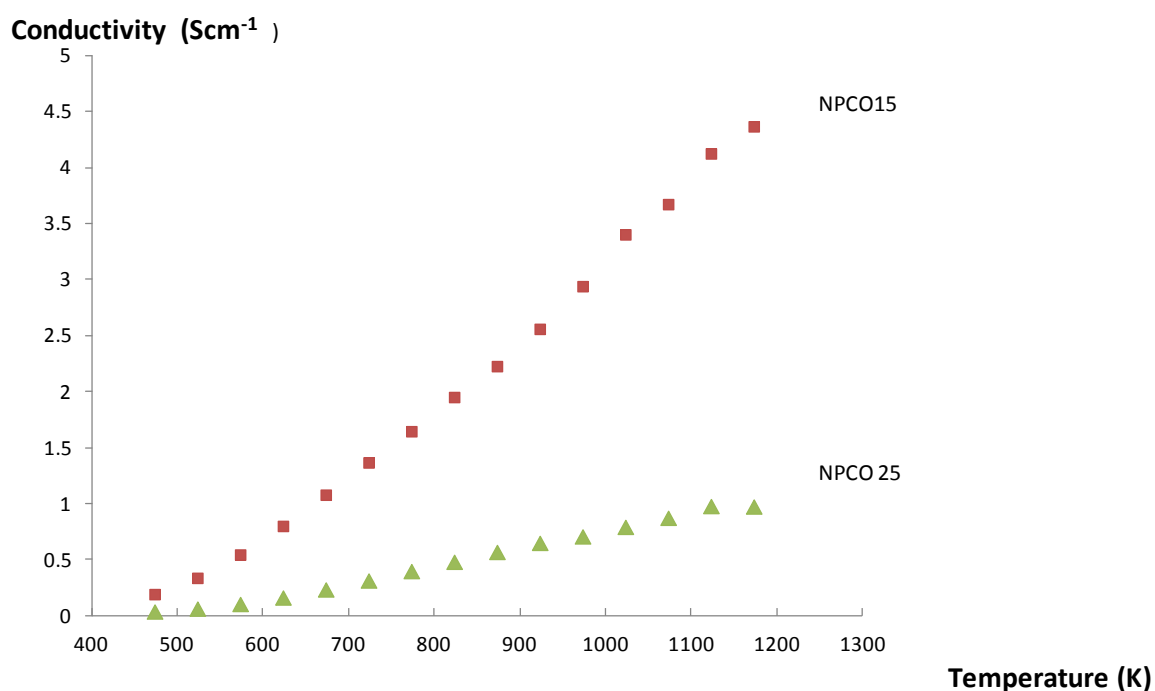


Figure 3.8: DC Conductivities of NPCO15 and NPCO25 in air

This could be due to high contact resistance which is not in the same magnitude with the pellet resistance. Typically the resistance of the point of contact is far smaller than the resistance of the sample, therefore it can be ignored. But, when one is measuring a very small sample resistance, the contact resistance can dominate and for this reason completely obscure changes in the resistance of the sample itself. The effect of the contact resistance can be eliminated using a four point DC technique.

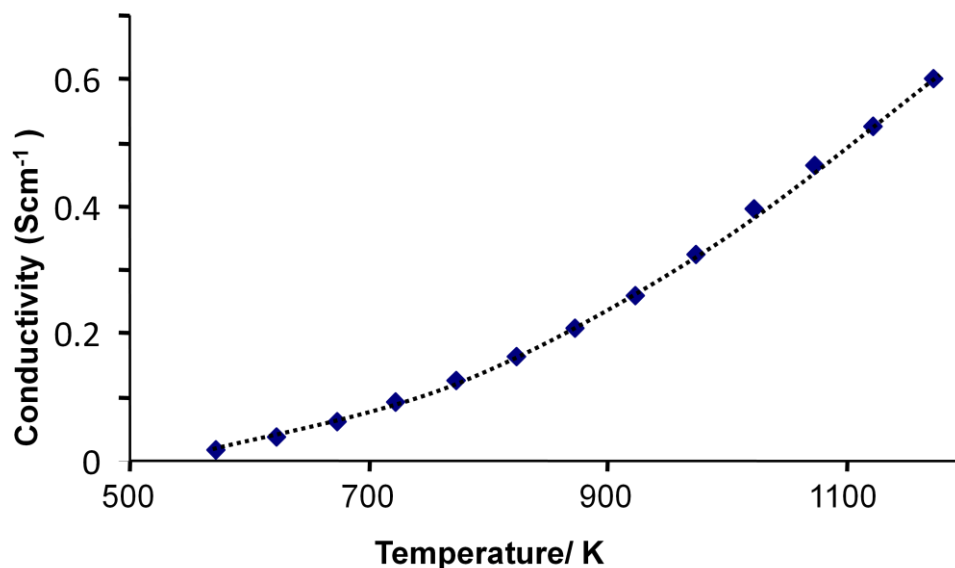


Figure 3.9: AC conductivity for NPCO15 obtained from impedance spectra

In order to compare the AC conductivities (figure 3.9), impedance was measured for the same pellet NPCO15 in air up to 900 °C by employing a two point probe. In order to get compensate for the lead resistance, impedance of the Pt wires was measured in all the temperatures. Figure 3.8 and 3.9 show that AC and DC conductivities for the NPCO15 are nearly the same but the conductivities are much lower compared to the expected value. This is probably due to high contact resistance. In order to eliminate that, four point DC measurements were carried out for sample NPCO.

3.2.1.4 Four point measurement

Conductivities for the NPCO in air and conductivity at different oxygen partial pressures were measured using the four probe DC technique. These were measured after the same amount of time on test and suggest that a maximum conductivity may exist close to a dopant level of $x = 0.25$.

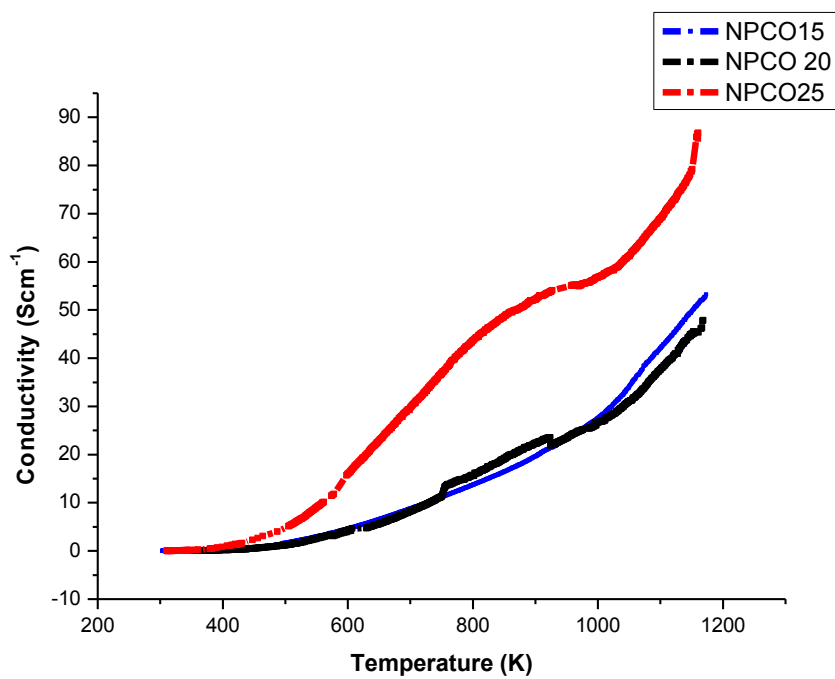


Figure 3.10: Comparison between DC conductivities in $\text{Nd}_{2-x}\text{Pr}_x\text{CuO}_4$ where $x=0.15, 0.20$, and 0.25 in air up to 900°C

Table 3.1: NPCO conductivities in air

Composition	σ at 900 K (Scm^{-1})	σ at 1000 K (Scm^{-1})	σ at 1160 K (Scm^{-1})	Activation energies obtained from the slope (eV)
NPCO15	19.8	27.6	52.3	0.31
NPCO20	22.4	26.7	47.9	0.33
NPCO25	52.2	56.84	86.7	0.33

The highest conductivity was obtained for NPCO25 in air about 86.7 Scm^{-1} at 900°C . NPCO15 and NPCO20 show pure semiconductor behaviour without showing any semiconductor/metallic transitions while NPCO25 shows a slight different behaviour. This may be due to several reasons. These are metallic/ semiconductor transition, phase transition (two phase effect might change the microstructure), or the changes in the oxygen stoichiometry (oxygen loss on heating). Refinement of X-ray diffraction data suggests (figure 3.4 and figure 3.5) that the limiting point of the solid solution is around $x=0.2$ substitution ratio. So, if we increase the Pr beyond 0.2 levels, it will not be in the same matrix. Therefore these NPCO25 compositions may adopt different behaviour compared to the NPCO15 and NPCO20 compositions.

In order to understand the thermal activation process Arrhenius plots, $\log \sigma T$ vs $1000/T$ for NPCO15, NPCO20 and NPCO25 were plotted (Figure 3.11). Similar to the σ vs T plot, NPCO15 and NPCO20 have a similar behaviour for $\log \sigma T$ vs $1000/T$ while NPCO25 has a slightly different behaviour. The linearity of the plots ($\log \sigma T$ vs. $1000/T$) for NPCO15 and NPCO20 showed that the observed increase in conductivity are due to the thermal activation, probably due to small polaron conduction. But non linearity of the plot NPCO25 in figure 3.11 showed that the observed increase in conductivity was not just due to thermal activation. Maybe another mechanism is contributing for that composition, although, all the three compositions follow Arrhenius behaviour at low temperatures.

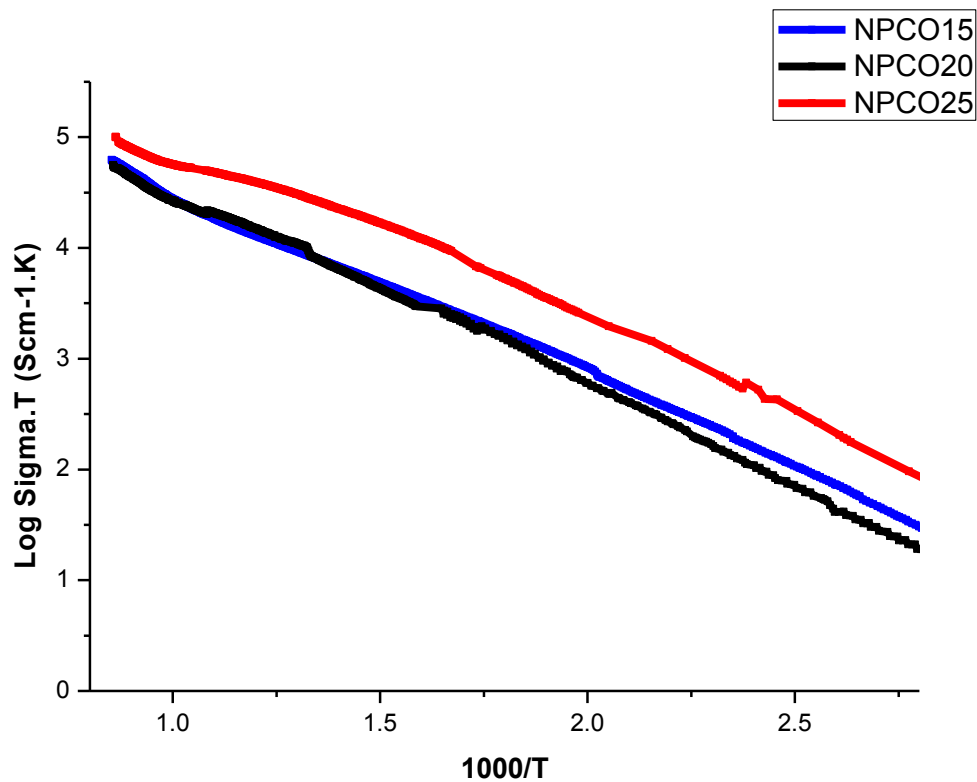


Figure 3.11:. Log σT vs $1000/T$ for NPCO15, NPCO20 and NPCO25 in air

It is interesting to see the material's behaviour, especially conductivity with respect to $p(\text{O}_2)$. To investigate this Argon was used to create a milder reducing atmosphere. Figure 3.12 shows the reduction-oxidation cycle of NPCO20 between air and argon at 900 °C.

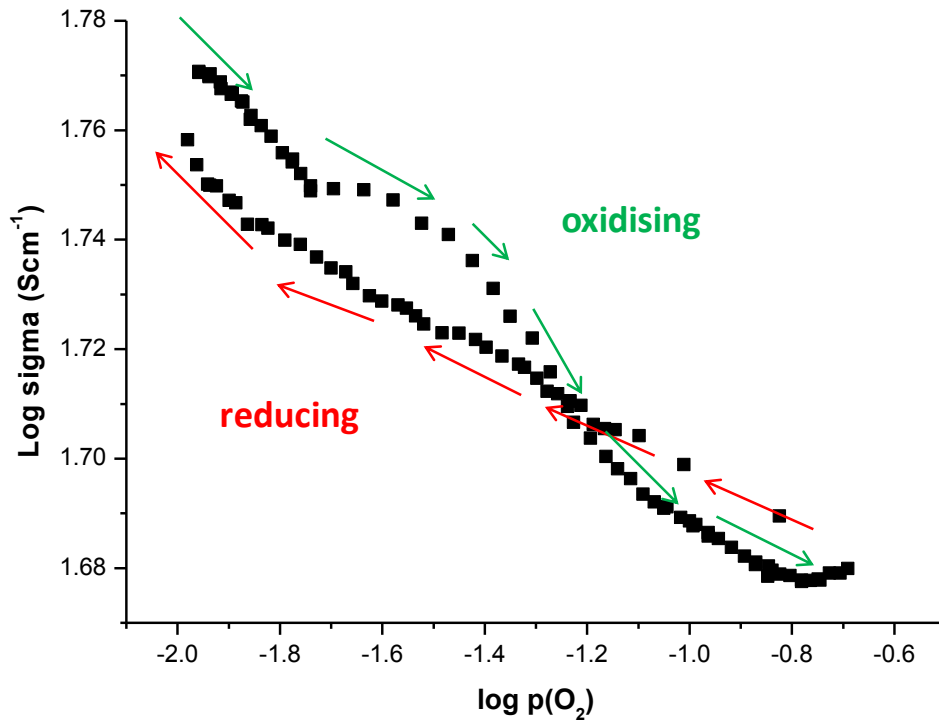


Figure 3.12: Log σ vs log $p(\text{O}_2)$ for NPCO20 in dry argon at 900 °C

It is known that the system loses oxygen when in reducing $p(\text{O}_2)$ atmospheres, in fact annealing in these conditions is a requirement in attaining superconductivity. At these partial pressures the conductivity of this material show some level of dependence on $p(\text{O}_2)$. However the NPCO data shows lower $p(\text{O}_2)$ dependence (gradient -0.08). The value of the observed slope is shallower than the classical defect slopes of $\pm 1/4$ or $\pm 1/6$ (82). This value is about - 1/12, which is $\frac{1}{2}$ of $1/6$ and might imply some charge disproportionation is involved.

From these experiments, the conductivity against oxygen partial pressure (until $\log p(\text{O}_2) 10^{-2}$) measurement showed an increase in conductivity with decreasing $p(\text{O}_2)$ which indicate that this material is an n-type semiconductor. This would imply that Pr stays in the system as a Pr^{+4} ion and introduces electrons to the system.

In order to see the fully reduced behaviour, hydrogen was used as a reducing atmosphere. Figure 3.13 shows the reduction of NPCO20 in hydrogen at 900 °C. In this experiment, the conductivity of pellets were measured as the oxygen partial pressure in the test jig was slowly allowed to decrease.

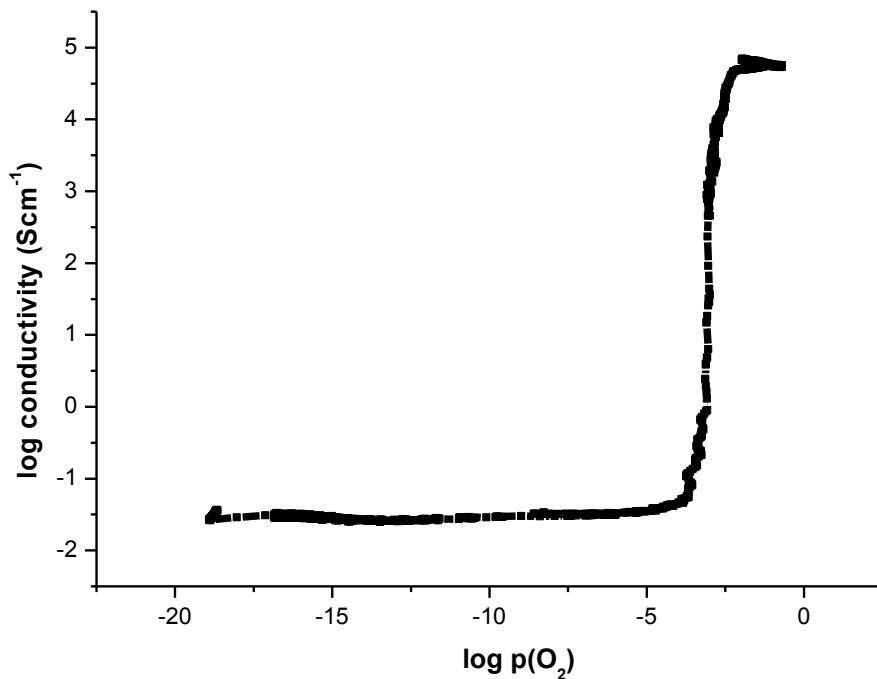


Figure 3.13: Plot of log conductivity versus log $p(\text{O}_2)$ for the NPCO20 composition (data was collected at 900 °C)

Sample behaviour is similar in Argon until it decomposes beyond 10^{-2} . This material shows an abrupt change in conductivity at values between 10^{-4} and $10^{-3.0}$. After full reduction with hydrogen, the sample is re-oxidized, then sample lost 20% of conductivity, that mean it is

not fully reversible. This can be presumably due to the reduction of the Pr^{4+} cation to Pr^{3+} , which is the same valence as the host Nd^{3+} cation therefore any charge carriers introduced by the higher valence Pr^{4+} are lost and conductivity will drop. However one must also consider the creation of Cu^{1+} cations within the CuO_2 planes and the effects of this on conductivity.

At oxygen partial pressure below around 10^{-4} atmospheres conductivity has been found to drop dramatically in representative anode conditions when the measured conductivities have been below 10^{-1} Scm^{-1} , which is far too low for anode current collection and distribution applications. This has been attributed to a reduction on the $\text{Cu}^{2+/1+}$ cation to Cu^0 .

After the full reduction with hydrogen, NPCO20 lost *ca* 20% conductivity. This may presumably be due to the sample decomposition in reduction and would not fully go back to the previous structure or it may be due to cracks in the pellet. Therefore SEM and EDX were used to investigate this further to see if there is any change in the microstructure or composition (figure 3.14 and 3.15).

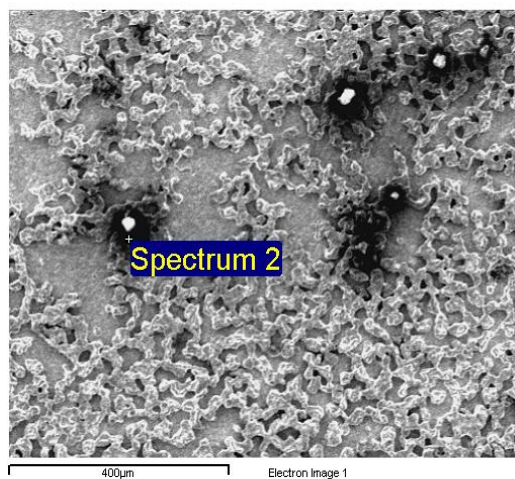


Figure 3.14: SEM image of tested pellet NPCO20 showing Cu is leaking out (black areas) of the pellet

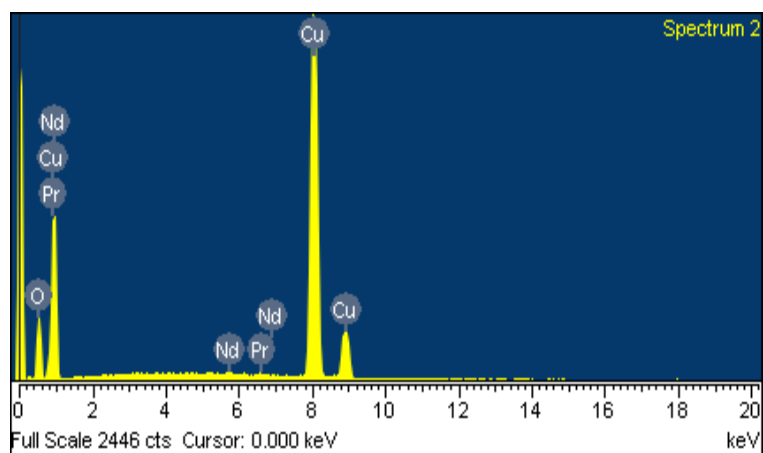


Figure 3.15: EDX obtained for spectrum 2 in SEM image showing increasing of Cu percentage

Table 3.2: EDX elemental analysing data as a percentage

Element	Weight%	Atomic%
O	22.62	53.86
Cu	76.60	45.93
Pr	0.15	0.04
Nd	0.63	0.17
Totals	100.00	

After the reduction with Hydrogen, the microstructure of the tested pellet (figure 3.14) indicated some black patches which were due to decomposition of the sample. To clarify this, EDX (Figure 3.15) was carried out to determine the composition of these areas. The percentage of Pr and Nd decreased while the percentage of Cu increased (Table 3.2). This was probably due to some CuO forming during the reduction since it would not go back to the previous structure or it may be due to Cu precipitation. Therefore, in order to reduce the oxygen partial pressure, argon can be used as a mild reducing agent for cuprate type materials. However, using this material for anode side application is problematic therefore in order to investigate the electrical behaviour in reduced atmosphere, dry Argon can be used as a mild reducing agent.

In order to investigate these changes due to sample instability, thermogravimetric analysis (TGA) was used to determine the NPCO changes in weight in relation to the change in temperature. It shows no significant mass change with the temperature change and the composition is reasonably stable in air up to 1200 K in air (figure 3.16).

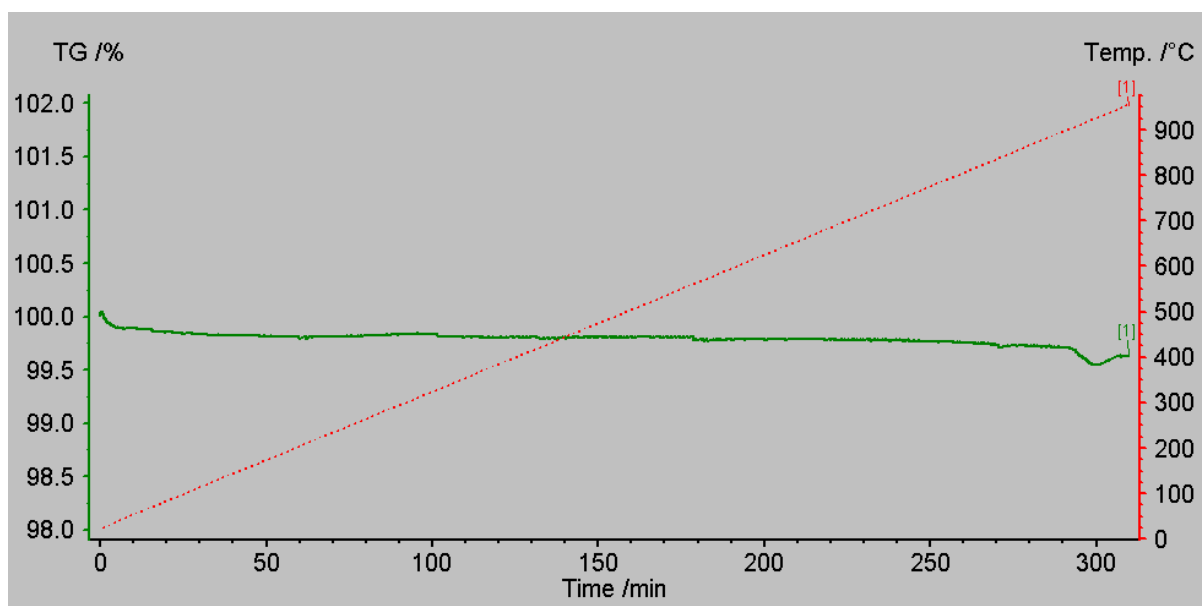


Figure 3.16: Thermogravimetric analysis of $\text{Nd}_{1.75}\text{Pr}_{0.25}\text{CuO}_4$ in air up to 950 °C

3.2.2 Cathode testing

Two types of current collectors (Pt and NPCO) were used for cathode testing. It has been shown in the previous section that NPCO possesses suitable conductivity for this role (around 52.3 Scm^{-1} , 47.9 Scm^{-1} , and 86.7 Scm^{-1} at 1160 K for different Pr substitution ratio of NPCO15, NPCO20 and NPCO 25 respectively). Candidate structures for cathode testing

were assessed in symmetrical half cell arrangements and direct electrochemical performance comparisons have been carried out using Ac impedance measurements at open circuit.

3.2.2.1 Pt as a current collector

Use of $\text{Nd}_{2-x}\text{Pr}_x\text{CuO}_4$ as part of a cathode system was explored with Pt as a current collector. Symmetrical cells were made with three steps as shown in as figure 3.17 (1. dense electrolyte 2. dense electrolyte with porous cathode material, 3. Pt grid painted symmetrical cell).

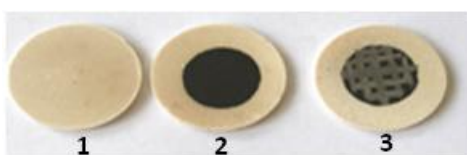


Figure 3.17: Symmetrical half cells before testing

Impedance was measured for NPCO15 (Pure and composite compositions) on CGO electrolyte in air up to 900 °C by employing basically a two point probe. Impedance spectra recorded from a symmetrical cell of $\text{Nd}_{1.85}\text{Pr}_{0.15}\text{CuO}_4$ on a CGO electrolyte are shown below:-

- a) High temperature behaviour (900 °C, 850 °C)
- b) Medium temperature behaviour (800 °C, 700 °C)
- c) Low temperature behaviour (600 °C)

In order to compare the results between pure and composite materials, they were both plotted in the same graph.

(a) Impedance spectra recorded at high temperature

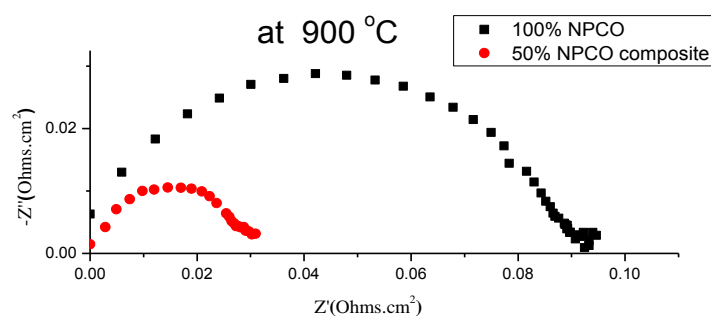


Figure 3.18: Impedance spectra recorded from a symmetrical cell of $\text{Nd}_{1.85}\text{Pr}_{0.15}\text{CuO}_4$ on a CGO electrolyte at 900 °C

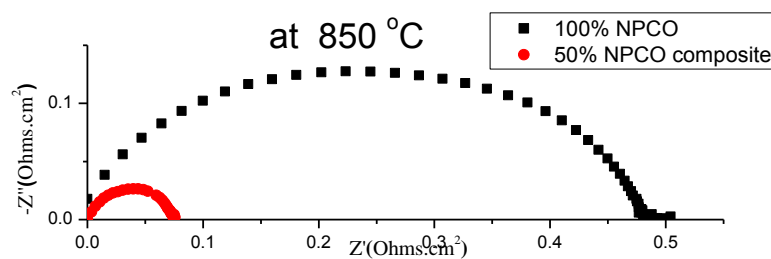


Figure 3.19: Impedance spectra recorded from a symmetrical cell of $\text{Nd}_{1.85}\text{Pr}_{0.15}\text{CuO}_4$ on a CGO electrolyte at 850 °C

b) Impedance spectra recorded at medium temperature

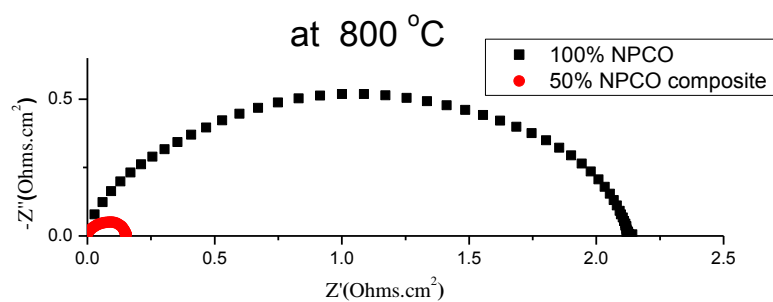


Figure 3.20: Impedance spectra recorded from a symmetrical cell of $\text{Nd}_{1.85}\text{Pr}_{0.15}\text{CuO}_4$ on a CGO electrolyte at 800 °C

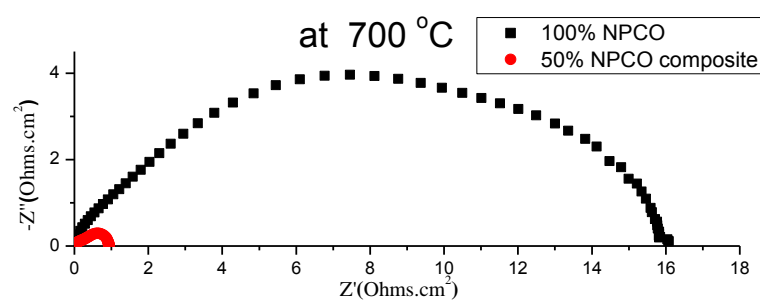


Figure 3.21: Impedance spectra recorded from a symmetrical cell of $\text{Nd}_{1.85}\text{Pr}_{0.15}\text{CuO}_4$ on a CGO electrolyte at 700 °C

c) Impedance spectra recorded at low temperature

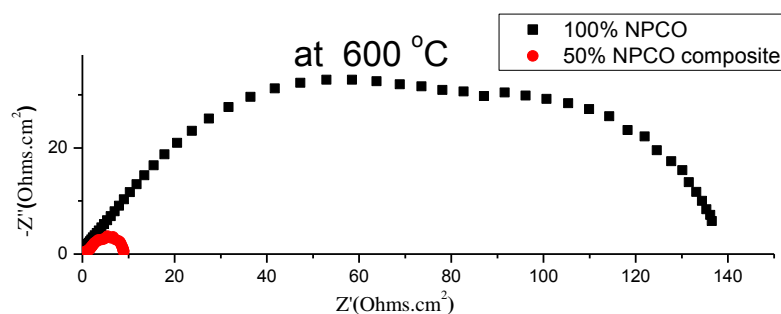


Figure 3.22: Impedance spectra recorded from a symmetrical cell of $\text{Nd}_{1.85}\text{Pr}_{0.15}\text{CuO}_4$ on a CGO electrolyte at 600°C

A typical set of impedance spectra obtained from the $\text{Nd}_{1.85}\text{Pr}_{0.15}\text{CuO}_4$ material are shown in Figure 3.18 to 3.22. In these impedance arcs, charge transfer process (chemical process) is assumed at high frequency and a mass transfer (mechanical process-Oxygen diffusion) process at lower frequency. This arc at medium to low frequencies suggests that the charge transfer process is slow (rate limiting) and therefore a charge builds up on the surface of the electrolyte. Log ASR (Area specific resistance) vs $1000/T$ for $\text{Nd}_{1.85}\text{Pr}_{0.15}\text{CuO}_4$ is demonstrating activation energy changes in the 900°C to 600°C range (Figure 3.24). Activation energy 1.89 eV and 1.67eV were obtained for NPCO15 on CGO with 100% NPCO cathode and 50% NPCO15; 50% CGO respectively.

Better performance was obtained for composite cathode material than the pure cathode material. At higher temperatures the performance of the composite cuprate was certainly good enough to be of interest as a cathode, with approximate R_p values of $0.03 \Omega\text{cm}^2$, $0.07 \Omega\text{cm}^2$ and $0.15 \Omega\text{cm}^2$ at temperatures of 900°C , 850°C and 800°C respectively. An activation energy of 1.67 eV is exhibited compared to 1 to 2 eV expected for conventional cathode materials such as LSM (129). Pure NPCO cathode material shows less performance compared to the composite with approximate R_p values of $0.09 \Omega\text{cm}^2$, $0.5 \Omega\text{cm}^2$ and $2.14 \Omega\text{cm}^2$ at temperatures at 900°C , 850°C and 800°C respectively with activation energy 1.897 eV . Lower activation energy of the 50:50 composite structure shows a significant performance benefit over the single phase material at temperatures down to 600°C .

In order to understand the microstructure of these symmetrical cells, cross sections of polished samples were prepared for the tested symmetrical cell. The microstructure of these layers shown in figure 3.25 shows a fine porous structure which appears well bonded to the electrolyte, indeed no delamination has been observed in these pellets. This is of considerable importance if this cathode is suitable for use at higher SOFC operating temperatures, where sinter activity has been seen in these materials.

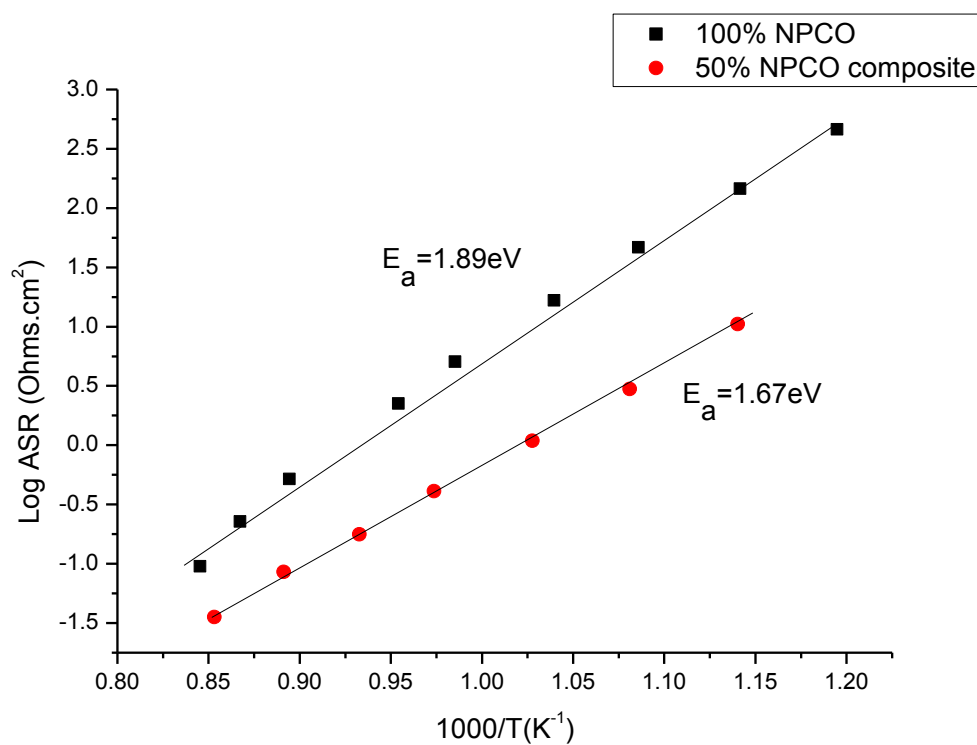


Figure 3.23: Arrhenius plot of $\text{Nd}_{1.85}\text{Pr}_{0.15}\text{CuO}_4$ on a CGO10 electrolyte with pure and composite compositions

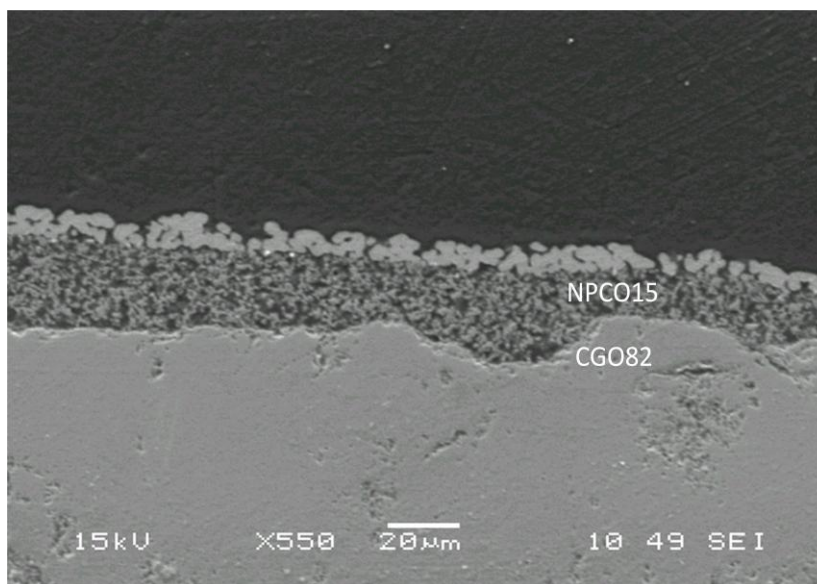


Figure 3.24: SEM image of polished cross section of tested symmetrical cell of NPCO15 on CGO electrolyte

Due to better performance on composite cathode, the next part of the work was carried out using 50% composite NPCO as a cathode material with an NPCO current collector.

3.2. 2.2 NPCO as a current collector

Impedance was measured for that composite NPCO20 (50% NPCO : 50% CGO composite) on YSZ electrolyte with CGO interlayer in air up to 900 °C by employing basically a two point probe. Basically two configurations were tested with symmetrical cell arrangements, they are pre-fired NPCO current collecting layer and the in-situ NPCO current collecting layer. Impedance spectra recorded from the symmetrical cells are shown below.

- a) High temperature (900 °C, 850 °C)
- b) Medium temperature (800 °C, 750 °C)
- c) Low temperature (700 °C, 600 °C)

In order to compare the results between pre-fired CC and in-situ CC, they both are plotted in the same graph.

a) Impedance spectra recorded at high temperature

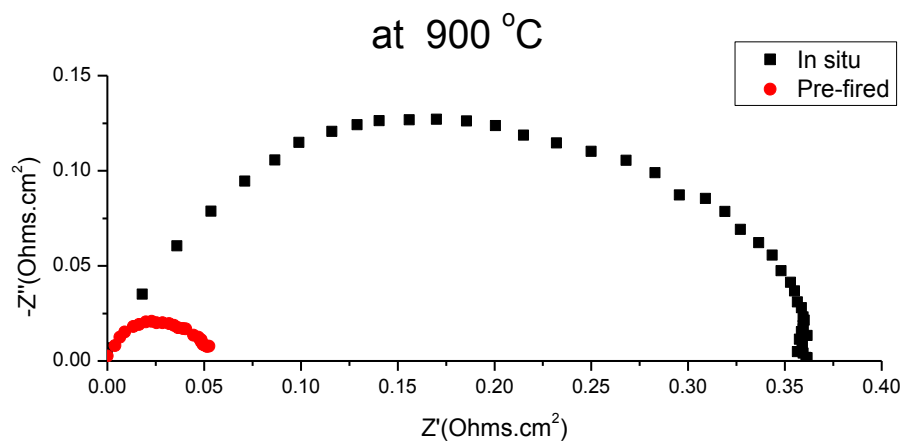


Figure 3.25: Impedance spectra recorded from a symmetrical cell of $\text{Nd}_{1.80}\text{Pr}_{0.20}\text{CuO}_4$ on a CGO electrolyte at 900 °C

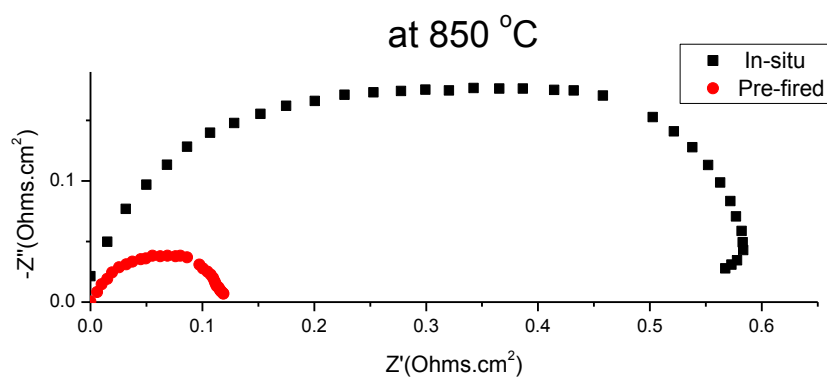


Figure 3.26: Impedance spectra recorded from a symmetrical cell of $\text{Nd}_{1.80}\text{Pr}_{0.20}\text{CuO}_4$ on a CGO electrolyte at 850 °C

b) Impedance spectra recorded at medium temperature

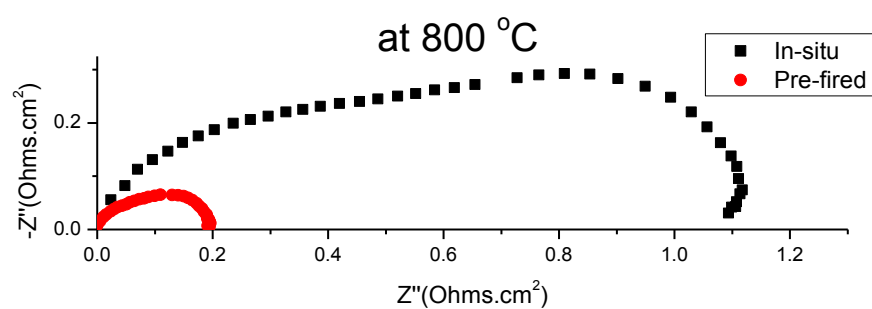


Figure 3.27: Impedance spectra recorded from a symmetrical cell of $\text{Nd}_{1.80}\text{Pr}_{0.20}\text{CuO}_4$ on a CGO electrolyte at 800 °C

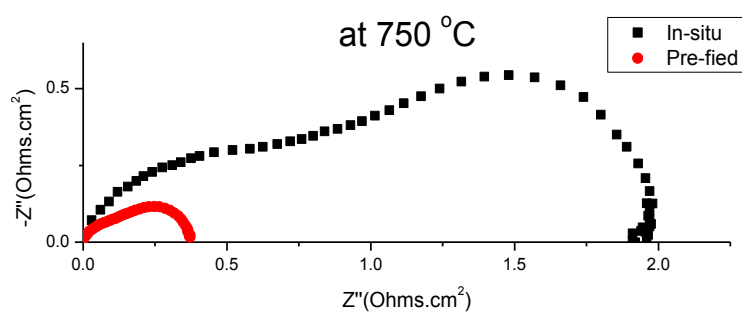


Figure 3.28: Impedance spectra recorded from a symmetrical cell of $\text{Nd}_{1.80}\text{Pr}_{0.20}\text{CuO}_4$ on a CGO electrolyte at 750 °C

c) Impedance spectra recorded at low temperature

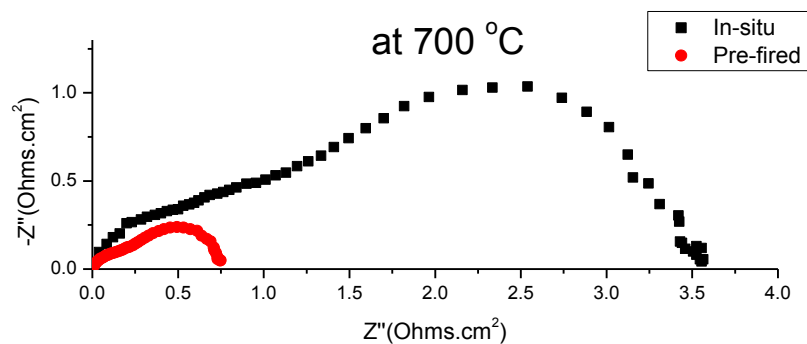


Figure 3.29: Impedance spectra recorded from a symmetrical cell of $\text{Nd}_{1.80}\text{Pr}_{0.20}\text{CuO}_4$ on a CGO electrolyte at 700 °C

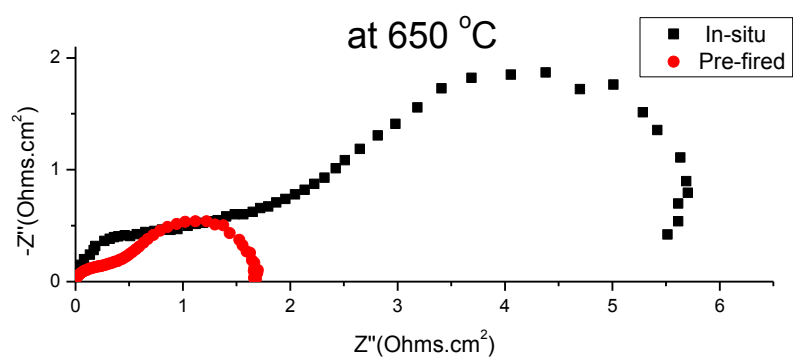


Figure 3.30: Impedance spectra recorded from a symmetrical cell of $\text{Nd}_{1.80}\text{Pr}_{0.20}\text{CuO}_4$ on a CGO electrolyte at 650 °C

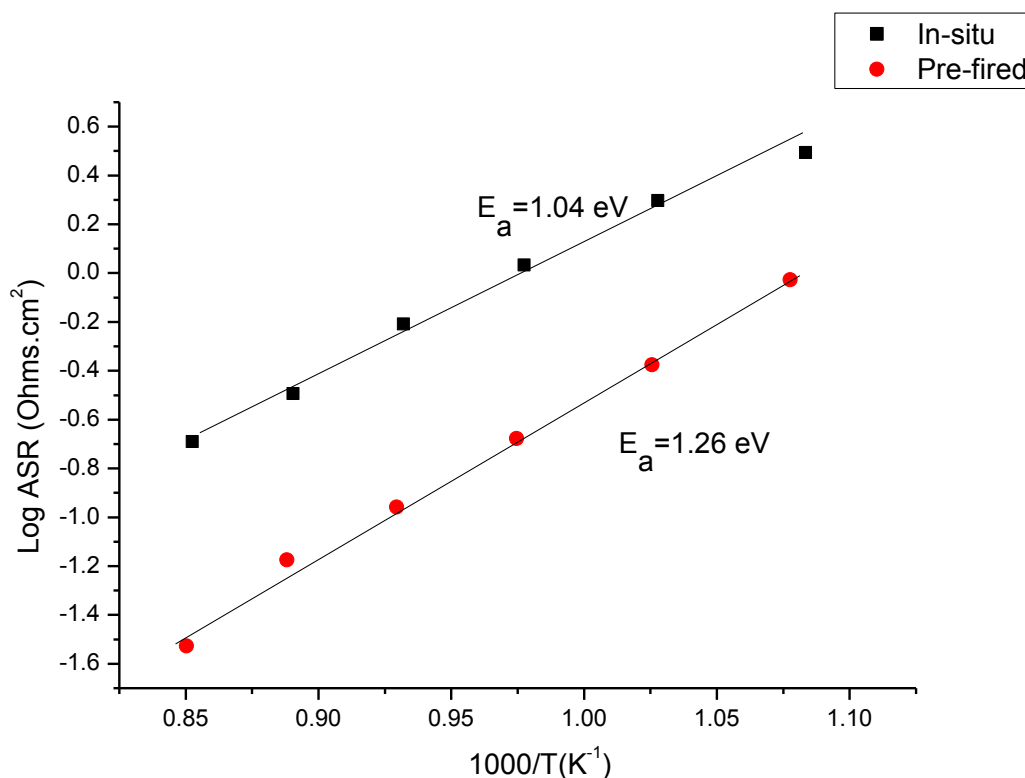


Figure 3.31: Arrhenius plot of 50% composite $\text{Nd}_{1.80}\text{Pr}_{0.20}\text{CuO}_4$ with CGO interlayer on a YSZ electrolyte with pre-fired and insitu CC layers

Differences of the pre-fired current collecting and in-situ current collecting are obvious in all the temperatures. In general, the overall spectra appear to consist of two to three rate limiting steps. From this data, three active processes have been identified in the cuprate cathode. At this time they have tentatively been ascribed to surface adsorption/diffusion, electrochemical exchange and internal transport ionic of species, with the surface adsorption and electrochemical exchange as the dominant effects at low and high temperatures respectively, however, as the temperature is reduced the impedance response appears to become more complex. As the temperature is reduced a low frequency arc becomes dominant. It is therefore likely that these processes are related to surface effects such as absorption and surface diffusion of Oxygen species. Although this arc is well defined in the lower

temperature spectra, it does not form the dominant process in the spectra measured at higher temperatures and may suggest a diffusion based process which is more prevalent at lower temperatures. At higher temperatures the response is dominated by an arc and is ascribed to electrochemical and charge transfer processes within the electrode structure. Pre-fired current collectors appear to give the most promising results, with R_p values of $0.05 \Omega\text{cm}^2$, $0.11 \Omega\text{cm}^2$ and $0.19 \Omega\text{cm}^2$ at 900°C , 850°C and 800°C respectively having been observed for cathode structures with the CGO interface layer while in-situ current collector give R_p values of $0.36 \Omega\text{cm}^2$, $0.56 \Omega\text{cm}^2$ and $1.09 \Omega\text{cm}^2$ at 900°C , 850°C and 800°C respectively. Pre-fired samples are good enough for mid temperature SOFC operation in the range of 850°C to 800°C . Therefore this performance observed for the pre-fired structures suggests possible applications in the temperature range of $850\text{-}800^\circ\text{C}$ and may give a method for the incorporation of current collection and cell to interconnect contact in a single layer. Pre-fired structure would offer a better environment to prevent the built up of this strain over the area of the electrode. This may be advantageous for stack assembly and reduced degradation, and so provide a reliable and consistent cathode contact to the interconnect.

After being tested with impedance, the samples were analysed with the SEM to see if there was any post delamination or not. There was no any indication of a weak bond between the cathode and the electrolyte and post test delamination (figure 3.32).

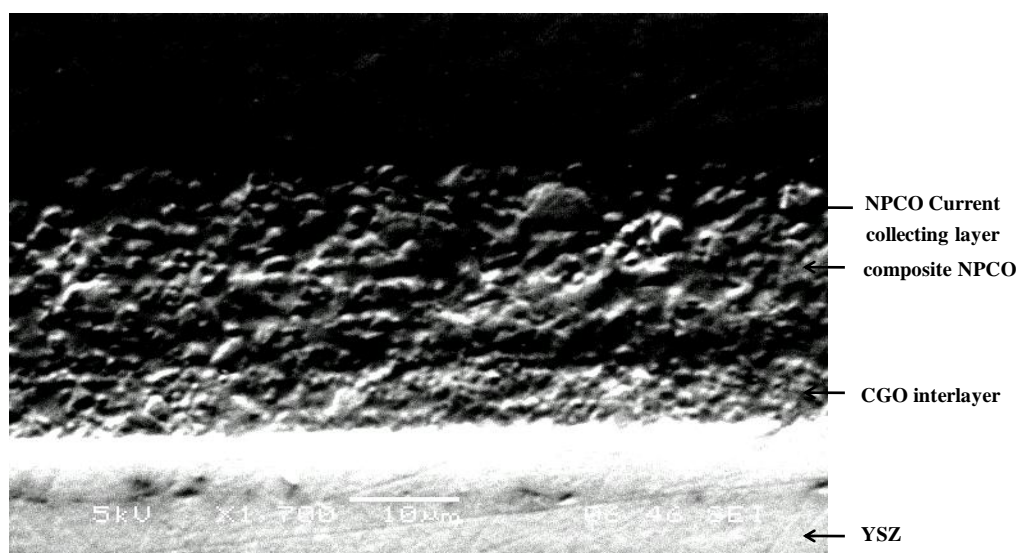


Figure 3.32: SEM image of polished cross section of tested symmetrical cell with in-situ current collecting layer

3.3 Conclusions

The main aim of this work was to explore the basic high temperature electrical characteristics of $\text{Nd}_{2-x}\text{Pr}_x\text{CuO}_{4+\delta}$ and how this matches with those required for components in an SOFC stack or system. From this, it was hoped to determine any possible applications for the NPCO system in SOFC applications. NPCO was characterised over a range of dopant levels ($x=0.15 - 0.25$) and a maximum conductivity (86.7 Scm^{-1}) in the region of $x = 0.25$ was identified due to the solubility limit of praseodymium in the neodymium cuprate matrix and suggests that this provides the optimum conditions for transport of ionic and electronic species within the material. NPCO has shown the highest conductivity with over 80 Scm^{-1} being observed from structures formed at temperatures normally associated with stack sealing and conditioning cycles. This offers the possibility of robust, high conductivity contacts leading to improved stack performance through better current distribution and reduced ohmic losses. NPCO shows n-type semiconductor behaviour which is of great promise for cathode side application which gives operational advantages when operating at mild oxygen

deficiency (e.g high Oxygen utilization) or high cell polarisation where the local cathode oxygen partial pressure is reduced.

At slightly reduced $p(\text{O}_2)$ the conductivity rises as one would expect with an n-type semi-conduction mechanism. However as $p(\text{O}_2)$ continues to drop, the conductivity drops dramatically and in representative anode side conditions the measured conductivities have been below 10^{-1} Scm^{-1} which are far too low for anode current collection and distribution applications. NPCO is not stable under Hydrogen reducing atmospheres therefore the potential for an anode side application is little more problematic.

AC impedance studies have been carried out on symmetrical cells to investigate the performance of NPCO as a cathode material. The study mainly focused on polarization resistance and the activation energies of the cells. Low R_p values and low activation energies are obtained for a composite cathode compared to pure cathode material. These low R_p values and low activation energies of composite NPCO make it a possible candidate for cathode material in SOFC and also its cathode performance is comparable with existing cathode material and worth further investigation.

Comparing the performance on Pt and NPCO as a current collecting material, low R_p values were obtained for Pt ($0.03 \text{ } \Omega\text{cm}^2$ and $0.05 \text{ } \Omega\text{cm}^2$ R_p values were obtained for Pt and NPCO respectively) but NPCO still exhibited lowest activation energies which indicate good catalytic activity (1.67 eV and 1.04 eV activation energies were obtained for Pt and NPCO respectively).

NPCO pre-fired exhibited better performance than in-situ fired NPCO. Both in-situ and pre-fired current collecting NPCO still exhibited lowest activation energies and it suggests good catalytic activity. The presence of co-existing $\text{Pr}^{4+}/\text{Pr}^{3+}$ in cuprate structures gives better

performance. It seems that NPCO material exhibit lower activation energies and it may also hint at a beneficial influence of the dual oxidation states of the Pr cation on the electrochemical reactions. From this study it is clear that NPCO shows great promise for the role of pre-fired cathode contact and current collector. Therefore NPCO pre-fired layer can be engineered to allow some degree of compliance during stack build. Finally from all these studies it is evident that the praseodymium doped neodymium cuprate material shows considerable promise as a potential cathode material for solid oxide fuel cell application. .

Chapter 4-- Material characterisation, Structural transitions and phase relationship in La Doped $\text{Nd}_{2-x}\text{Pr}_x\text{CuO}_4$

4.0 Introduction

In this work, two different crystal structure types were considered, the tetragonal form T' , and the tetragonal and orthorhombically distorted K_2NiF_4 -type structure T/O. The parent compounds of these structures were Nd_2CuO_4 for the T' and La_2CuO_4 for the T/O. To investigate the phase transformations between these two structures La was doped into a $\text{Nd}_{1.8}\text{Pr}_{0.2}\text{CuO}_4$ to obtain the general family of $\text{Nd}_{1.8-x}\text{La}_x\text{Pr}_{0.2}\text{CuO}_4$.

4.1 Methods used

Nineteen samples with different compositions were examined to construct the phase diagram of $\text{Nd}_{1.8-x}\text{La}_x\text{Pr}_{0.2}\text{CuO}_4$ family. Materials have been produced, with varying La content over the range $x=0$ to $x=1.8$ with an increment of 0.1, by the solid state method. Hygroscopic powders (Nd_2O_3 , Pr_6O_{11} , La_2O_3) were dried for 30 minutes at temperature up to 900°C . Stoichiometric amounts of Nd_2O_3 (Alfa-Aesar 99.9%), Pr_6O_{11} (Alfa-Aesar 99.9%), CuO (Aldrich 99+ %) and La_2O_3 (Aldrich 99.99%) were then weighed and ground in acetone. These mixtures were then dried and calcined in air at 850°C for 36 hours. Following this, powders were reground using a planetary ball mill and the heat treatment (850°C for 36 hours) repeated. It was found 850°C fired samples (where the $x=0.3$ to 1.6), is a mixture of two phases, therefore all the samples were reheated 950°C for 24 hours to synthesis NLPCO. 3°C min^{-1} rate was used for both heating and cooling.

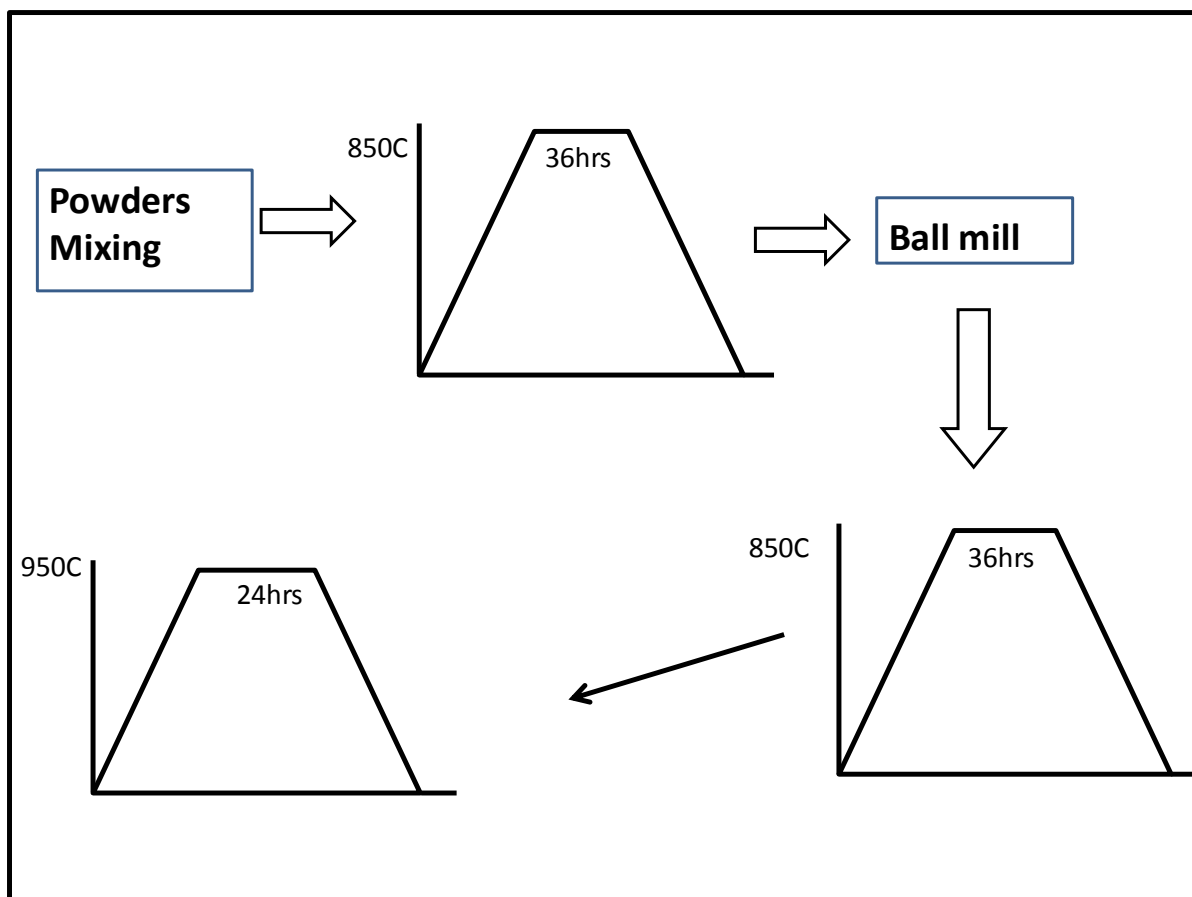


Figure 4.1: Schematic diagram of the solid state reaction

Phase purity was examined by X-ray diffraction (XRD) analysis of powders on a Stoe STADI/P powder diffractometer. Incident radiation was generated using a $\text{CuK}\alpha_1$ source ($\text{CuK}\alpha_1 = 1.54056 \text{ \AA}$). The step size for data collection was 0.02° with a collection time of 10 s at each step. Vaseline was used to mount the sample in the holder.

In-situ X-ray diffraction analysis of powders were collected at room temperature on a Bruker Axis D8 advance diffractometer equipped with a Lynxeye detector in the $10\text{--}90^\circ$ range with a step of 0.02° and accounting time of 25 s per step ($\text{CuK}\alpha = 1.54 \text{ \AA}$). The high temperature diffraction data were collected in the $10\text{--}90^\circ$ range, with a step of 0.0148° and a counting time of 0.2 s per step, on a Bruker axis D8 advance diffractometer equipped with a high

temperature Anton Paar HTK 1200N chamber and a one dimensional X-ray detector VÅNTEC-1 ($\text{CuK}\alpha=1.54 \text{ \AA}$). X-ray data was recorded every 50°C increment up to 1000°C for all over these compositions, but interesting temperatures for each compositions (T' , T'' , T/O) was selected and plotted in the graphs. All these graphs were plotted upon cooling from 1000°C to room temperature. Equilibration time at each temperature was 1 hour.

FULLPROF software (123) was used to perform least squares refinement of the room temperature lattice parameters of the samples.

The oxygen content of all the single phase samples was determined by thermogravimetric analysis using a TGA (NETZSCH/ TG209). About 20 mg of powder was heated at $5^\circ\text{C}/\text{min}$ under flowing 5%hydrogen/95%argon ($22\text{ml}/\text{min}$.) from 50°C to 950°C . The content of oxygen was calculated by considering the detected mass losses.

Magnetic properties were only measured for selected compositions of single phase materials. A MPMS superconducting quantum interference device was used to determine the magnetization measurements from 200K to 5K.

Electrical properties were measured using small circular pellets. Powders were uniaxially pressed using a pressure of 120 Mpa. The pellets had a diameter of 13 mm with a thickness of 1-2 mm and were fired in air for 10 hours at 950°C . Conductivity was measured using a four point DC technique with measurements obtained in air between room temperature and 900°C . Effects of Oxygen partial pressure were also studied at 900°C by introducing nitrogen or dry argon, either of which was flushed through the system until a stable $p(\text{O}_2)$ was measured

by an YSZ oxygen sensor. Once this was reached the system was sealed and the conductivity monitored as the $p(\text{O}_2)$ slowly increased as oxygen found its way back into the system by natural leakage. Electrical behaviour was studied in some compositions where the La level was $x = 0.0, 0.1, 0.2, 0.3, 1.7$ and 1.8 .

4.2 Results and Discussions

4.2.1 Phase characterization

Room temperature as well as high temperature X-ray diffraction (up to 1000°C) data were collected.

4.2.1.1 Room temperature X-ray analysis

From analysis of the XRD patterns obtained at room temperature there are clearly five distinguishable regions for the 950°C fired $\text{Nd}_{1.8-x}\text{La}_x\text{Pr}_{0.2}\text{CuO}_4$ system (Figure 4.2). They are, (1) monophasic T' solid-solution for $0.0 \leq x < 0.8$; (2) two phase mixture $T' + T''$ for $0.8 \leq x < 1.4$; (3) monophasic T'' solid-solution for $1.4 < x < 1.5$; (4) two phase mixture $T'' + \text{O}$ for $1.5 \leq x < 1.6$; and (5) monophasic O-phase solid-solution for $1.6 \leq x \leq 1.8$. Interestingly, a new tetragonal symmetry phase, T'' , was found similar to the well-known T' type structure which has slightly larger a and c axes. XRD patterns of monophasic systems (T' , T'' and O) at room temperature are shown in figure 4.3.

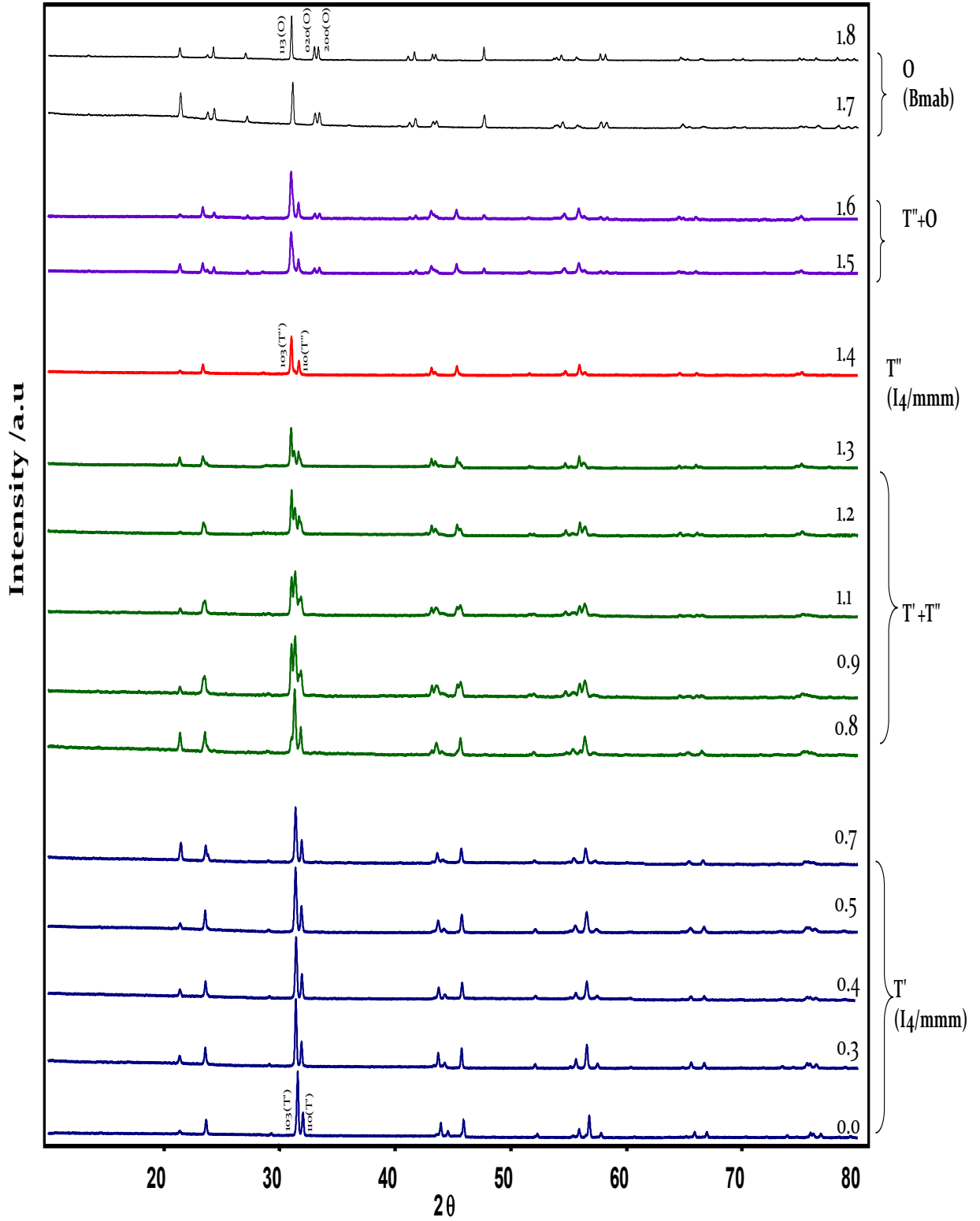


Figure 4.2: Room temperature XRD patterns for the $\text{Nd}_{1.8-x}\text{La}_x\text{Pr}_{0.2}\text{CuO}_4$ where the x is between 0-1.8 with an increment of 0.1

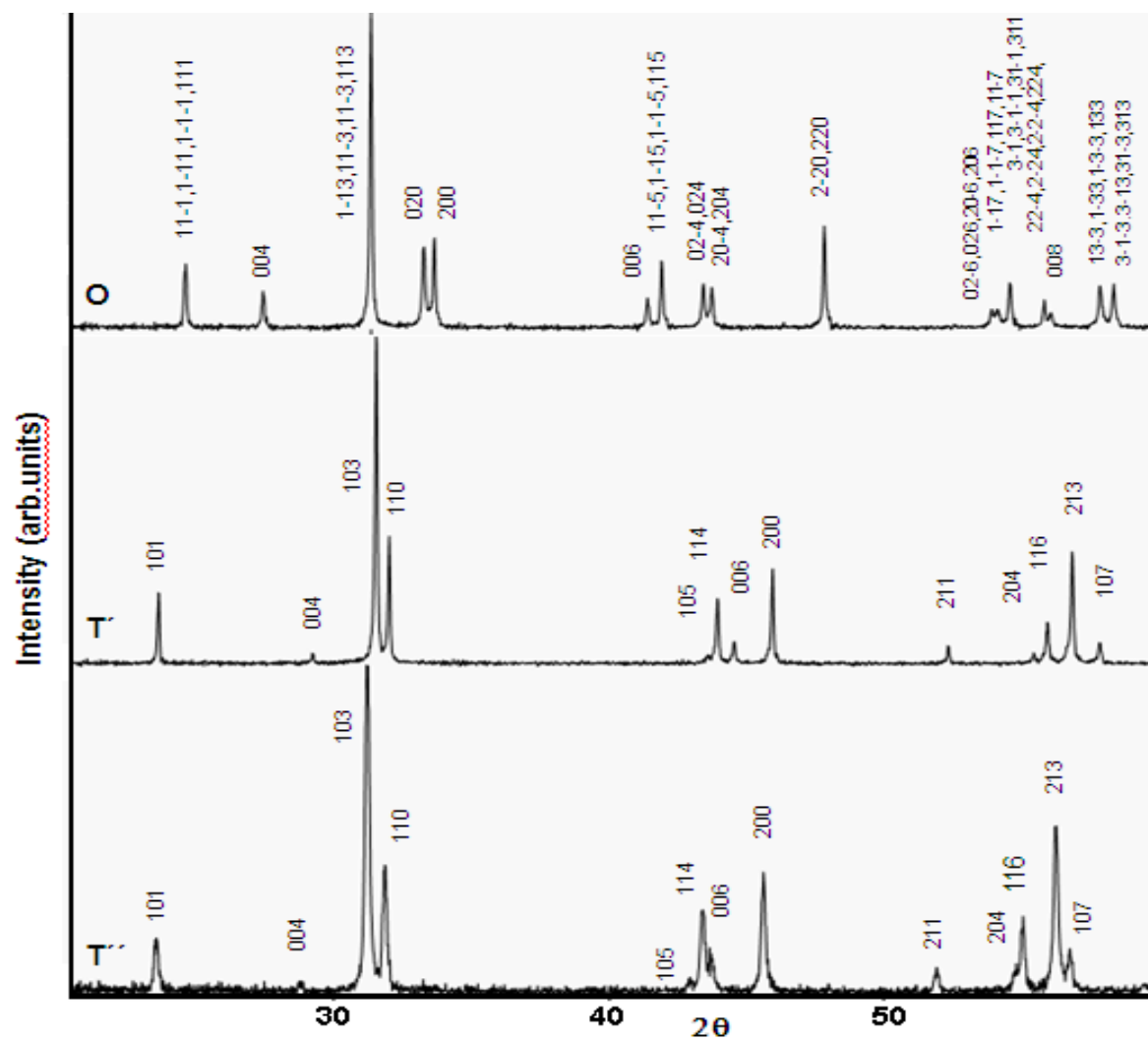


Figure 4.3: XRD pattern for the Single phase compositions at room temperature for T' phase (x=0.1) T'' phase (x=1.45) and O phase (x=1.7) for $\text{Nd}_{1.8-x}\text{La}_x\text{Pr}_{0.2}\text{CuO}_4$

Table 4.1: Refined structural parameters for $\text{Nd}_{1.8-x}\text{La}_x\text{Pr}_{0.2}\text{CuO}_4$ where $x = 0.0, 0.1, 0.2, 0.3, 0.4, 0.5, 0.7, 1.45, 1.7$ and 1.8 at RT (295K)

x	Phase	Space group	a (Å)	b(Å)	c (Å)	c/a	V(Å ³)
0.0	T'	I4/mmm	3.9523(2)	-	12.1963(9)	3.08528	190.51(2)
0.1	T'	I4/mmm	3.9570(4)	-	12.1967(1)	3.08588	189.92(4)
0.2	T'	I4/mmm	3.9600(1)	-	12.2201(5)	3.08832	190.34(1)
0.3	T'	I4/mmm	3.9616(3)	-	12.257(1)	3.09393	192.37(3)
0.4	T'	I4/mmm	3.9627(3)	-	12.2681(9)	3.09588	192.65(2)
0.5	T'	I4/mmm	3.9643(1)	-	12.2803(5)	3.09766	193.00(1)
0.7	T'	I4/mmm	3.9721(4)	-	12.322(1)	3.10228	194.43(3)
1.45	T''	I4/mmm	4.0065(1)	-	12.5255(5)	3.12629	201.05(1)
1.7	O	Bmab	3.7963(1)	3.8360(1)	13.1586(2)	3.44810	191.62(1)
1.8	O	Bmab	3.7963(1)	3.8341(1)	13.1658(2)	3.45085	191.64(1)

The room temperature Rietveld refinement profile for T', T' + T'' with the space group I4/mmm was shown in figure 4, 5

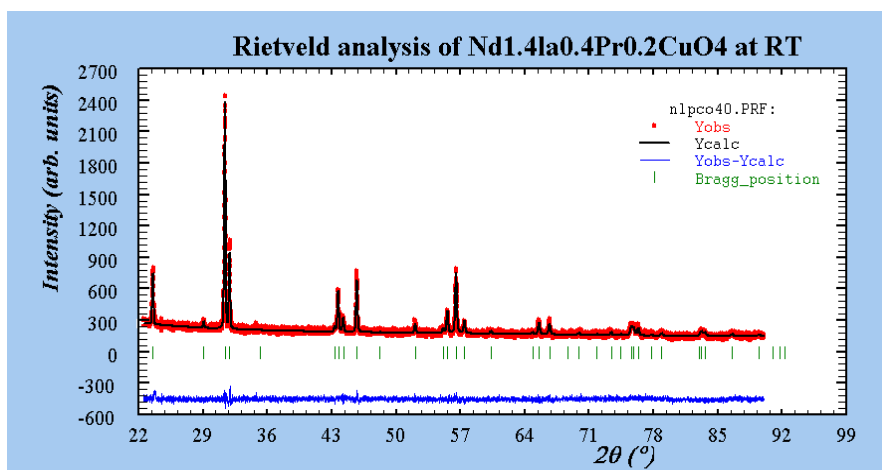


Figure 4.4: Rietveld refinement profile of T' phase ($\text{Nd}_{1.4}\text{La}_{0.4}\text{Pr}_{0.2}\text{CuO}_4$) at room temperature (295K) in the I4/mmm space group. Observed (plus sign), calculated (continuous line) and Bragg reflections (vertical lines) are shown. Chemical cell: s.g. I4/mmm, $a = b = 3.9627(3) \text{ \AA}$, $c = 12.2681(9) \text{ \AA}$, $v = 192.65(2) \text{ \AA}^3$, $R_p: 5.49$, $R_{wp}: 7.01$, $R_{exp}: 7.04$, $\chi^2: 0.992$, $R_B: 8.89$

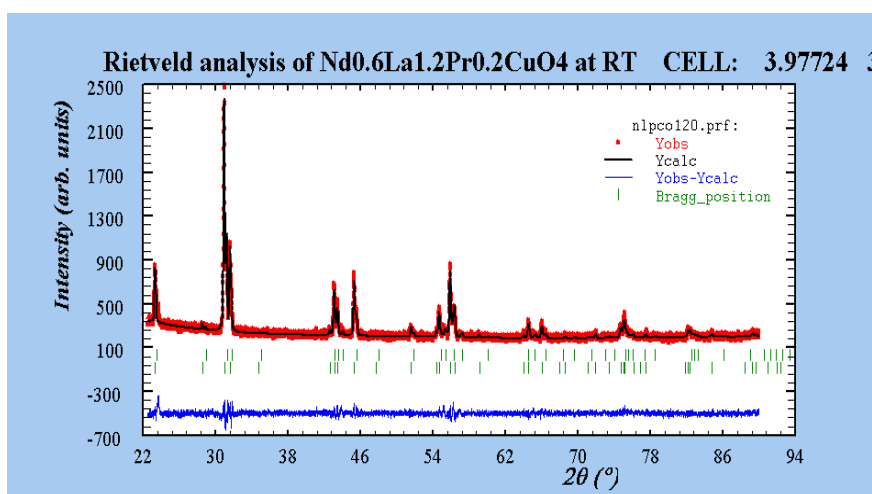


Figure 4.5: Rietveld refinement profile for the two phase region (T' + T'') at room temperature (295K) in the I4/mmm space group. Observed (plus sign), calculated (continuous line) and Bragg reflections (vertical lines) are shown. Chemical cell for T': s.g. I4/mmm, $a = b = 3.9772 \text{ \AA}$ (2), $c = 12.316 \text{ \AA}$ (1), $v = 194.82(2) \text{ \AA}^3$, Chemical cell for T'': s.g. I4/mmm, $a = a = 3.9965 \text{ \AA}$ (2), $c = 12.4888 \text{ \AA}$ (6), $V = 199.47(2) \text{ \AA}^3$, $R_p: 5.44$, $R_{wp}: 7.02$, $R_{exp}: 6.43$, $\chi^2: 1.19$, $R_B: 7.20$ (phase1) 7.35 (phase2)

In order to understand the cell parameter change along the series x vs a, c and c/a were plotted in figure 4. 6.

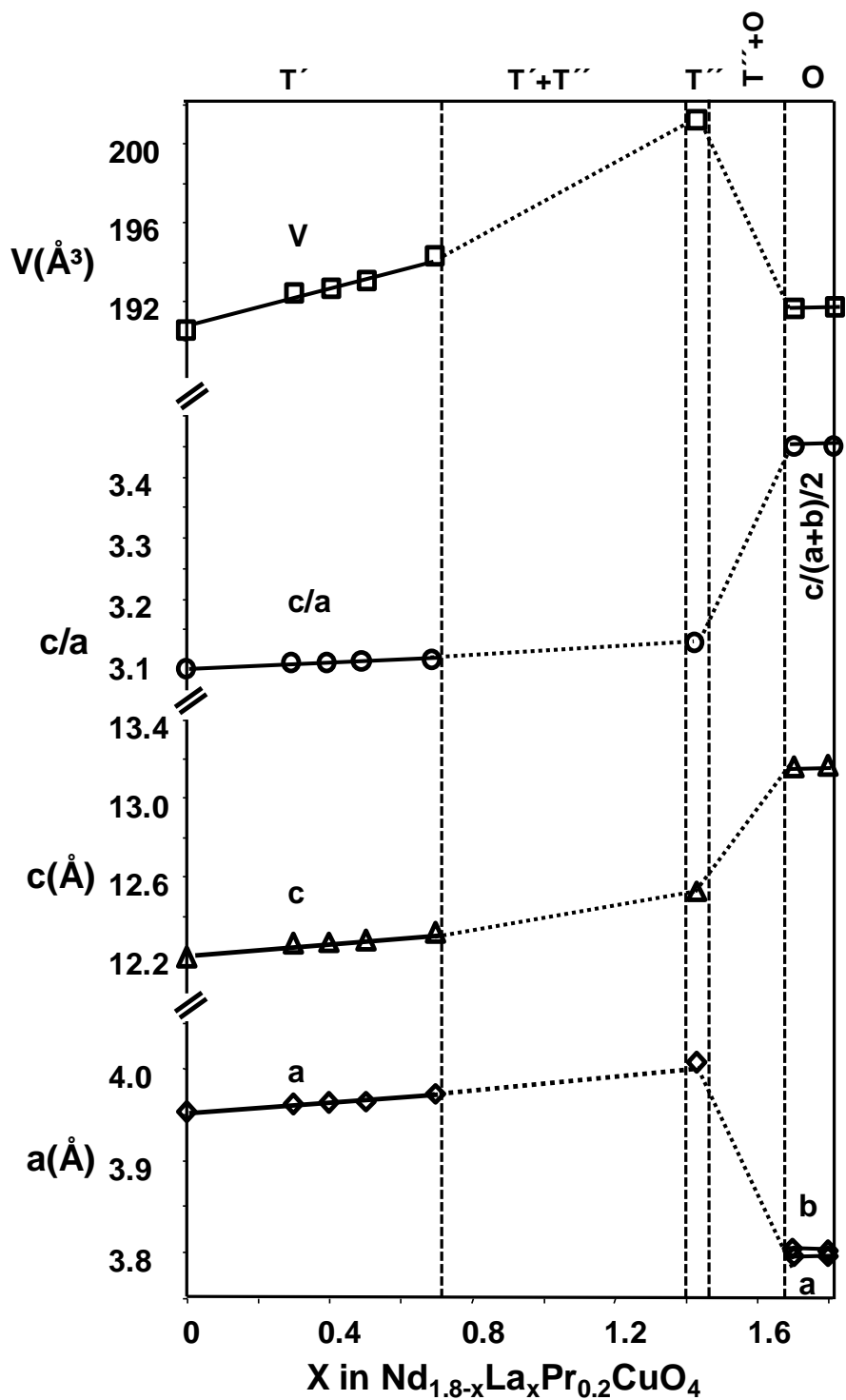


Figure 4.6: Lattice parameters (a , c and c/a) and volume (V) vs. La content for the single phase regions (T , T'' and O) of $\text{Nd}_{1.8-x}\text{La}_x\text{Pr}_{0.2}\text{CuO}_4$ measured at room temperature

Both lattice constants a and c increased with increasing x following Vegard's law from $x=0$ till $x<0.8$. Discontinuities of the cell parameters are obtained where $0.8 \leq x \leq 1.4$ and $1.5 \leq x \leq 1.6$ due to the compositional phase separation. The T' has a much smaller c axis and c/a ratio and a larger a axis and cell volume compared to T (O) structure. The narrow single phase, T'' phase, around $1.4 < x < 1.5$ has larger a and c axis and c/a ratio compared to T' . Figure 4.3 shows the similarity of these tetragonal phases in X-ray analysis obtained for La levels of 0.1 and 1.45. However, the lattice constants of both a and c are clearly distinct between the two tetragonal phases. Remarkably T'' has a much larger cell volume than either T' or T/O phases.

Figure 4.7 shows the graph obtained with increase La content (x) against the intensity ratio $I_{T'} / (I_{T'} + I_{T''})$. It indicated that intensities of the T' ($I_{T'}$) decreases with La doping which leads to zero intensity between La content of 1.4 to 1.5 content (~ 1.45). That mean when the La level reaches to around 1.45 in this compound ($\text{Nd}_{0.35}\text{La}_{1.45}\text{Pr}_{0.2}\text{CuO}_4$) the phase will be a pure T'' phase.

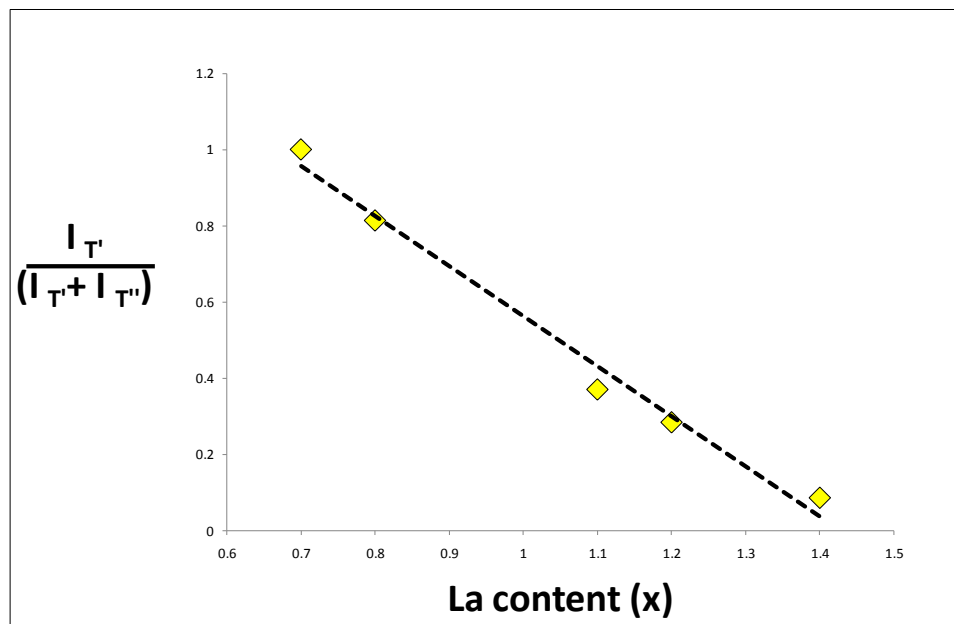


Figure 4.7: La content (x) vs $I_{T'} / (I_{T'} + I_{T''})$ for the $\text{Nd}_{1.8-x}\text{La}_x\text{Pr}_{0.2}\text{CuO}_4$ system

4.2.1.2. In situ X-ray analysis

In order to understand the phase development involving these three tetragonal modifications (T' , T , T'') in-situ high temperature XRD analysis was performed on cooling with temperatures where monophasic systems were found.

Figures 4.8, 4.9, 4.14 show the results from in-situ XRD studies for T' ($x=0.1$), T'' ($x=1.45$) and O ($x=1.7$) respectively for the $\text{Nd}_{1.8-x}\text{La}_x\text{Pr}_{0.2}\text{CuO}_4$ system.

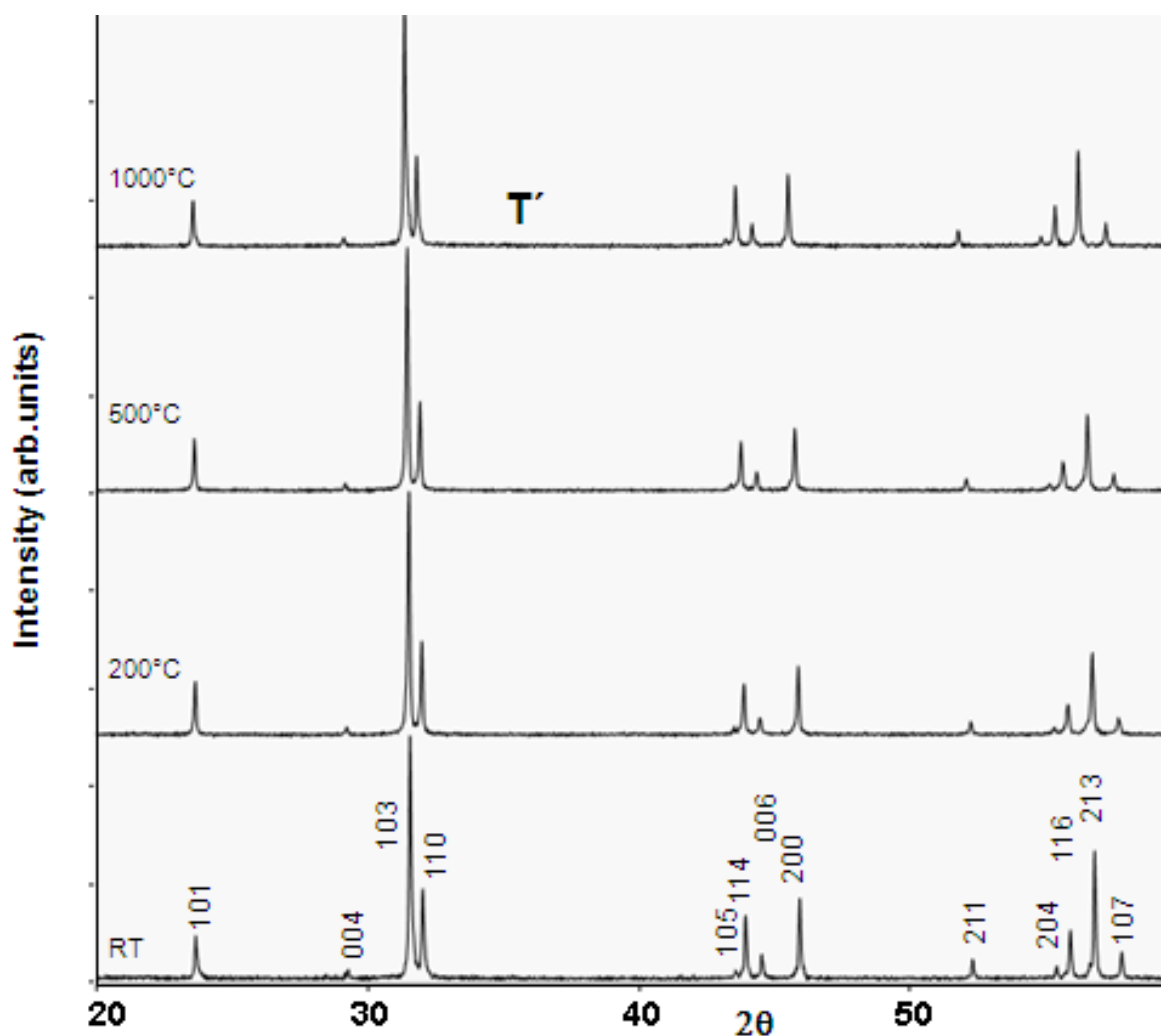


Figure 4.8: In-situ XRD pattern for T' phase at different temperature for the $x=0.1$ composition

Due to the strictly square planar Cu coordination in T', this phase is very robust and does not show buckling of the CuO₂ planes down to the lowest temperature (130). This phase can tolerate wide range of lanthanides, from Pr to Gd. High temperature X-ray analysis (Fig 4.8) indicates that T' phase is stable up to 1000 °C without any compositional separation or phase transition for compositions $0.0 \leq x < 0.8$. Replacement of a greater amount of the smaller Nd³⁺ by larger La³⁺ increases the bond length mismatch for the T' phase, which will lead to changes in c axis oxygen transforming the fluorite layer to a rock salt layer.

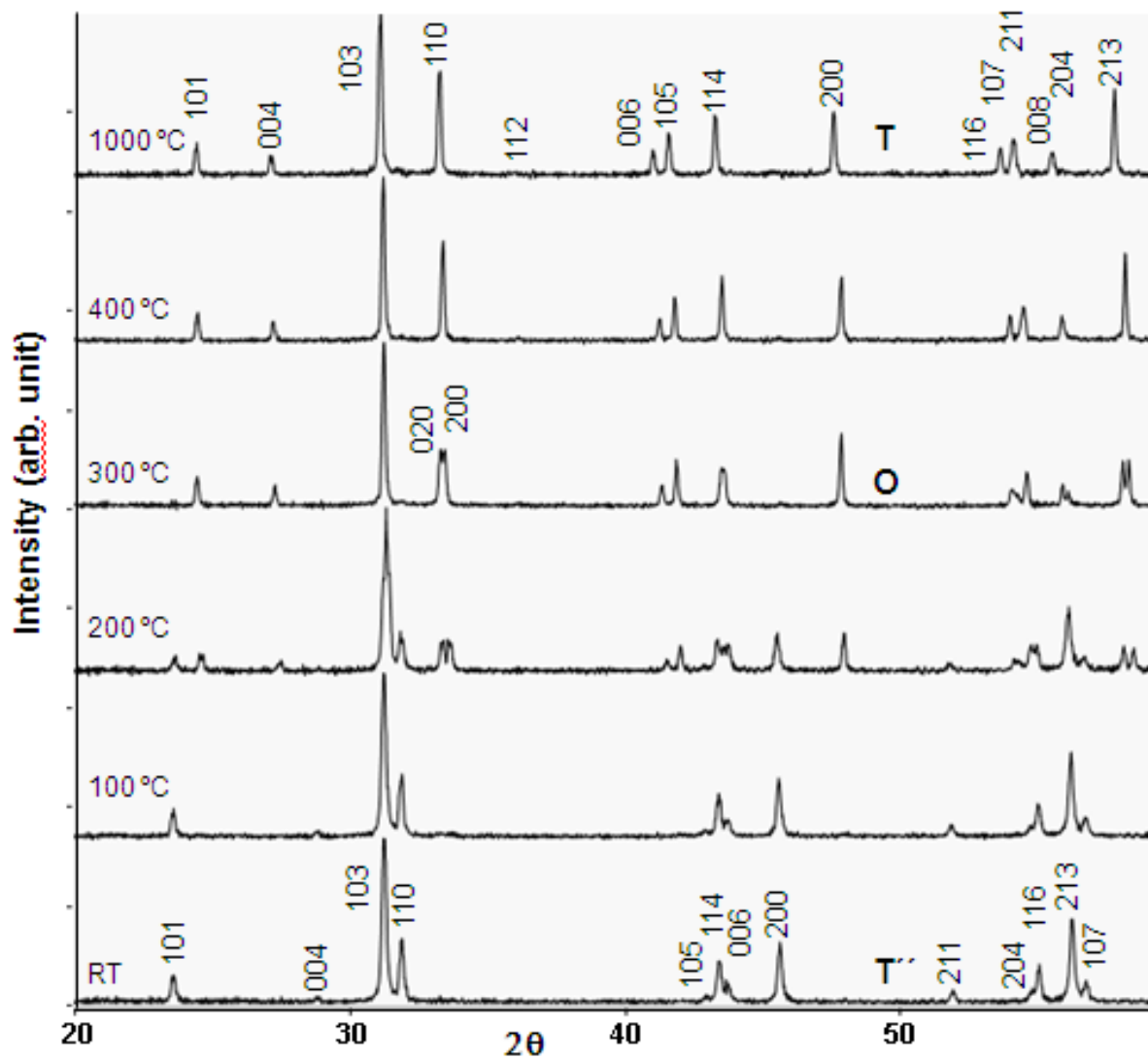


Figure 4.9: In-situ XRD pattern for T'' phase at different temperatures for the $x=1.45$ composition

In the $1.4 < x < 1.5$ compositional range, the high temperature tetragonal T (I4/mmm) phase was found at the highest temperatures. This undergoes orthorhombic distortion between 400 and 300°C and converts to the T'' phase at lower temperatures. At 200 °C there is still a mixture of T'' and O as the transformation has not completed with the time of the experiment. By 100 °C, however the sample is entering T''. The T'' phase does not exist at high temperature; it forms upon cooling at lower temperatures which make sintered pellets become very fine powders when cooled to room temperature. Interestingly, this phenomenon only occurred when the pellets were sintered above 900 °C.

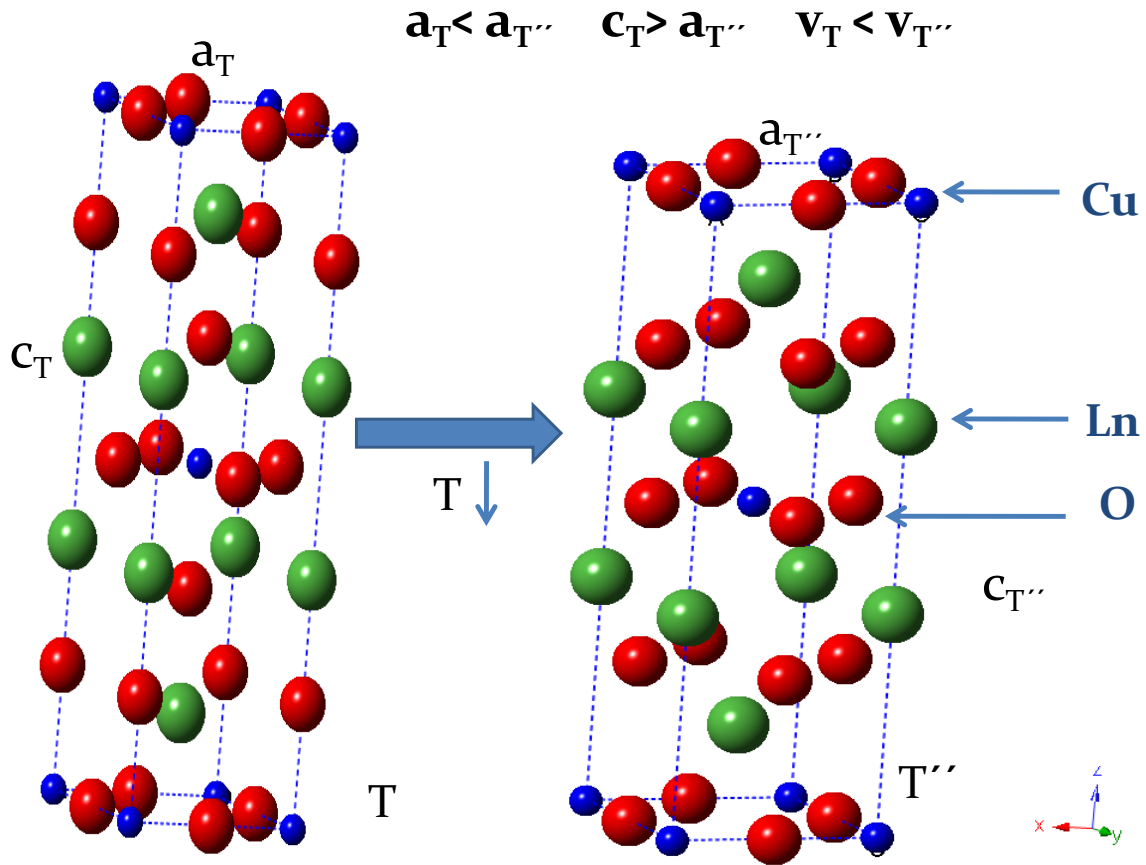


Figure 4.10: Schematic diagram for T to T'' transition for the $x=1.45$ composition

Different calcination temperatures (850 °C and 950 °C) have been investigated and both slow cooling and quenching have been employed. Samples in the range $0.2 < x < 1.4$ which have been annealed below 950°C formed $T' + T/O$ phases (Figure 4. 11).

After annealing at lower temperature (e.g. 850 °C) the T'' phase does not appear on cooling as the T phases undergoes a spinodal decomposition into higher and lower Nd content T' and T/O phases. Therefore the T'' phase only forms with a moderately fast cooling rate. The high temperature T phase undergoes a diffusionless transition to the metastable T'' phase. Therefore on annealing any rapidly cooled sample at lower temperature, equilibrium spinodal product phases (T' and T/O) will be formed (figure 4.11). Samples in the range of $0.2 > x > 1.4$ which have been fired below 950 °C formed $T' + T/O$ equilibrium phases. Higher calcinations temperatures (950 °C) prevents the onset of the orthorhombic phase at $x=0.2$. However a further lattice distortion was observed beginning at $x=0.8$; this is a T'' phase and exists in a mixture with the T' phase until $x=1.4$. The T'' phase only exists as a single phase over a narrow band between $1.4 < x < 1.5$ before the emergence of the orthorhombic distorted phase which becomes a single phase at $x=1.6$. The T'' phase was observed both in quenched and slow cooled specimens for the 950°C fired samples. Two different ramp rates ($3\text{ }^{\circ}\text{C min}^{-1}$ and $2\text{ }^{\circ}\text{C min}^{-1}$) were used for the slow cooling specimens. But these ramp rates are not slow enough to form equilibrium spinoidal products. That means this slow cooling processes are relatively fast. But on annealing samples at lower temperature (e.g. 850 °C, 600 °C) for a long time (24 hours), equilibrium spinodal product phases (T' and T/O) will be formed. Therefore the T'' phase forms with relatively fast cooling rate, which does not allow the necessary diffusion of ions and the compositional adjustment required for the low temperature equilibrium phases (T' and T/O) to form. Figure 4.11 shows the 850 °C annealed samples for the $\text{Nd}_{1.8-x}\text{La}_x\text{Pr}_{0.2}\text{CuO}_4$ the range $x=0$ to $x=1.8$ with an increment of 0.1. It shows there is no any metastable T'' present for the low temperate annealed

compositions. T'' phase was preserved at operational temperatures and more detail will be discussed in chapter 5.

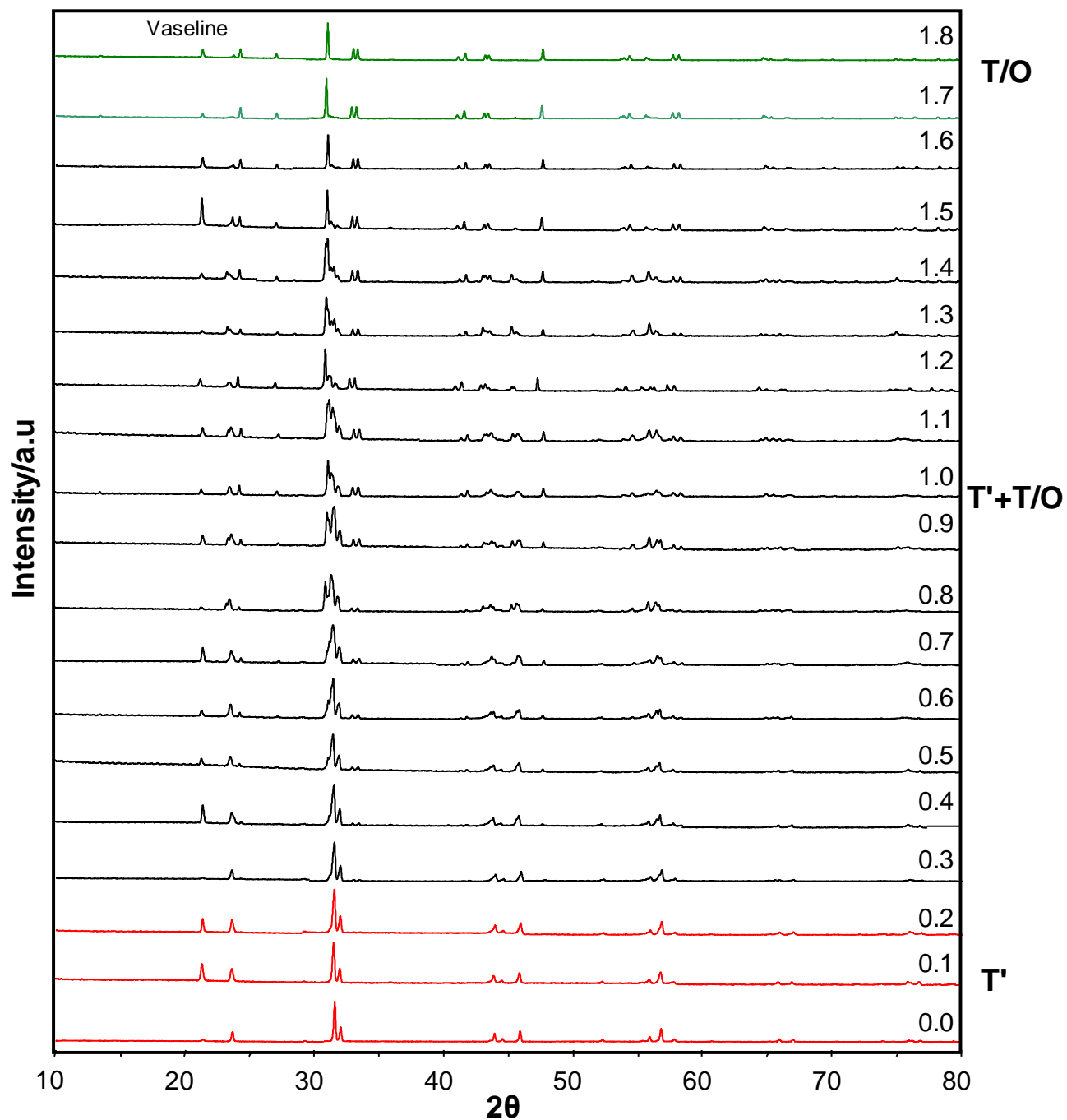


Figure 4.11: Room temperature XRD pattern for the 850 °C annealed samples for the $\text{Nd}_{1.8-x}\text{La}_x\text{Pr}_{0.2}\text{CuO}_4$ where the $x=0$ to $x=1.8$ with an increment of 0.1

It has been suggested by Manthiram and Goodenough (76) that in the biphasic system (T' + T'') that higher temperatures, disordering the cation and /or the O^{2-} ions within Ln-O layers, stabilises a single phase material via large entropy term in the free energy. Then upon cooling to lower temperatures, ionic ordering within Ln-O layers can occur at room temperature, resulting in a spinoidal decomposition to the biphasic mixture T' and T'' . But our results indicate that two phase region ($T' + T''$) does not stabilise as a single phase even at elevated temperatures (1000 °C). Even at 1000 °C these compositions ($0.8 \leq x \leq 1.4$) formed T' and T . For an example composition at $x=1.2$ ($Nd_{1.8-x}La_xPr_{0.2}CuO_4$) at room temperature it exist as T' and T'' but when the temperature is gradually increased the T'' phase transforms to T while the T' phase stays stable as described in figure 4.12. Figure 4.13 further explains this phase behaviour, as can be seen at 1000°C; at $x= 1.2$ composition is a combination of T' and T . Therefore two phase region ($0.8 \leq x \leq 1.4$) at higher temperatures, forms T' and T , and it wouldn't stabilises any single phase at any point. The T phase distorts to O with upon cooling while T' remains stable with temperature. Even though T' and T'' have similar XRD patterns at room temperature the phases are discrete in compositional space, and the T'' phase seems to be kinetically stabilised.

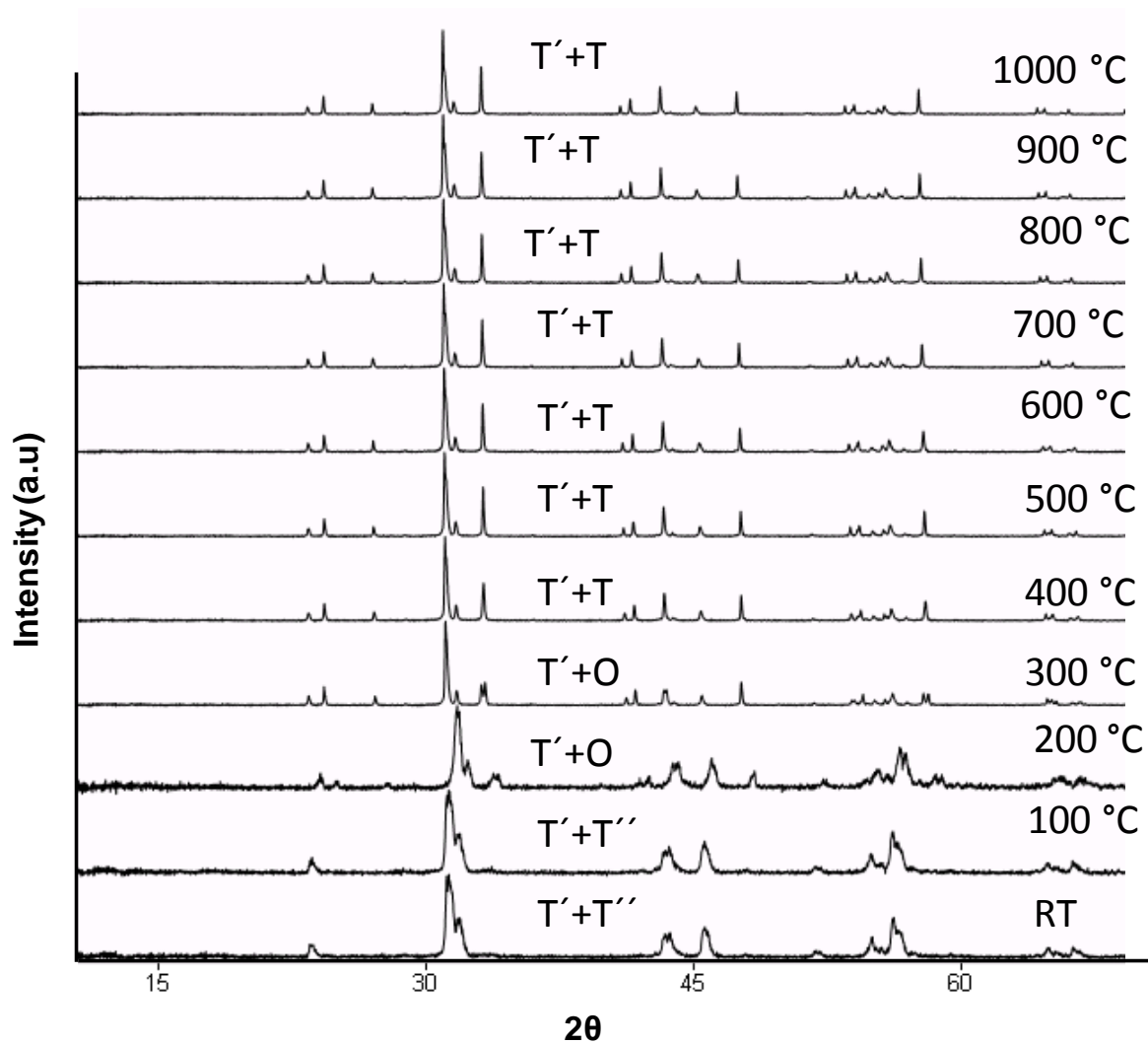


Figure 4.12: In-situ XRD pattern for the two phase region where $x=1.2$ ($T' + T''$ at room temperature composition) at different temperatures

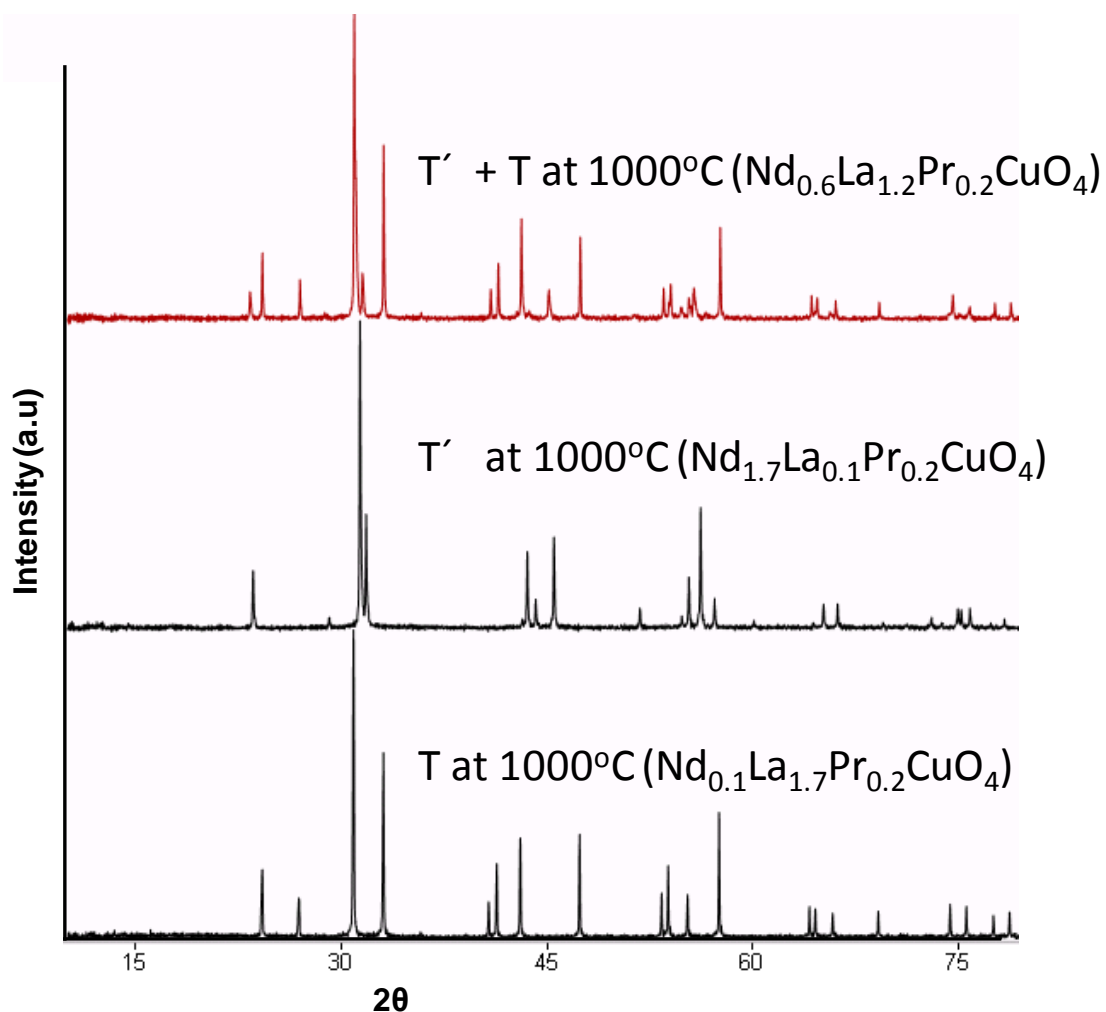


Figure 4.13: Comparison of XRD pattern for the $\text{Nd}_{1.8-x}\text{La}_x\text{Pr}_{0.2}\text{CuO}_4$ at 1000°C where $x=1.2$ (two phases) and $x=0.1$, $x=1.7$ where both are single phases. It is clear the $x=1.2$ spectra is a combination of T' and T

The single phase orthorhombic T - structure was found only between $1.6 \leq x \leq 1.8$ for the $\text{Nd}_{1.8-x}\text{La}_x\text{Pr}_{0.2}\text{CuO}_4$ system. This is very similar to the La_2CuO_4 structure. La_2CuO_4 is orthorhombic at room temperature; La_2CuO_4 undergoes a second order crystallographic transition, orthorhombic to tetragonal, near 533K with minor change in unit cell volume. (88,131). Similar to La_2CuO_4 , $\text{Nd}_{1.8-x}\text{La}_x\text{Pr}_{0.2}\text{CuO}_4$ undergoes tetragonal to orthorhombic phase transition at ~ 523 K due to this cooperative rigid tilting of the elongated CuO_6 octahedral along the 110 direction of the tetragonal unit cell. The In-situ XRD pattern for T/O

phase at different temperatures where $x=1.7$ composition were plotted in figure 4.15. $\text{Nd}_{1.8-x}\text{La}_x\text{Pr}_{0.2}\text{CuO}_4$ for tetragonal (T) and orthorhombic phases obtained space group $I4/mmm$ and $Bmab$ respectively.

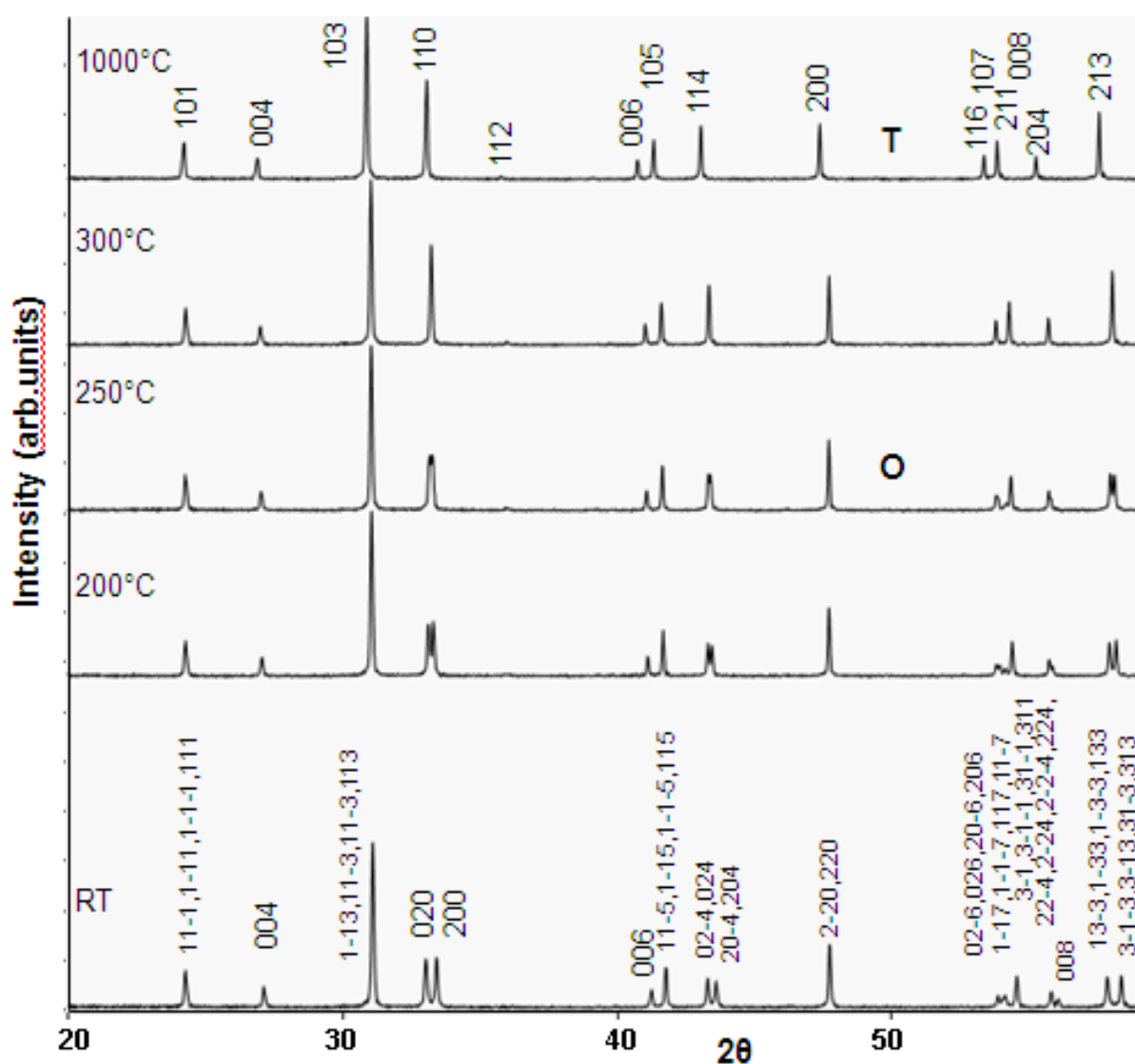


Figure 4.14: In-situ XRD pattern for T/O phase at different temperatures where $x=1.7$ composition

With summarizing all the in situ x-ray analysing data, it is easy to plot the phase transformation behaviour for the $\text{Nd}_{1.8-x}\text{La}_x\text{Pr}_{0.2}\text{CuO}_4$ with temperature. The phase transformation behaviour of this system is summarised in Figure 4.15.

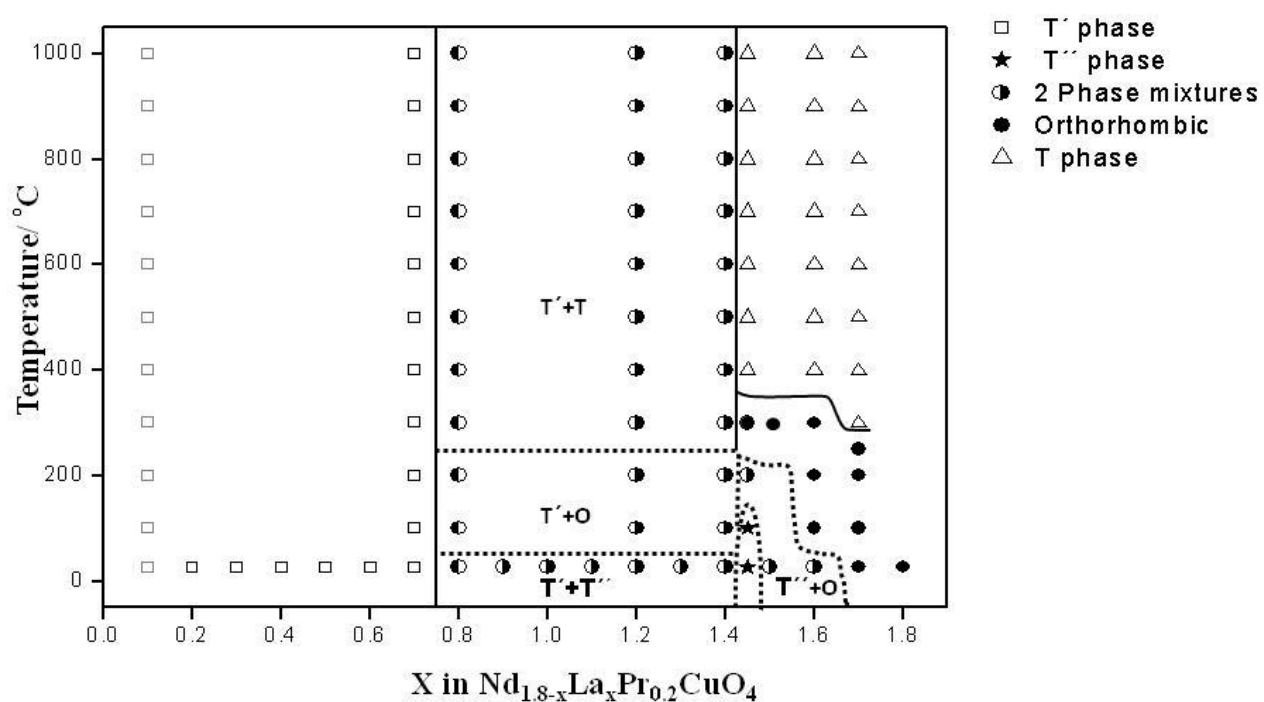


Figure 4.15: Phase relationship for $\text{Nd}_{1.8-x}\text{La}_x\text{Pr}_{0.2}\text{CuO}_4$ as a function of temperature, solid lines describe equilibrium phase boundaries; whereas dotted lines denote observed boundary regions involving the metastable (non-equilibrium) T'' phase

Figure 4.16 shows the equilibrium phase diagram for $\text{Nd}_{1.8-x}\text{La}_x\text{Pr}_{0.2}\text{CuO}_4$ which has been obtained using both 850°C and 950°C fired samples.

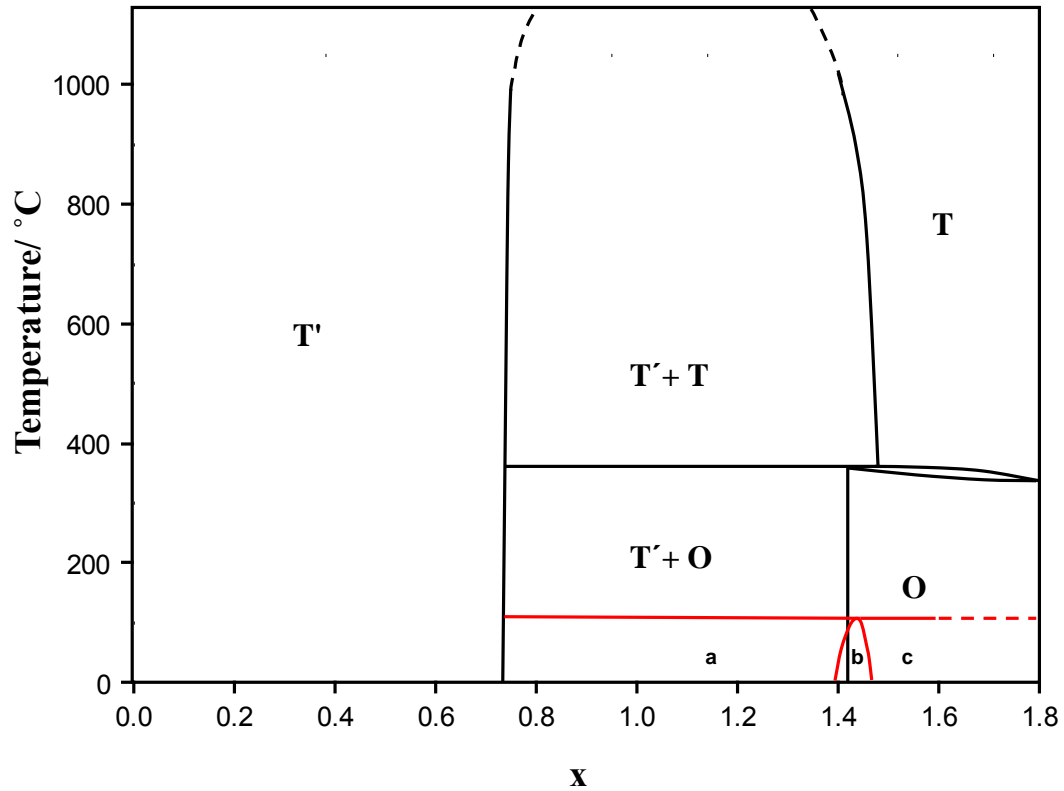


Figure 4.16: Phase diagram of $\text{Nd}_{1.8-x}\text{La}_x\text{Pr}_{0.2}\text{CuO}_4$ showing location of metastable T'' phase formed on rapid cooling at 950°C . Black lines show equilibrium phase boundaries, red lines mark approximate limits of the metastable T'' phase fields ($a = \text{T}' + \text{T}''$, $b = \text{T}''$, $c = \text{O} + \text{T}''$)

As shown in figure 4.16, there are three equilibrium phases for $\text{Nd}_{1.8-x}\text{La}_x\text{Pr}_{0.2}\text{CuO}_4$ at room temperature. They are, (1) monophasic T' solid-solution for $0.0 \leq x < 0.8$; (2) two phase mixture $\text{T}' + \text{O}$ for $0.8 \leq x < 1.45$; (3) monophasic O solid-solution for $1.45 < x < 1.8$. The metastable T'' phase has no place on this equilibrium phase diagram. On annealing any rapidly cooled sample with the compositions where $0.8 \leq x < 1.45$ at lower temperature the equilibrium spinodal product phases (T' and T/O) will be formed.

4.2.2 Thermal analysis

TGA data were obtained for the compositions where $x=0.0, 0.1, 1.7$ and 1.8 . In order to calculate the δ values for these $\text{Nd}_{1.8-x}\text{La}_x\text{Pr}_{0.2}\text{CuO}_{4+\delta}$ material thermogravimetric analysis under 5% hydrogen heating up to 800°C were carried. Detected mass lost (Z) were reported. Table 4.2 shows the detected mass losses and corresponding δ values for the NLPCO where $x=0.0, 0.1, 1.7$ and 1.8 .

TG indicated that reduction goes via mainly two steps. Copper is reduced via Cu(II) to Cu^0 . Final XRD diffraction studies also confirmed that Cu(II) was reduced to metallic copper and Pr was reduced to +3 oxidation state (present as Pr_2O_3).

Therefore material was reduced as below under 5% hydrogen.

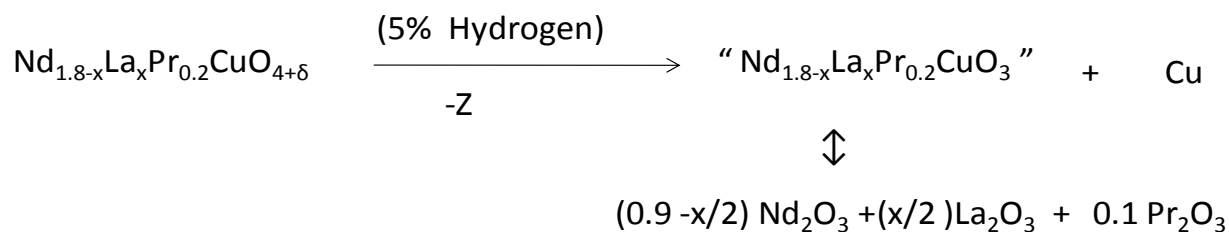


Table 4.2: Detected mass lost and corresponding δ values

La level (x)	Mass lost (Z) %	δ
0.00	3.78 (2)	-0.010(5)
0.10	3.76 (1)	-0.025(3)
1.70	3.79 (1)	-0.038(3)
1.80	3.81 (1)	-0.034(3)

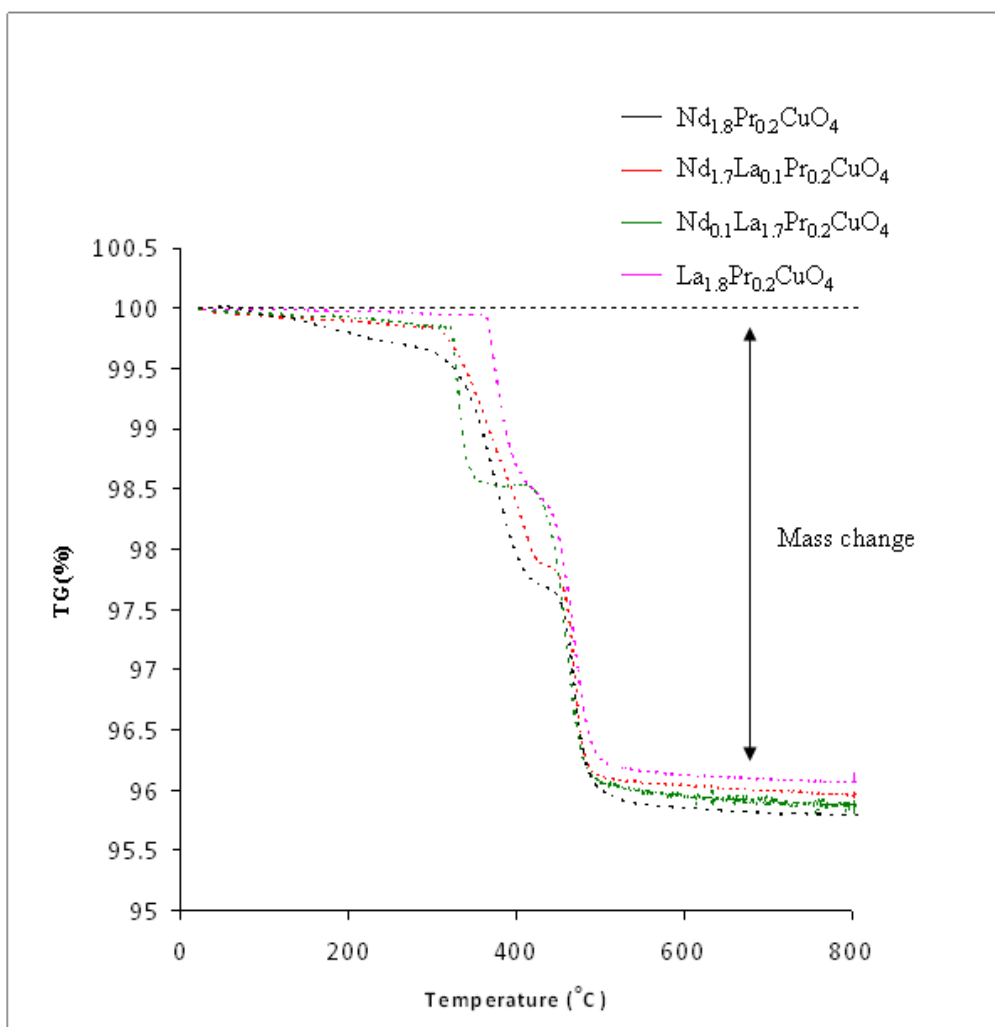


Figure 4.17: Thermogravimetric analysis under 5% Hydrogen heating up to 800 $^{\circ}\text{C}$

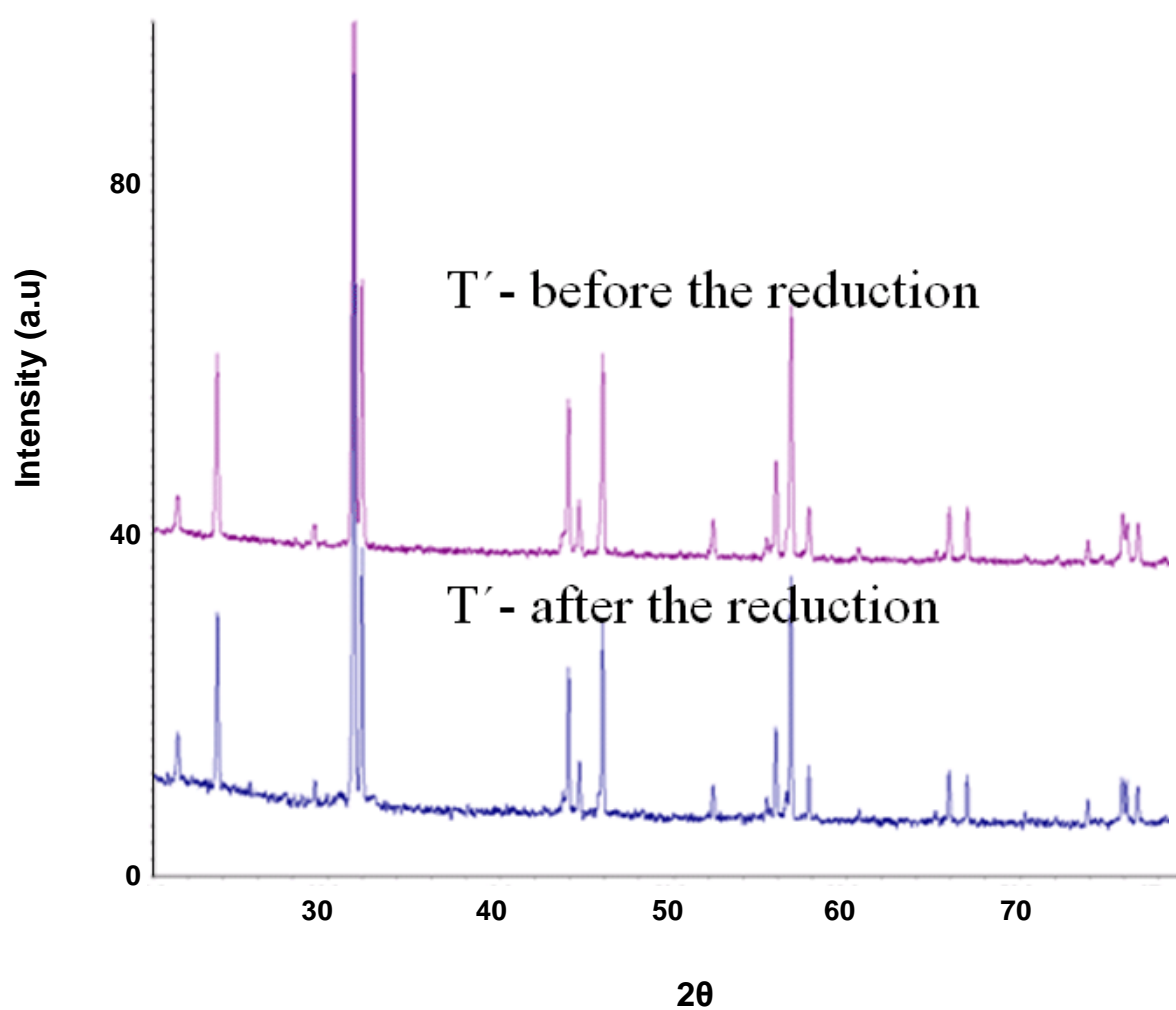


Figure 4.18: XRD pattern for the T' phase ($\text{Nd}_{1.8}\text{Pr}_{0.2}\text{CuO}_4$) before and after the reduction with 5% H_2 up to 300 °C

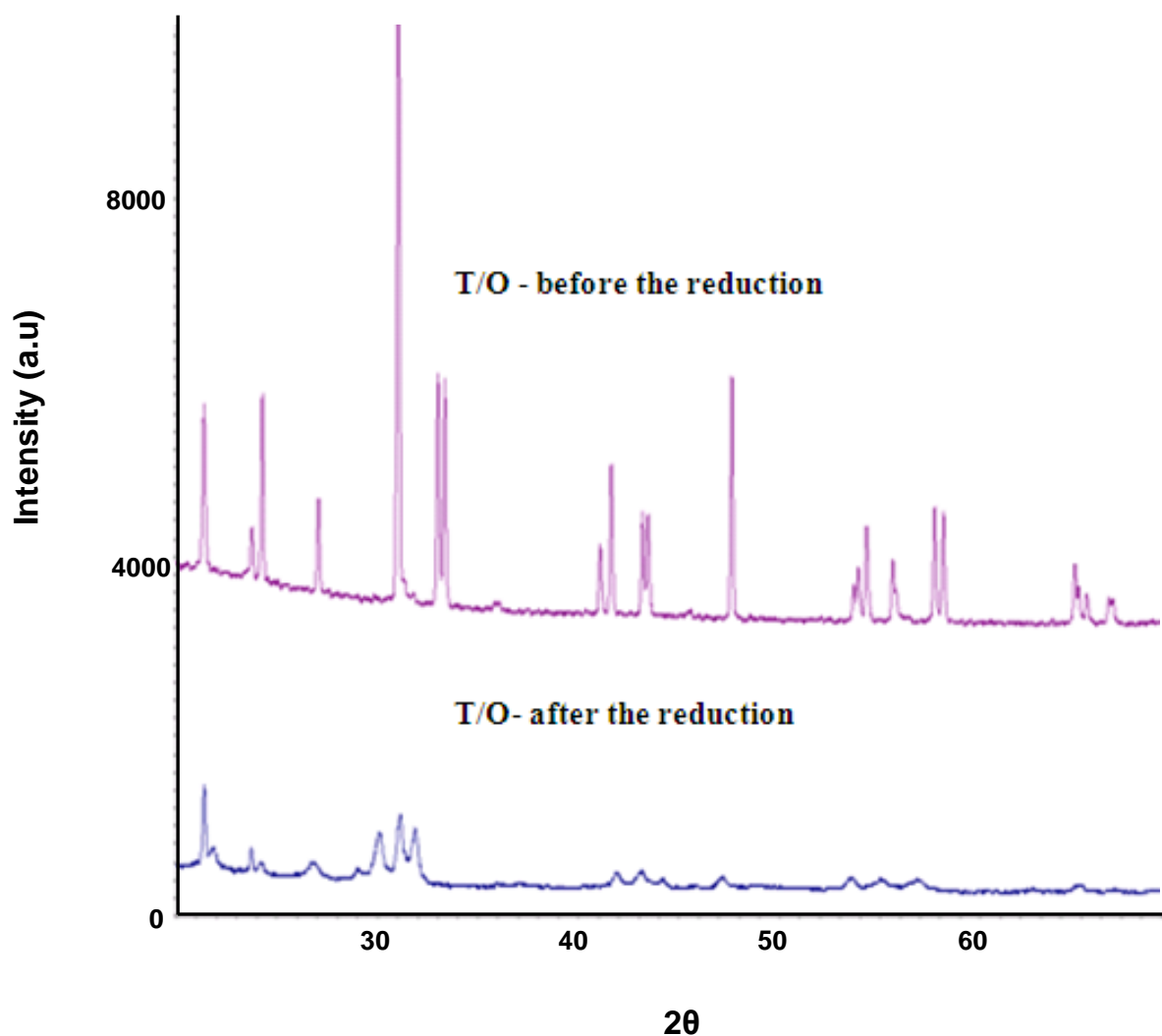


Figure 4.19: XRD pattern for the T/O phase ($\text{La}_{1.8}\text{Pr}_{0.2}\text{CuO}_4$) before and after reduction with 5% H_2 up to 300 °C

Thermo gravimetric analysis data in figure 4.17 show orthorhombic phase ($\text{La}_{1.8}\text{Pr}_{0.2}\text{CuO}_4$ and $\text{Nd}_{0.1}\text{La}_{1.7}\text{Pr}_{0.2}\text{CuO}_4$) and tetragonal T' phase ($\text{Nd}_{1.8}\text{Pr}_{0.2}\text{CuO}_4$ and $\text{Nd}_{1.7}\text{La}_{0.1}\text{Pr}_{0.2}\text{CuO}_4$) have slight different reduction behaviour. Orthorhombic phase shows stability up to *ca* 370 °C before starting the reduction step, but XRD patterns obtained for the orthorhombic phase (T/O) and T' phase after the reduction with 5% H_2 up to 300 °C indicate that T' phase remains the same phase after the low temperature reduction while the orthorhombic phase changes its crystal structure. Therefore T' is much stable than the orthorhombic phase at reducing

atmosphere at low temperatures (below to 300 °C). This could be an important property for low temperature anode side applications.

4.2.3 Electrical characterisation

Electrical characterisation of lanthanum-doped neodymium praseodymium copper oxide ($\text{Nd}_{1.8-x}\text{La}_x\text{Pr}_{0.2}\text{CuO}_4$) with respect to lanthanum content, temperature and oxygen partial pressure was performed for the phase compositions ($x=0.0, 0.1, 0.2, 0.3, 1.7$ and 1.8) to determine which composition has the maximum conductivity and whether this remains so at different temperatures. As shown in figure 4.20 conductivities were measured against temperature using four compositions for T' phase (where $x=0.0, 0.1, 0.2$ and 0.3) and two compositions of orthorhombic T phase ($x=1.7$ and 1.8). T' phase is remain all over the temperature, but room temperature orthorhombic phase change to T phase at high temperature, therefore this phase is denoted as T/O phases in figure 4.20. The conductivity data also shows that the orthorhombic compositions have a significantly lower conductivity than the T' phase. In order to see clearly, orthorhombic phase's conductivities were plotted again in separate figure in 4.21.

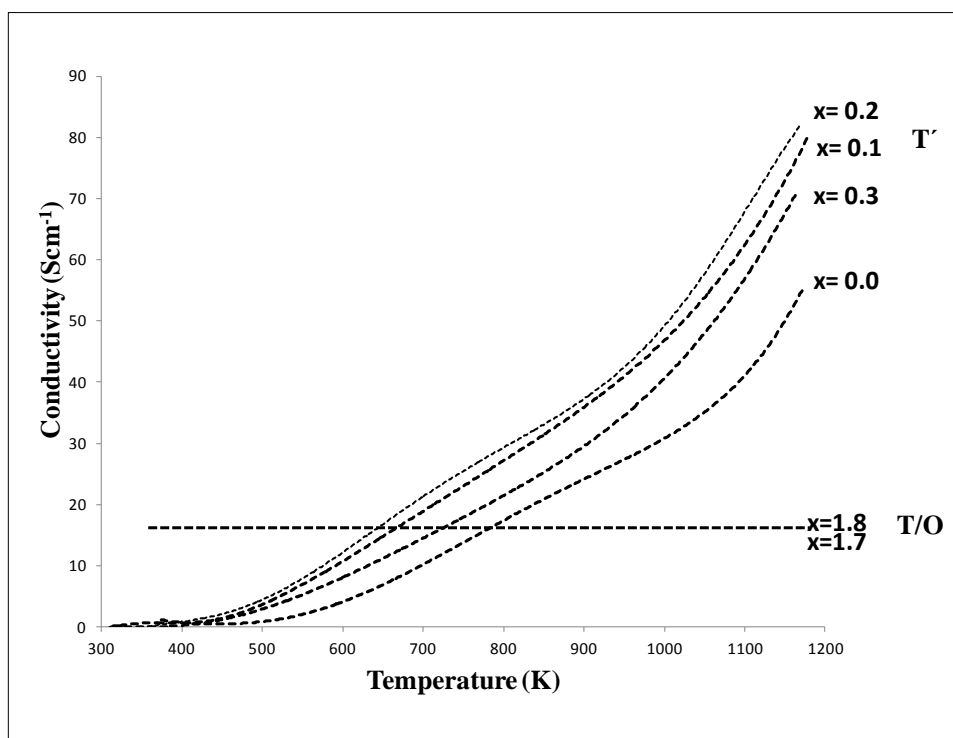


Figure 4.20: DC conductivity data for $\text{Nd}_{1.8-x}\text{La}_x\text{Pr}_{0.2}\text{CuO}_4$ in air where $x=0.0, 0.1, 0.2, 0.3, 1.7$ and 1.8

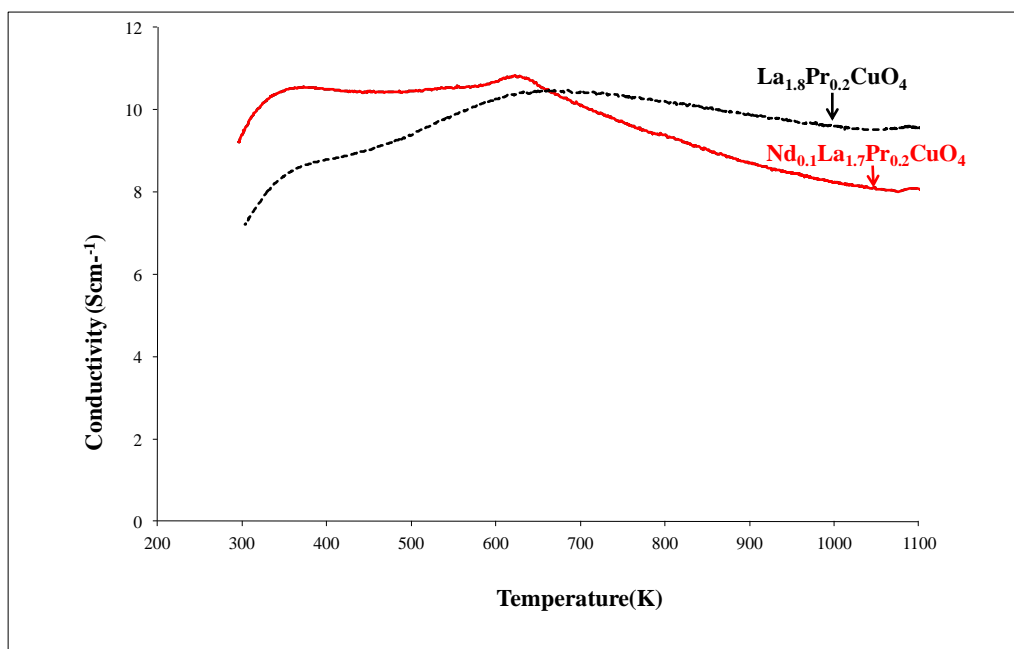


Figure 4.21: DC conductivity data for $\text{Nd}_{1.8-x}\text{La}_x\text{Pr}_{0.2}\text{CuO}_4$ in air where $x=1.7$ and 1.8

Table 4.3: NLPCO conductivity in air

Composition x	Conductivity Scm-1 (At 700 °C)	Conductivity Scm-1 (At 800 °C)	Conductivity Scm-1 (At 900 °C)
0.0	28.3	38.0	54.0
0.1	42.9	57.9	80.7
0.2	45.1	61.1	90.1
0.3	36.8	52.7	71.2
1.7	8.00	7.97	8.65
1.8	9.68	9.55	9.44

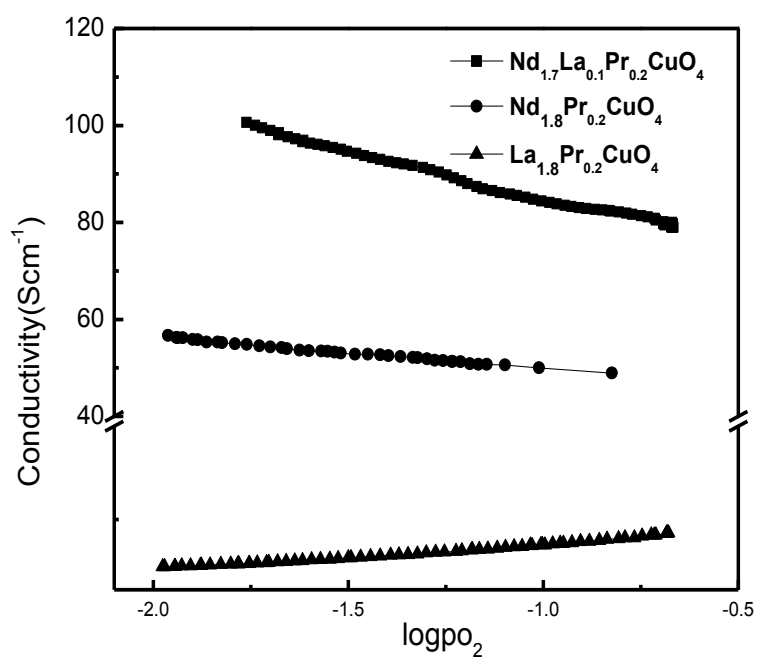


Figure 4.22: Log pO₂ vs conductivity for Nd_{1.8-x}La_xPr_{0.2}CuO₄ for single phase compositions

These data were measured after approximately the same conditioning protocol for all the tests and suggest that a maximum conductivity may exist around a dopant level is around 0.2. Further increasing the dopant level leads to decrease the conductivity ($x=0.3$). Interesting property of this material is that the electrical properties can be improved with the small concentration of lanthanum. The conductivity data also shows that the orthorhombic compositions have a significantly lower conductivity than the T' phase. Figure 4.20 shows that the material behaves as a pure semiconductor up to $x=0.3$ while heavily lanthanum doped samples (Figure 4.21) show both semiconducting and metallic behaviour with the transition to the latter at temperatures above 600 °C, although another, less distinct transition may also occur around 300°C. La_2CuO_4 was observed to show metallic behaviour and slight anomaly in the conductivity was noted at around 310 °C (132) while Nd_2CuO_4 is semiconducting. An orthorhombic to tetragonal transition was reported for La_2CuO_4 at about 533 K (133). Semiconductor to metallic transition was obtained for $\text{La}_{1.8}\text{Pr}_{0.2}\text{CuO}_4$ around for 600 K. This probably due to phase transition from orthorhombic to tetragonal .

The conductivity with respect to oxygen partial pressure shows an increase in conductivity with decreasing $p(\text{O}_2)$ for low La level single phase compositions, which indicates that this material is a n-type semiconductor. Pr stays in the system as +4 and introduces electrons to the system. However the orthorhombic $\text{La}_{1.8}\text{Pr}_{0.2}\text{CuO}_4$ shows p-type behaviour with conductivity decreasing as $p(\text{O}_2)$ also decreases. In both materials, conductivity has been found to drop dramatically as the oxygen partial pressure below around 10^{-4} atmospheres. This has been attributed to reduction on the $\text{Cu}^{2+/1+}$ cation to Cu^0 with the decomposition of the phase structure and the exsolution of metallic copper.

4.2.4 Magnetisation measurements

Magnetic properties were investigated for T' and O phases using compositions $\text{Nd}_{1.8}\text{Pr}_{0.2}\text{CuO}_4$ and $\text{La}_{1.8}\text{Pr}_{0.2}\text{CuO}_4$ respectively. SQUID measures the magnetic flux through a sense coil due to the sample magnetic moment. The magnetic behaviour was investigated measuring the magnetization versus temperature and magnetic field.

Fig. 2A and 2B show the field-cooled (FC) and zero-field-cooled (ZFC) magnetisation vs. temperature for different compositions of $\text{Nd}_{1.8-y}\text{La}_y\text{Pr}_{0.2}\text{CuO}_4$ (A and B are where $\text{La} = 1.8$ and 0.0 respectively) measured with an applied field of $H = 500$ Oe. Zero field measurements also carried out at temperature down to 5K.

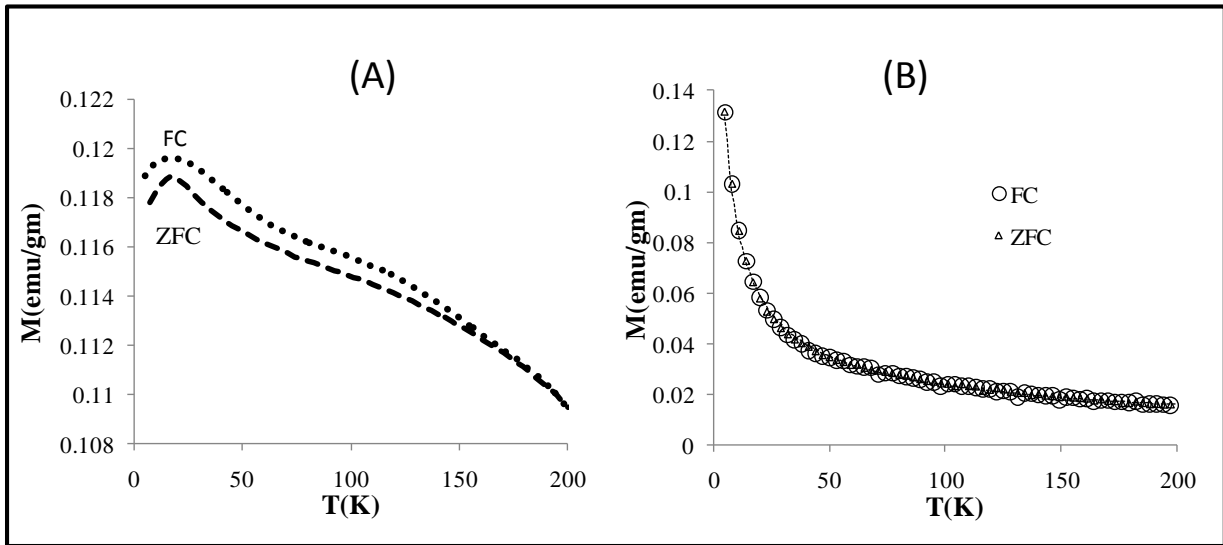


Figure 4. 23: (A): FC and ZFC Magnetization versus temperature For $\text{La}_{1.8}\text{Pr}_{0.2}\text{CuO}_4$, (B) FC and ZFC Magnetization versus temperature for $\text{Nd}_{1.8}\text{Pr}_{0.2}\text{CuO}_4$

Figure 4.23 (A) shows the temperature dependence of the dc magnetization in ZFC and FC conditions for orthorhombic phase of $\text{La}_{1.8}\text{Pr}_{0.2}\text{CuO}_4$ composition and ZFC curve shows a low temperature antiferromagnetic type transition at 16 K. In order to understand this magnetic behaviour, magnetization vs field was plotted (figure 4.24). It shows weak hysteresis which is good indicative of antiferromagnetism.

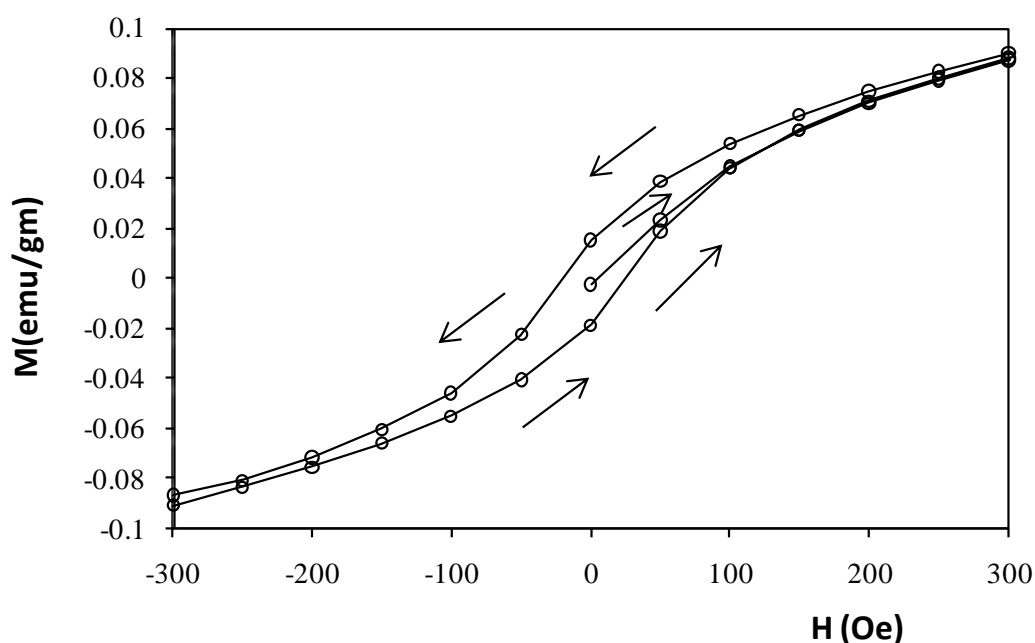


Figure 4.24: Magnetization versus magnetic field at 5 K for $\text{La}_{1.8}\text{Pr}_{0.2}\text{CuO}_4$

The tetragonal T' phase of $\text{Nd}_{1.8}\text{Pr}_{0.2}\text{CuO}_4$ showed paramagnetic magnetic behaviour (figure 4.23 B). Luke et al firstly proposed the magnetic phase diagram of the electron-doped system $\text{Nd}_{2-x}\text{Ce}_x\text{CuO}_4$ (NCCO) [134]. In this phase diagram T_n gradually decreases upon electron doping and at 0.15 Ce concentration antiferromagnetic ordering suddenly disappears and the optimum superconductivity (T_c around 25K) appears. In this study we were unable to see any superconducting property for the $\text{Nd}_{1.8}\text{Pr}_{0.2}\text{CuO}_4$ (T' phase) and $\text{La}_{1.8}\text{Pr}_{0.2}\text{CuO}_4$ (O phase) systems.

4.3 Conclusions

General material characterization for $\text{Nd}_{2-x-y}\text{La}_x\text{Pr}_y\text{CuO}_4$ was done using X-ray diffraction, magnetization, thermogravimetric analysis and conductivity measurements. The $\text{Nd}_{1.8-x}\text{La}_x\text{Pr}_{0.2}\text{CuO}_4$ system was studied varying the La level ($0 \leq x \leq 1.8$) compositions and then characterised using high temperature X-ray powder diffraction. From analysis of the XRD patterns obtained at room temperature there were clearly five distinguishable regions for the $\text{Nd}_{1.8-x}\text{La}_x\text{Pr}_{0.2}\text{CuO}_4$ system with three single phases (T' , T'' and O). They are, (1) monophasic T' solid-solution for $0.0 \leq x < 0.8$; (2) two phase mixture $T' + T''$ for $0.8 \leq x < 1.4$; (3) monophasic T'' solid-solution for $1.4 < x < 1.5$; (4) two phase mixture $T'' + O$ for $1.5 \leq x < 1.6$; and (5) monophasic O-phase solid-solution for $1.6 \leq x \leq 1.8$.

A new tetragonal symmetry phase, T'' , was found similar to the well-known T' type structure which has slightly larger a and c axes. This phase coexists with T' phase for $0.8 \leq x \leq 1.4$ and occurs as a very narrow solid solution at $1.4 < x < 1.5$. T'' structure is strongly dependent on the firing temperature. In order to form T'' phase it has to be fired above 900°C .

The T' phase was stable up to 1000°C without any compositional separation or phase transition for compositions $0.0 \leq x < 0.8$. A tetragonal (T) to orthorhombic phase transition occurred at $\sim 523\text{ K}$ for the composition $1.6 \leq x \leq 1.8$. Replacement of a greater amount of the smaller Nd^{3+} by larger La^{3+} increased the bond length mismatch for the T' phase, which will lead to changes in c axis oxygen replacing the rock salt layer in the place of fluorite layer. T'' phase exhibited a narrow homogeneity range near $x = 1.45$. This T'' can be considered as a non transformable metastable structure. Interestingly non transformable T'' was formed from quenching of T phase. O is an orthorhombically distorted variant of the T-phase. For the composition $\text{Nd}_{0.35}\text{La}_{1.45}\text{Pr}_{0.2}\text{CuO}_4$ with significant Nd content, the T phase exists at high temperature then transforms via the O phase to the T'' phase at low

temperatures. After prolonged annealing at e.g. 850°C the T'' phase does not appear on cooling as the the T phases undergoes a spinodal decomposition into lower and higher Nd content T' and T/O phases. Even though T' and T'' have similar XRD patterns, the high temperature phase transition behaviour of T'' was more similar to T/O phase. Replacement of Nd³⁺ by sufficient larger La³⁺ in Nd_{2-x-y}La_xPr_{0.2}CuO₄ relieves the mismatch along the series by forming T structure; however, the strain in this T phase cannot be sustained to lower temperature resulting in the non-transformable metastable T'' phase. On adding sufficient La the T/O phase become fully stabilised. Magnetic measurements indicated that paramagnetic behaviour is obtained for T' phase while antiferromagnetic behaviour is obtained for T phase. Dc conductivity measurements indicate tetragonal phase follows n-type semiconductor behaviour and will increase the conductivity using small concentration of Lanthanum (up to x= 0.2). Orthorhombic phase shows p-type metallic behaviour while having low conductivities.

Chapter five -T'' non-transformable phase from quenching of La₂CuO₄ (T) type structures

5.0 Introduction

Apart from T' and T phases, a new phase called T'' has been reported for the Nd₂CuO₄-La₂CuO₄ system where $x \approx 1.5$ in Nd_{2-x}La_xCuO_{4±δ} which has a similar X-ray diffraction pattern to T' with slightly larger a and c parameters than the T' phase. It has been suggested that, in accord with its stoichiometry, T'' contains a unique cation ordering which is roughly 3(Ln):1(Ln') in Ln-O layer and interlayer ordering at the Ln₃Ln' composition and it has been claimed as an equilibrium phase (76, 77, 91). Hypotheses and suggestions on this T'' phase in literature vary and have not been confirmed. Therefore we have explored this system in detail with temperature dependent X-ray diffraction, SAED, neutron diffraction and conductivity measurements.

5.1 Methods used

The T'' phase was synthesised for the Nd_{0.35}La_{1.45}Pr_{0.2}CuO_{4±δ} composition by solid state reaction. Hygroscopic powders (Nd₂O₃, Pr₆O₁₁, La₂O₃) were dried for 30 minutes at temperatures up to 900 °C. Stoichiometric amounts of Nd₂O₃ (Alfa-Aeser 99.9%), Pr₆O₁₁ (Alfa-Aeser 99.9%), CuO (Aldrich 99+ %) and La₂O₃ (Aldrich 99.99%) were then weighed and ground in acetone. These mixtures were then dried and calcined in air at 850 °C for 36 hours. Following this powders were reground using the planetary ball mill and the heat treatment (850 °C for 36 hours) repeated. The sample was reheated at 950 °C for 24 hours.

In-situ X-ray diffraction analysis of powders were collected at room temperature on a Bruker axs D8 advance diffractometer equipped with a solX energy dispersive detector in the 10–90° range with a step of 0.02° and accounting time of 25 s per step (CuKα = 1.5406 Å). The high

temperature diffraction data were collected in the 10–90° range, with a step of 0.0148° and a counting time of 1.5 s per step, on a Bruker axs D8 advance diffractometer equipped with a high temperature Anton Paar HTK 1200N chamber and a one dimensional X-ray detector VÅNTEC-1 ($\text{CuK}\alpha = 1.5406 \text{ \AA}$). FULLPROF software (123) was used to perform least square refinement of the lattice parameters of the samples.

High resolution and high intensity time-of-flight neutron powder diffraction (NPD) data were collected using GEM diffractometer at the ISIS spallation source at Rutherford Appleton laboratory, UK. The sample (ca. 5 g) was loaded into a thin-walled, cylindrical vanadium can and placed in the sample chamber in ambient conditions. The diffraction data sets were analysed using the Rietveld method (121,122) in GSAS package (124).

Selected area electron diffraction patterns were collected in different orientations on a Jeol JEM-2011 electron microscope operated at 200 kV. The powder sample was ground using a mortar and pestle, and suspended in acetone. One drop of suspension was deposited on a copper grid with a holey carbon film.

Thermogravimetric analysis was carried out on a NETZSCH TG 209 instrument to evaluate the oxygen content (from weight loss) at different temperatures in air and to compare with neutron diffraction results. The initial weight of the sample was about 20 mg. The effect of buoyancy was corrected using empty crucible blank runs under corresponding gas atmosphere and flow rates. The samples were heated up to 1000 °C in the TG furnace at a heating rate of 5 °C min⁻¹ in air and under flowing 5% Hydrogen/95% Argon (Flow rate: 30ml/min). The excess/deficiency of oxygen ($\pm\delta$) was calculated from the detected mass change.

Electrical properties were measured using small circular pellets. Powders were uniaxially pressed using a pressure of 120 MPa. The pellets had a diameter of 13 mm with a thickness

of 1-2 mm and were fired in air for 10 hours at 850 °C. In-situ conductivity was measured using a four point DC technique from 900 °C to room temperature in air using Van der Pauw technique (125,126).

5.2 Results and Discussion

T'' phase formation was explored for the composition Nd_{0.35}La_{1.45}Pr_{0.2}CuO₄. XRD data were obtained on cooling from 1000 °C. These in situ X-ray diffraction studies indicate that T'' phase form via orthorhombically distorted variant (O) of the T-phase (figure 5.1).

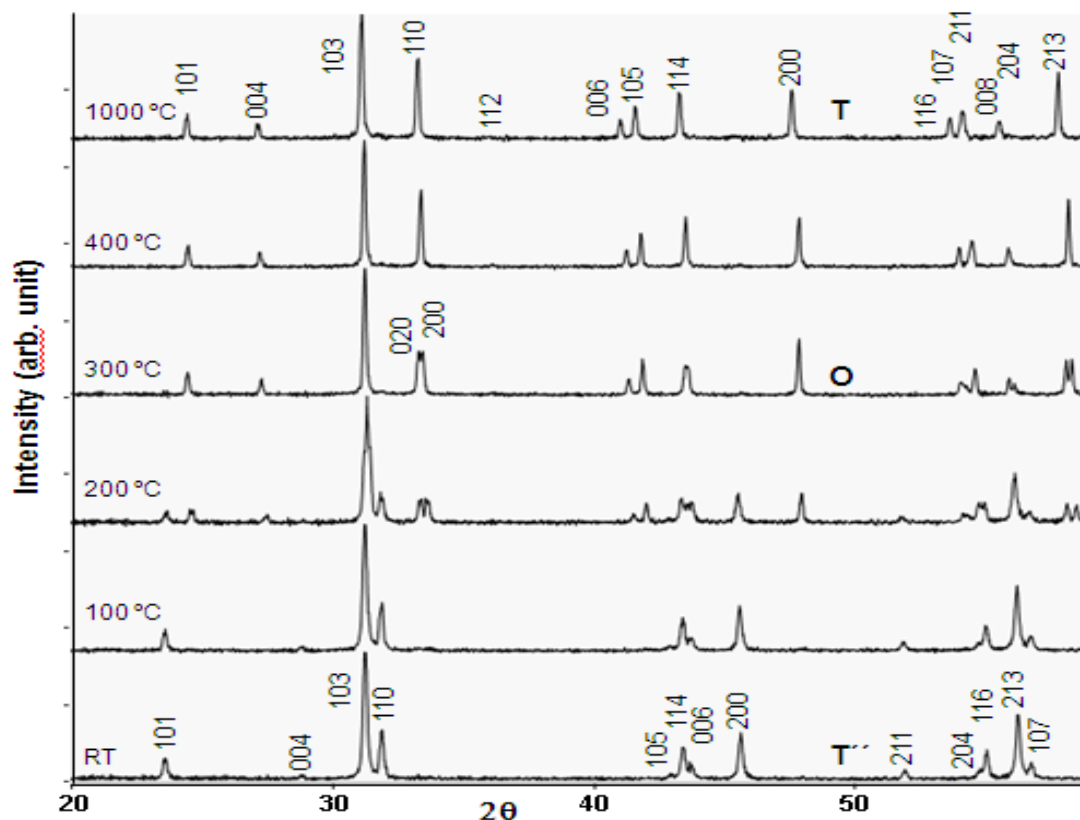


Figure 5.1: In-situ XRD pattern for T'' phase at different temperatures where x = 1.45 composition

The T'' has tetragonal symmetry similar to the well-known T' type structure, it has slightly larger a and c axes and c/a ratio compared to T' . For the composition $\text{Nd}_{0.35}\text{La}_{1.45}\text{Pr}_{0.2}\text{CuO}_4$ with significant Nd content, the T phase exists at high temperature then transforms to a metastable T'' phase at low temperatures (*ca* 200 °C). This final transition is accompanied by a very large change in unit cell shape, as indicated by the large difference in c/a between T and T'' phases (Figure 2). On changing from T -type to T'' -type volume increases by 5%, a increases by 5%, c decreases by 5% and c/a ratio decreases by 10%. Not surprisingly, ceramic pellets going through the T to T'' transition transform to fine powders, typically with 15 minutes of cooling to room temperature (figure 5.4).

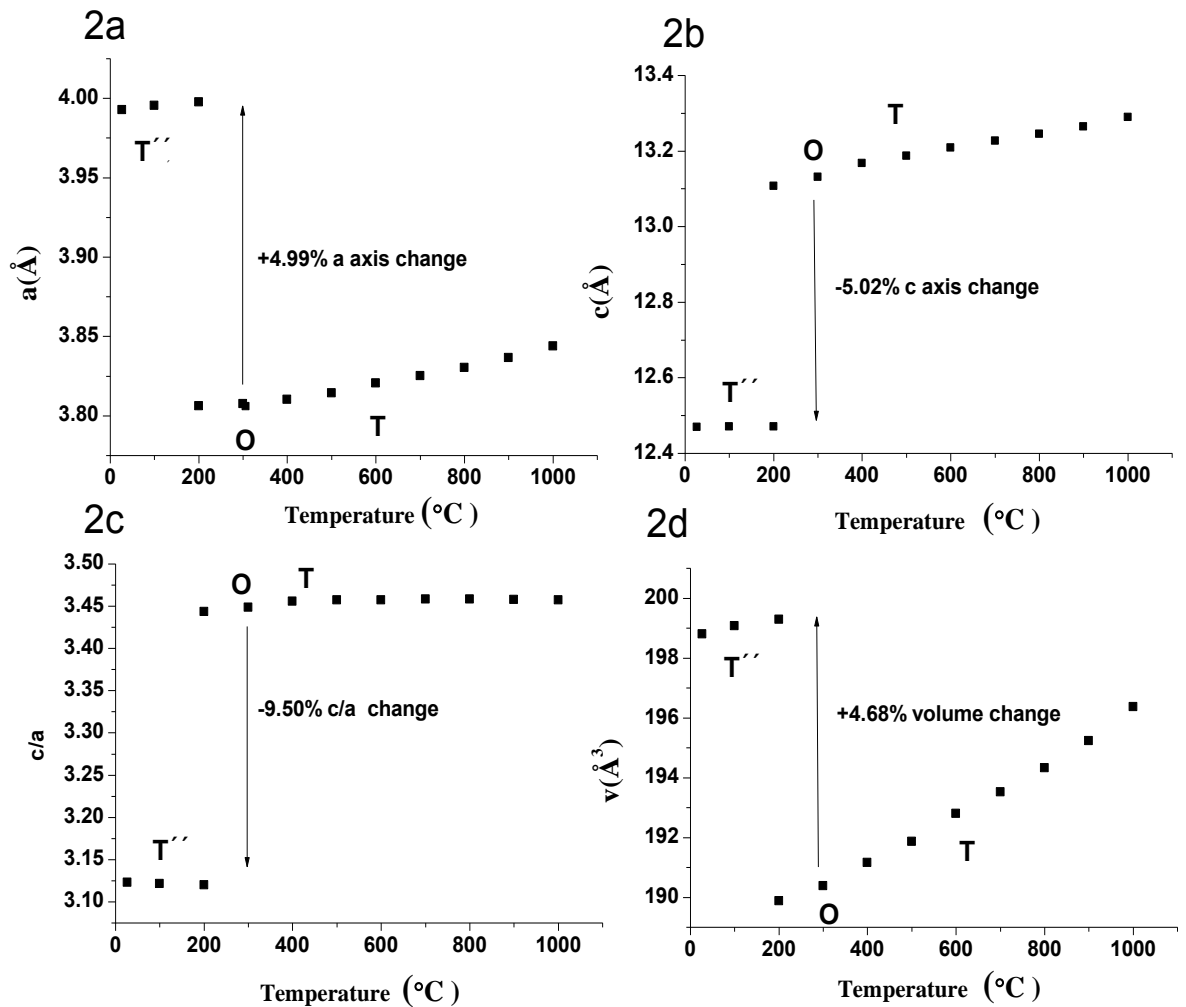


Figure 5.2: Variation of lattice parameters a (a), lattice parameter c (b), c/a ratio (c) and volume v (d) with temperature for $\text{Nd}_{0.35}\text{La}_{1.45}\text{Pr}_{0.2}\text{CuO}_4$

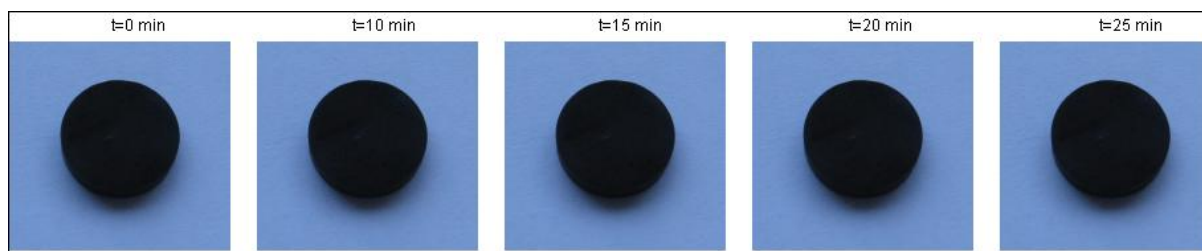


Figure 5.3: Images of 850 °C annealed $\text{Nd}_{0.35}\text{La}_{1.45}\text{Pr}_{0.2}\text{CuO}_4$ pellet with time

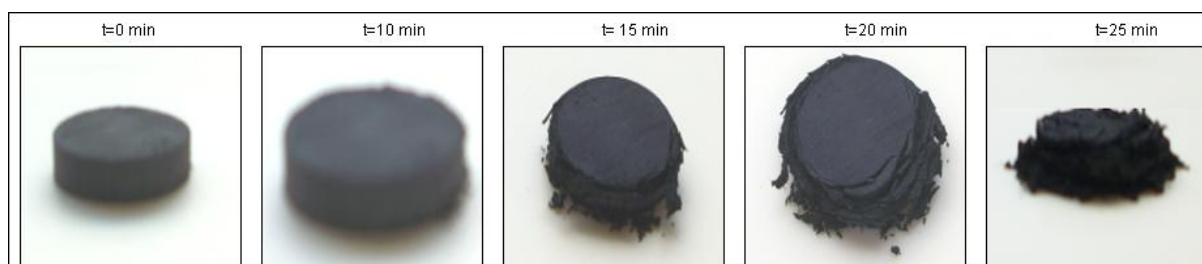


Figure 5.4: Images of 950 °C fired $\text{Nd}_{0.35}\text{La}_{1.45}\text{Pr}_{0.2}\text{CuO}_4$ pellet with time

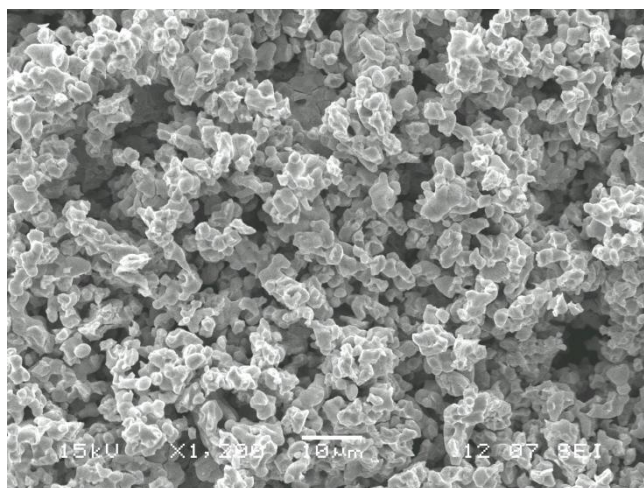


Figure 5.5: SEM image of the fine powder which was obtained of from a dense pellet of $\text{Nd}_{0.35}\text{La}_{1.45}\text{Pr}_{0.2}\text{CuO}_4$ after firing at 950 °C for 10 hours and cooling to room temperature

After prolonged annealing at lower temperature (e.g. 850 °C, 600 °C) the T'' phase does not appear on cooling as the T phases undergoes a spinodal decomposition into higher and lower Nd content T' and T/O phases (figure 5.6). Therefore the T'' phase only forms on relatively fast cooling, which does not allow the necessary diffusion of ions and the compositional adjustment required for the low temperature equilibrium phases to form. Therefore high temperature T phase undergoes a diffusionless transition to the metastable T'' phase. This is reminiscent of the metastable t' phase often reported in the yttria stabilized zirconia system (135). It depends on the grain size, cooling rate and content of the Y_2O_3 (136). Similar to the t' phase in the yttria stabilized zirconia system, the T'' phase has no place on the equilibrium phase diagram. On annealing any rapidly cooled sample at lower temperature the equilibrium spinodal product phases (T' and T/O) will be formed.

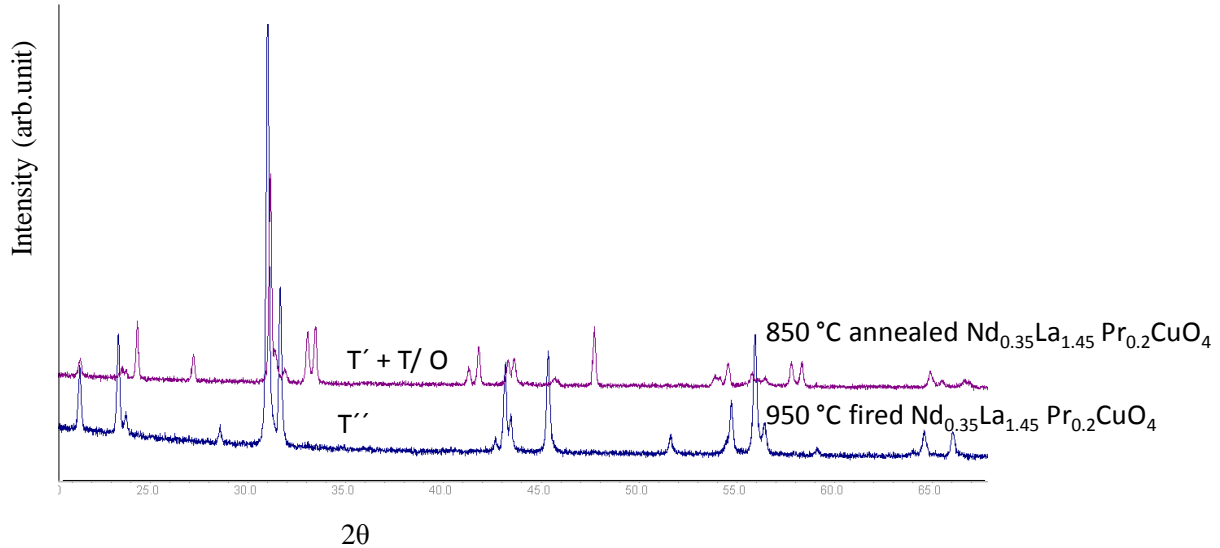


Figure 5.6: Comparison of XRD graphs at 950 °C fired sample and 850°C annealed samples for the composition $Nd_{0.35}La_{1.45}Pr_{0.2}CuO_4$

The T'' phase has only been obtained in a very narrow region where $1.4 < x < 1.5$ for this $Nd_{1.8-x}La_xPr_{0.2}CuO_4$ system. For higher La content the T phase is stabilised to room

temperature (although as its orthorhombically distorted variant). For lower La content the T' phase is stabilised to room temperature. The observed T'' phase must have a lower energy than the corresponding T phase, but the T'' phase is still metastable at room temperature.

The symmetry of the two phases T and T' are similar, both can be represented by the space group $I4/mmm$, but crystallographically these two tetragonal phases are different. The structure of the T'' phase has been investigated by neutron diffraction (Figure 5.7) and electron diffraction (Figure 5. 8) studies. These show the typical patterns for the 4 coordinated Cu tetragonal $I4/mmm$ phase but have larger a and c axes compared to the T' phase. From the NPD studies, oxygen deficiency is calculated ($\delta=0.03$).

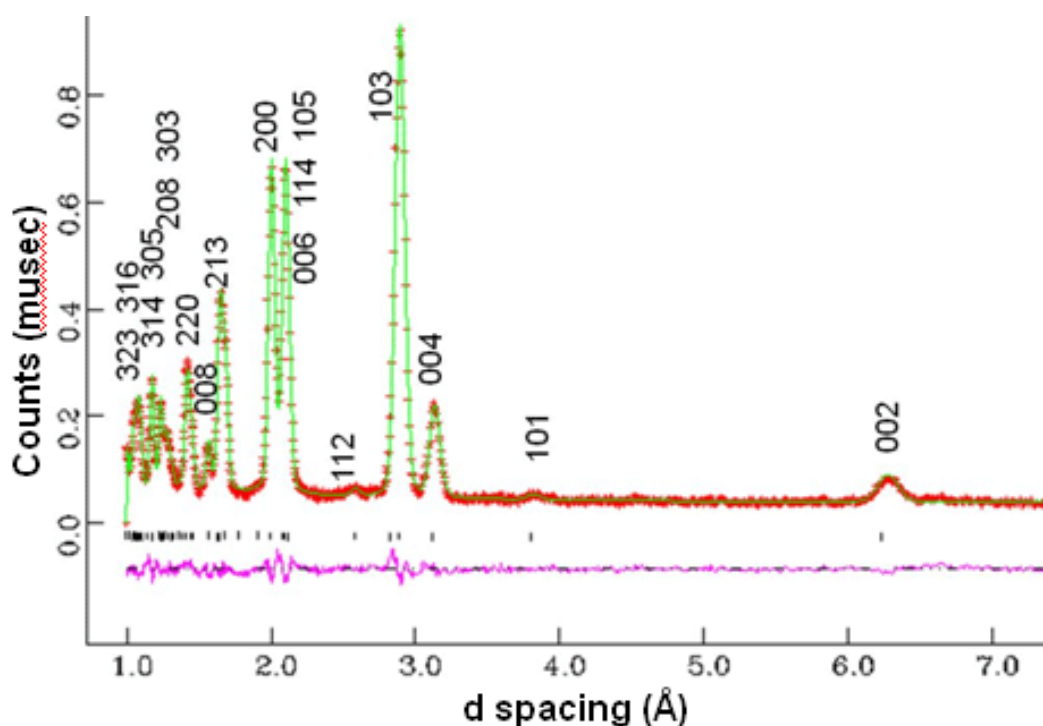


Figure 5.7: Rietveld refinement profile of T'' at room temperature in the $I4/mmm$ space group. Observed (plus sign), calculated (continuous line) and Bragg reflections (vertical lines) are shown

Table 5.1: Refined structural parameters of Nd_{0.35}La_{1.45}Pr_{0.2}CuO₄ at room temperature (295K)

Chemical cell: s.g. I4/mmm, $a = b = 4.0065(1)\text{\AA}$, $c = 12.5255(5)\text{\AA}$. $R_p = 6.5\%$, $R_{wp} = 4.34\%$, $\chi^2 = 7.73$.

Atom	Positions	x	y	Z	B (\AA^2)	Occupancy
La	$4e$	0.00	0.00	0.3520(1)	0.32(4)	1.45
Nd	$4e$	0.00	0.00	0.3520(1)	0.32(4)	0.35
Pr	$4e$	0.00	0.00	0.3520(1)	0.32(4)	0.2
Cu	$2a$	0.00	0.00	0.00	0.58(6)	1.0
O(1)	$4c$	0.00	0.50	0.00	1.02(6)	1.992
O(2)	$4d$	0.00	0.50	0.25	0.84(5)	1.978

T and T'' phases have different atomic positions (Table 5.2, Table 5.3). The rapid transformation from T to T'' is associated with a displacement of oxygen atoms in the c direction, with a corresponding change in lattice parameters. The figure 5.9 shows the interstitial oxygen changes during T to T'' phase transition along the z direction.

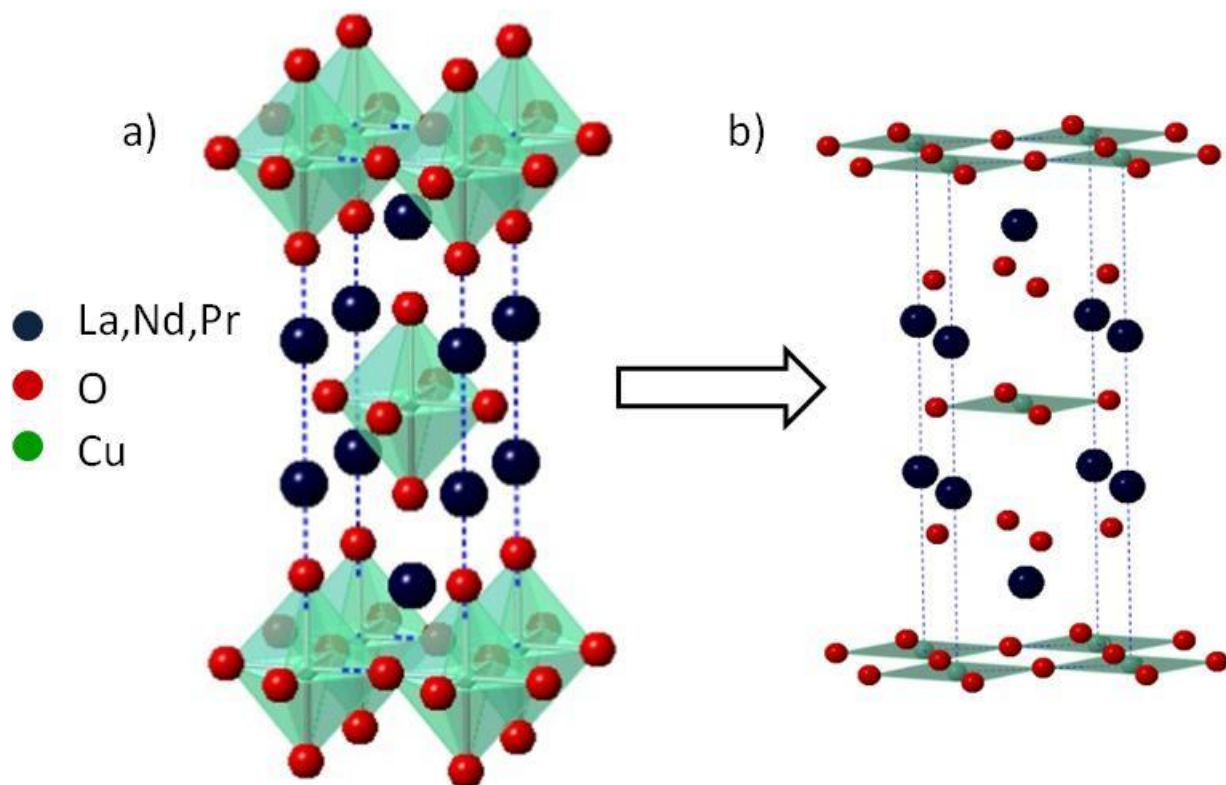


Figure 5.8: Schematic 3D diagram of $\text{Nd}_{0.35}\text{La}_{1.45}\text{Pr}_{0.2}\text{CuO}_4$ at 400 °C (a) and room temperature (b)

Table 5.2: Atomic positions for T phase

Atom	x	y	z
Ln	0	0	0.3606(1)
Cu	0	0	0
O1	0	0.5	0
O2	0	0	0.1828(1)

Table 5.3: Atomic positions for T'' phase

Atom	x	y	z
Ln	0	0	0.3520(1)
Cu	0	0	0
O1	0	0.5	0
O2	0	0.5	0.25

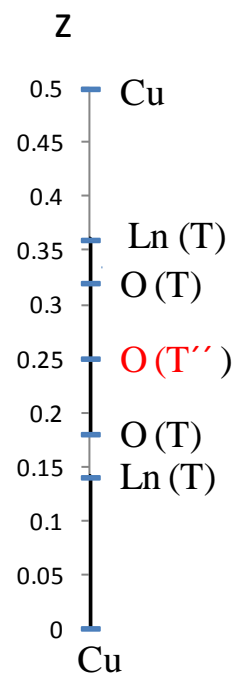


Figure 5.9: Schematic diagram of interstitial oxygen change during T to T'' transition. Figure has been drawn along the z direction

Oxygen moves along both y and z directions ($y=0.0$ to 0.5 and $z=0.1828$ to 0.25) when it transform to T to T'' phase and figure 5.9 showed only oxygen movement along the z direction. The main strategy of the neutron diffraction was to refine the oxygen positions. For the refinement of neutron diffraction pattern of T'' phase, different oxygen positions (T'- 4 fold Cu, T- 6 fold Cu and finally T* - 5 fold Cu) were used, but refinement is only possible when it is 4 fold similar to T'.

Therefore when it transforms from T to T'' Cu coordination changes from 6 to 4. That means that octahedral oxygen will move well away from the apical position leading to formation of fluorite type layers in Ln-O layers.

T'' phase occurs at very narrow compositional range ($\text{Nd}_{0.35}\text{La}_{1.45}\text{Pr}_{0.2}\text{CuO}_4$) where larger cation (La) : smaller cation (Pr or Nd) is nearly 3:1. Manthiram and Goodenough (76, 77, 91)

proposed that T'' phase may have unique cation ordering in the Ln-O layer and interlayer ordering at the $\text{Ln}_3\text{Ln}'$ composition. In order to see any $\text{La}_3\text{Pr}(\text{Nd})$ interlayer ordering, SAED was studied, but any superstructure or specific cation ordering for this T'' phase wasn't found.

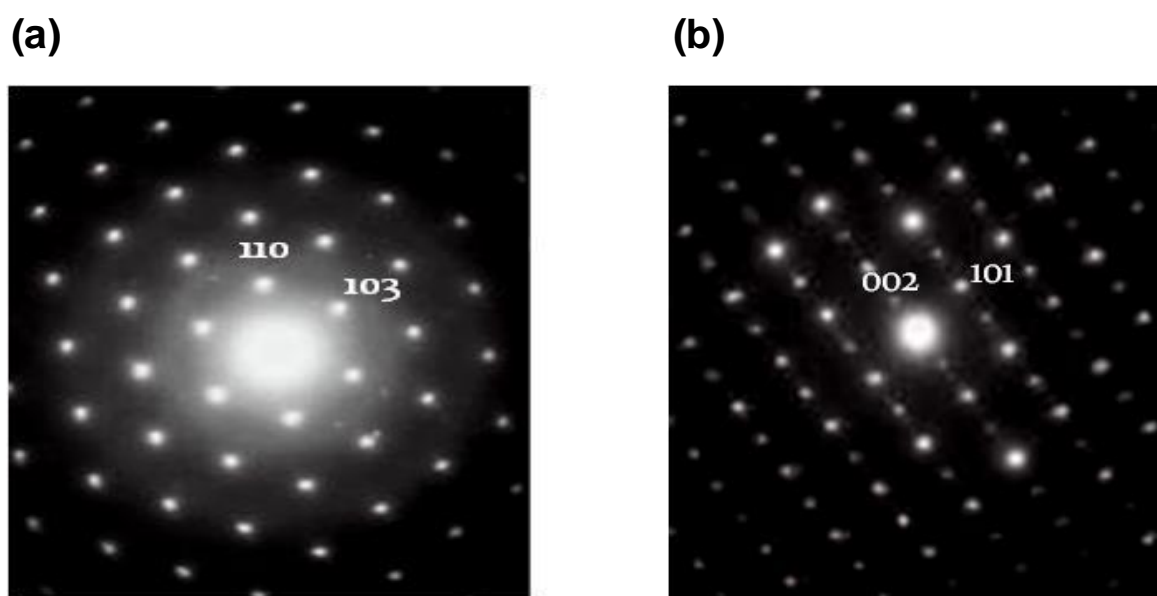


Figure 5.10: SAED patterns for T'' phase at room temperature viewed down the $\bar{3}31$ (a) and $0\bar{1}0$ (b)

SAED patterns are in agreement with the NPD studies. Figure 5.10(a-b) shows a typical SAED pattern of the 4 coordinated tetragonal phase viewed down from two different directions $\bar{3}31$ and $0\bar{1}0$. The phase is indexed according to the cell parameters from the d -spacings of the pattern and angle between each plane. The oxygen content of all the T'' phase was also determined by thermogravimetric analysis (figure 5.11). There is no significant mass change in the TGA under air, as the oxygen content doesn't change significantly T to T'' phase. In order to calculate the δ values thermogravimetric analysis under 5% hydrogen /

95% argon heating up to 1000 °C were carried out. TGA with reduction in two steps. Copper is reduced via Cu(I) to Cu⁰. Final XRD diffraction studies also confirmed that Cu(II) was reduced to metallic copper. Again a $\delta \approx 0.030(8)$ ($\text{Nd}_{0.35}\text{La}_{1.45}\text{Pr}_{0.2}\text{CuO}_{3.97}$) value was obtained from detected mass loss which agrees with neutron diffraction studies.

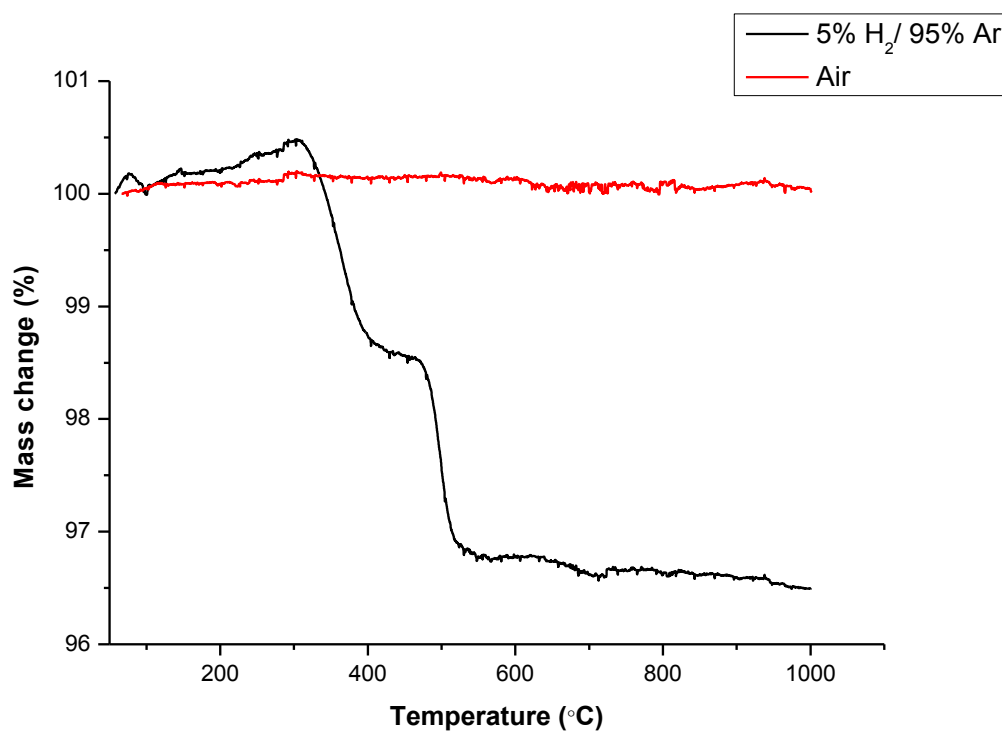


Figure 5.11: Thermogravimetric analysis under air and 5% hydrogen/95% argon heating up to 1000 °C

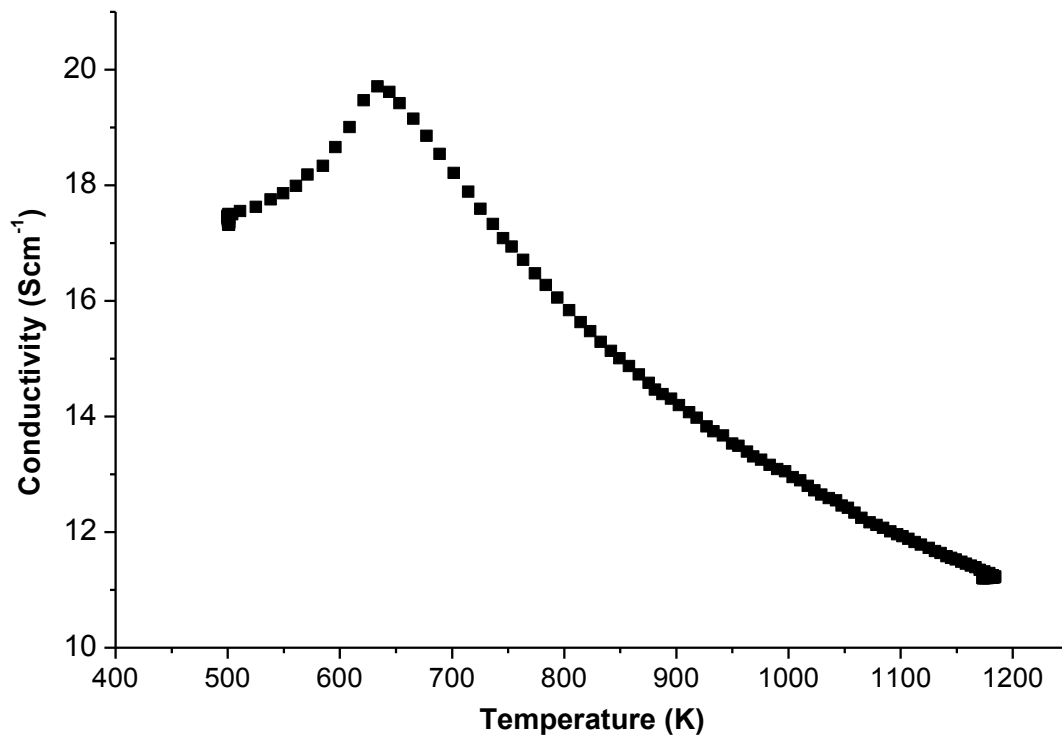


Figure 5.12: DC conductivity measurements for $\text{Nd}_{0.35}\text{La}_{1.45}\text{Pr}_{0.2}\text{CuO}_4$

In-situ conductivity measurements were carried out for this composition (figure 5.12) above 200°C. $\text{Nd}_{0.35}\text{La}_{1.45}\text{Pr}_{0.2}\text{CuO}_4$ shows metallic behaviour at higher temperatures with semiconductor to metallic transition at 360°C, although this also relates to T to O phase transition. Ceramic pellets going through O to T'' transition transform to fine powder around 200°C. Therefore to avoid this transition the pellet was taken out from the jig at 220°C. Compared to La rich compositions, $\text{Nd}_{0.35}\text{La}_{1.45}\text{Pr}_{0.2}\text{CuO}_4$ composition (with the phases T'+O at room temperature) is more conductive (3 Scm^{-1}) at room temperature, the highest conductivity (19.7 Scm^{-1}) is reached around 360°C. This behaviour is similar to the undoped p-type T phase (La_2CuO_4). But for the higher Nd containing compositions, T phase is more conductive compared to the higher La containing T phase.

5.3 Conclusions

The T'' form has previously been suggested as an ordered form of T' ; however here we show via high temperature X-ray diffraction studies that it is a non-transformable metastable phase formed on quenching of the T phase via an orthorhombically distorted variant. Although $\text{Nd}_{0.35}\text{La}_{1.45}\text{Pr}_{0.2}\text{CuO}_{3.97}$ has a high Nd content, which would tend to stabilise T' formation, it exists as pure T phase at high temperature. This then transforms to T'' on cooling to low temperatures (*ca* 200 °C). This final transition is accompanied by a very large change in unit cell parameters, resulting from the large difference in c/a ratio between T and T'' phase. The T'' phase has tetragonal symmetry and is very similar to the T' type structure but with quite different unit cell parameters. Due to significant volume change upon cooling, the sintered ceramic pellet of the T'' phase transforms into fine powder (*ca* 5 microns) within few minutes at room temperature due to this phase transition (O to T'').

Rietveld refinement profile of NPD and SAED data confirm that T'' contains 4-fold Cu coordination. Neutron diffraction and thermogravimetric analysis measurements show that oxygen deficient (δ) in T'' is about 0.03.

Chapter 6- Conclusions

Current SOFC cathode materials have advantages as well as disadvantages as described in section 1.2, to investigate new materials and to optimize current materials is always key issue to enhance the efficiency of SOFC. Therefore the major target of this project was to investigate the performance of cuprate based material as a SOFC candidate. Especially with the n-type based material as a SOFC cathode to enhance the performance in mild oxygen deficiency. Therefore $\text{Nd}_{2-x}\text{Pr}_x\text{CuO}_4$ were prepared with the dopant level $x=0.15, 0.20$ and 0.25 and then electrochemical performance were investigated. Summarising overall work in this thesis, NPCO shows promising as a SOFC cathode material due to its high conductivity (NPCO25 shows maximum conductivity 86.7 Scm^{-1} at 900°C), n-type behaviour (increasing the conductivity with decreasing oxygen partial pressure) and stable in oxidising atmosphere. In addition, it is compatible with current SOFC electrolyte materials (CGO and YSZ) as there is no delaminating for the post tested pellet. Composite NPCO cathode showed better performance compared to the pure NPCO cathode with low R_p and low activation energies. In addition to that NPCO was investigated as a current collecting material using pre-fired and in situ-fired current collecting layers. Pre-fired current collecting layer showed overall better performance (low R_p and low activation energies) compared to in-situ current collecting layer. Overall lower activation energy is obtained for NPCO is possibly due to its catalytic activity for the oxygen reduction. This may presumably be due to Pr dual oxidation state.

Second part of this work was to introduce lanthanum in to NPCO system (distort the structure) and investigate the electrochemical performance. Nineteen samples were prepared ($\text{Nd}_{2-x-y}\text{La}_y\text{Pr}_x\text{CuO}_4$) with varying the La content with the increment of 0.1. Interestingly it leads to construct the phase diagram of NLPCO. In-situ XRD was performed up to 1000°C for selected compositions to complete the phase diagram. As shown in Figure 4.16, two

equilibrium phases (T' and O) can be seen at room temperature. Another new phase is appearing where the $La=1.45$ which was previously identified as T'' in the literature. This phase has similar XRD pattern to the T' structure but with larger cell parameters (a and c). Our results indicate that T'' phase is metastable and non transformable, because T'' phase formed as a quenching of T phase. Annealed in low temperature for long time, this T phase undergoes a spinoidal decomposition in to lower and higher Nd content T' and O phases. This T'' phase has no place in equilibrium phase diagram due to its metastability. Reitveld refinements of neutron diffraction data have proved that this T'' phase has four fold Cu coordination similar to T' phase.

Electrochemical performance and magnetic properties were investigated for the selected composition of the NLPCO. Increasing a small La content into the system will increase the conductivity while increasing higher La content lead to decrease the conductivity. T' phase shows n-type semiconductor behaviour while T phase shows p-type metallic behaviour. Superconducivity was not seen for the selected NLPCO compositions for T' and O phases

As a future work, in-situ neutron diffraction analysis for $Nd_{0.35}La_{1.45}Pr_{0.2}CuO_4$ will carry out to understand the movement of oxygen from T to T'' phase with the temperature.

References

- 1) Tao, S. W.; Irvine, J. T. S. *Nat. Mater.* **2003**, 2, 320-323.
- 2) Atkinson, A.; Barnett, S.; Gorte, R. J.; Irvine, J. T. S.; McEvoy, A. J.; Mogensen, M.; Singhal, S. C.; Vohs, J. *Nat. Mater.* **2004**, 3, 17-27.
- 3) Guo, K. W. *Int. J. Energ. Res.* **2012**, 36, 1-17.
- 4) Tao, S. W.; Irvine, J. T. S. *Adv. Mater.* **2006**, 18, 1581-1584.
- 5) Sammer, N.M.; Topsette, G. A.; Phillips, R. J. *Solid State Ion.* **1998**, 111, 1-7.
- 6) Ssen, Z. *Prog. Energ. Combust.* **2004**, 30, 367-416.
- 7) Sun, L. P.; Huo, L. H.; Zhao, H.; Li, Q.; Pijolat, C. *J. Power Sources.* **2008**, 179, 96-100.
- 8) Tietz, F.; Buchkremer, H. P.; Stover, D. *Solid State Ion.* **2002**, 152, 373-381.
- 9) Jegannathan, K. R.; Abang, S.; Poncelet, D.; Chan E. S.; Ravindra, P.; *Crit.Rev. Biotechnol.* **2008**, 28, 253-264.
- 10) Lam, M. K.; Lee, K. T.; *Biotechnol.Adv.* **2011**, 29, 124-141.
- 11) Krishnan, A.; Lu, X. G.; Pal, U. B. *Scand J. Metall*, **2005**, 34, 293-301.
- 12) Savaniu, C. D.; Irvine, J. T. S. *J. Mater. Chem.* **2009**, 19, 8119-8128.
- 13) Kim, J. H.; Cassidy, M.; Irvine, J. T. S.; Bae, J. *Chem. Mat.* **2010**, 22, 883-892.
- 14) EG&G Technical services, Inc., *Fuel cell Handbook seventh Edition*, National energy technology laboratory, 2004.
- 15) Hirschenhofer, J.H.; Sauffer, D.B.; Engleman, R.R.; Klett, M.G.; *Fuel Cell Handbook*, US Department of Energy, Morgantown, WV, 1998.
- 16) Nagamoto, H.; Cai, Z. H.; *Electrochemical Society Inc.* **1999**, 99, 163-171.
- 17) Swartz, S. L.; Seabaugh, M. M.; Dawson, W. J.; *Electrochemical Society Inc.* **1999**, 99.

- 18) Singhal, S.C.; Kendall, K.; High Temperature Solid Oxide Fuel Cells: Fundamentals, Design and Applications, Elsevier, Oxford, UK. 2003.
- 19) Singhal, S. C. *MRS Bull.* **2000**, *25*, 16-21.
- 20) Zhu, W. Z.; Deevi, S. C. *Mater. Sci. Eng. A-Struct. Mater. Prop. Microstruct. Process.* **2003**, *362*, 228-239.
- 21) Park, S. D.; Vohs, J. M.; Gorte, R. J. *Nature* **2000**, *404*, 265-267.
- 22) Adler, S. B. *Chem. Rev.* **2004**, *104*, 4791-4843.
- 23) Minh, N.Q.; Takahashi, T. Science and Technology of Ceramic Fuel Cells, Elsevier Science B.V: Amsterdam; 1995.
- 24) Yamamoto, O.; Takeda, Y.; Kanno, R.; Noda, M. *Solid State Ion.* **1987**, *22*, 241-246.
- 25) Clausen, C.; Bagger, C.; Bildesorensen, J. B.; Horsewell, A. *Solid State Ion.* **1994**, *70*, 59-64.
- 26) Kenjo, T.; Nishiya, M. *Solid State Ion.* **1992**, *57*, 295-302.
- 27) Esquirol, A.; Kilner, J.; Brandon, N. *Solid State Ion.* **2004**, *175*, 63-67.
- 28) Figueiredo, F. M.; Labrincha, J. A.; Frade, J. R.; Marques, F. M. B. *Solid State Ion.* **1997**, *101*, 343-349.
- 29) Yamamoto O.; Takeda Y.; Kanno R.; Noda, M. *Solid States Ion.* **1987**, *22*, 241–246.
- 30) Kuscer, D.; Holc, J.; Hrovat, M.; Bernik, S.; Samardzija, Z.; Kolar, D. *Solid State Ion.* **1995**, *78*, 79-85.
- 31) Ishihara, T.; Honda, M.; Shibayama, T.; Minami, H.; Nishiguchi, H.; Takita, Y. *J. Electrochem. Soc.* **1998**, *145*, 3177-3183.
- 32) Ishihara, T.; Fukui, S.; Nishiguchi, H.; Takita, Y. *Solid State Ion.* **2002**, *152*, 609-613.
- 33) Hartley, A.; Sahibzada, M.; Weston, M.; Metcalfe, I. S.; Mantzavinos, D. *Catal. Today* **2000**, *55*, 197-204.
- 34) Siebert, E.; Hammouche, A.; Kleitz, M. *Electrochim. Acta.* **1995**, *40*, 1741-1753.

- 35) Steele, B. C. H. *Solid State Ion.* **1996**, 86-88, 1223-1234.
- 36) Juhl, M.; Primdahl, S.; Manon, C.; Mogensen, M. *J. Power Sources.* **1996**, 61, 173-181.
- 37) Matsuzaki, Y.; Yasuda, I. *Solid State Ion.* **1999**, 126, 307-313.
- 38) VanHerle, J.; McEvoy, A. J.; Thampi, K. R. *Electrochim. Acta.* **1996**, 41, 1447-1454.
- 39) Mitterdorfer, A.; Gauckler, L. J. *Solid State Ion.* **1998**, 111, 185-218.
- 40) Baur, E.; Preis, H. *Z. Elektrochem. Angew. Phys. Chem.* **1937**, 43, 727-732.
- 41) Kharton, V. V.; Viskup, A. P.; Kovalevsky, A. V.; Naumovich, E. N.; Marques, F. M. B. *Solid State Ion.* **2001**, 143, 337-353.
- 42) Wang, S.; Kato, T.; Nagata, S.; Kaneko, T.; Iwashita, N.; Honda, T.; Dokiya, M. *Solid State Ion.* **2002**, 152, 477-484.
- 43) Liu, X. L.; Ma, J. F.; Hou, W. H.; Gao, J.; High-Performance Ceramics 2001 (Key Engineering Materials), Trans Tech Publishing Ltd., Zurich, Switzerland, 2002.
- 44) Maffei, N.; Kuriakose, A. K. *Solid State Ion.* **1998**, 107, 67-71.
- 45) Eguchi, K.; Setoguchi, T.; Inoue, T.; Arai, H. *Solid State Ion.* **1992**, 52, 165-172.
- 46) Matsuzaki, Y.; Yasuda, I. *J. Electrochem. Soc.* **2001**, 148, A126-A131.
- 47) Ralph, J. M.; Kilner, J. A.; Steele, B. C. H. In *New Materials for Batteries and Fuel Cells*; Doughty, D. H., Nazar, L. F., Arakawa, M., Brack, H. P., Naoi, K., Eds.; Materials Research Society: Warrendale, **2000**; 575, 309-314.
- 48) Steele, B. C. H. *Solid State Ion.* **2000**, 134, 3-20.
- 49) Lashtabeg, A.; Skinner, S. J. *J. Mater. Chem.* **2006**, 16, 3161-3170.
- 50) McEvoy, A. J. *Solid State Ion.* **2000**, 135, 331-336.
- 51) Richter, J.; Holtappels, P.; Graule, T.; Nakamura, T.; Gauckler, L. J. *Mon. Chem.* **2009**, 140, 985-999.
- 52) Skinner, S. J.; Kilner, J. A.; *Ionics* **1999**, 5, 171-174.

- 53) Skinner, S. J.; Kilner, J. A. *Solid State Ion.* **2000**, *135*, 709-712.
- 54) Vashook, V. V.; Yushkevich, II; Kokhanovsky, L. V.; Makhnach, L. V.; Tolochko, S. P.; Kononyuk, I. F.; Ullmann, H.; Altenburg, H. *Solid State Ion.* **1999**, *119*, 23-30.
- 55) Kharton, V. V.; Viskup, A. P.; Kovalevsky, A. V.; Naumovich, E. N.; Marques, F. M. B. *Solid State Ion.* **2001**, *143*, 337-353.
- 56) Singhal, S. C. *Solid State Ion.* **2000**, *135*, 305-313.
- 57) Skinner, S. J. *Int. J. Inorg. Mater.* **2001**, *3*, 113-121.
- 58) Ishihara, T.; Kudo, T.; Matsuda, H.; Takita, Y. *J. Am. Ceram. Soc.* **1994**, *77*, 1682-1684.
- 59) Sakaki, Y.; Takeda, Y.; Kato, A.; Imanishi, N.; Yamamoto, O.; Hattori, M.; Iio, M.; Esaki, Y. *Solid State Ion.* **1999**, *118*, 187-194.
- 60) Rim, H. R.; Jeung, S. K.; Jung, E.; Lee, J. S. *Mater. Chem. Phys.* **1998**, *52*, 54-59.
- 61) Weber, A.; Ivers-Tiffée, E. *J. Power Sources.* **2004**, *127*, 273-283.
- 62) Simner, S. P.; Bonnett, J. R.; Canfield, N. L.; Meinhardt, K. D.; Shelton, J. P.; Sprenkle, V. L.; Stevenson, J. W. *J. Power Sources.* **2003**, *113*, 1-10.
- 63) Ralph, J. M.; Rossignol, C.; Kumar, R. *J. Electrochem. Soc.* **2003**, *150*, A1518-A1522.
- 64) Shaked, H.; Keane, P.M.; *etal.* Crystal structure of the High-Tc Superconducting copper –oxides, Elsevier Science B.V: Netherlands, **1994**.
- 65) Mauvy, F.; Bassat, J. M.; Boehm, E.; Dordor, P.; Loup, J. P. *Solid State Ion.* **2003**, *158*, 395-407.
- 66) Boehm, E.; Bassat, J. M.; Steil, M. C.; Dordor, P.; Mauvy, F.; Grenier, J. C. *Solid State Sci.* **2003**, *5*, 973-981.
- 67) Kilner, J. A.; Shaw, C. K. M. *Solid State Ion.* **2002**, *154*, 523-527.

- 68) Munnings, C. N.; Skinner, S. J.; Amow, G.; Whitfield, P. S.; Davidson, I. J. *Solid State Ion.* **2005**, *176*, 1895-1901.
- 69) Boehm, E.; Bassat, J. M.; Dordor, P.; Mauvy, F.; Grenier, J. C.; Stevens, P. *Solid State Ion.* **2005**, *176*, 2717-2725.
- 70) Mauvy, F.; Lalanne, C.; Bassat, J. M.; Grenier, J. C.; Zhao, H.; Dordor, P.; Stevens, P. *J. European Ceram. Soc.* **2005**, *25*, 2669-2672.
- 71) Bassat, J. M.; Odier, P.; Villesuzanne, A.; Marin, C.; Pouchard, M. *Solid State Ion.* **2004**, *167*, 341-347.
- 72) Minervini, L.; Grimes, R. W.; Kilner, J. A.; Sickafus, K. E. *J. Mater. Chem.* **2000**, *10*, 2349-2354.
- 73) Buttrey, D. J.; Ganguly, P.; Honig, J. M.; Rao, C. N. R.; Scharfman, R. R.; Subbanna, G. N. *J. Solid State Chem.* **1988**, *74*, 233-238.
- 74) Jiang, S. P.; Zhang, J. P.; Zheng, X. G. *J. European Ceram. Soc.* **2002**, *22*, 361-373.
- 75) Fletcher, J. G.; Irvine, J. T. S.; West, A. R.; Labrincha, J. A.; Frade, J. R.; Marques, F. M. B. *Mater. Res. Bull.* **1994**, *29*, 1175-1182.
- 76) Manthiram, A.; Goodenough, J. B. *J. Solid State Chem.* **1990**, *87*, 402-407.
- 77) Goodenough, J. B.; Manthiram, A. *J. Solid State Chem.* **1990**, *88*, 115-139.
- 78) Prijamboedi, B.; Kashiwaya, S.; Sawa, A.; Tanaka, Y. *Physica C.* **2002**, *378*, 386-389.
- 79) Jansen, L.; Block, R. *Physica A.* **1999**, *271*, 169-191.
- 80) Vigoureux, P.; Paulus, W.; Henry, J. Y.; Pinol, S.; Heger, G. *Physica B.* **1997**, *234*, 719-720.
- 81) Spinolo, G.; Scavini, M.; Ghigna, P.; Chiodelli, G.; Flor, G. *Physica C.* **1995**, *254*, 359-369.

- 82) Cassidy, M.; Irvine, J. T. S. In *Solid Oxide Fuel Cells 10*; Eguchi, K., Singhai, S. C., Yokokawa, H., Mizusaki, H., Eds.; Electrochemical Society Inc: Pennington, **2007**; 7,1235-1241.
- 83) Ganguly, P.; Rao, C. N. R. *J. Solid State Chem.* **1984**, *53*, 193-216.
- 84) Pillai, C. G. S.; George, A. M. *Int. J. Thermophys.* **1986**, *7*, 1091-1100.
- 85) Ganguly, P.; Rao, N. R. *Mater. Res. Bull.* **1973**, *8*, 405-412.
- 86) Smolenskii, G. A.; Yudin, V. M.; Sherr, E. S. *Soviet Physics-Solid State.* **1963**, *4*, 2452-2454.
- 87) Puche, R. S.; Norton, M.; Glaunsinger, W. S. *Mater. Res. Bull.* **1982**, *17*, 1523-1530.
- 88) Puche, R. S.; Norton, M.; White, T. R.; Glaunsinger, W. S. *J. Solid State Chem.* **1983**, *50*, 281-293.
- 89) Longo, J. M.; Racciah, P. M. *J. Solid State Chem.* **1973**, *6*, 526-531.
- 90) Goodenough, J. B.; Ramasesha, S. *Mater. Res. Bull.* **1982**, *17*, 383-390.
- 91) Manthiram, A.; Goodenough, J. B. *J. Solid State Chem.* **1991**, *92*, 231-236.
- 92) Tao, Y. K.; Sun, Y. Y.; Paredes, J.; Hor, P. H.; Chu, C. W. *J. Solid State Chem.* **1989**, *82*, 176-178.
- 93) Lappas, A.; Prassides, K. *J. Solid State Chem.* **1995**, *115*, 332-346.
- 94) Bringley, J. F.; Trail, S. S.; Scott, B. A. *J. Solid State Chem.* **1990**, *86*, 310-322.
- 95) Bringley, J. F.; Trail, S. S.; Scott, B. A. *J. Solid State Chem.* **1990**, *88*, 590-593.
- 96) Vanderah, T.A, Chemistry of superconductor materials, Noyes Publications, New Jersey, 1992.
- 97) Mullerbuschbaum, H.; Wollschlager, W. *Z. Anorg. Allg. Chem.* **1975**, *414*, 76-80.
- 98) Tokura, Y.; Takagi, H.; Uchida, S. *Nature.* **1989**, *337*, 345-347.
- 99) Cheong, S. W.; Thompson, J. D.; Fisk, Z. *Physica C.* **1989**, *158*, 109-126.

- 100) Tarascon, J. M.; Greene, L. H.; McKinnon, W. R.; Hull, G. W.; Geballe, T. H. *Science*. **1987**, *235*, 1373-1376.
- 101) Bednorz, J.B.; Miiller, K.A. *Z. Phys.* **1986**, *B64*, 189.
- 102) Terrance, J. B.; Bezing, A.; Nazzari, A. I.; Huang, T. C.; Parkin, S. S. P.; Keane, D. T.; Laplace, S. J.; Horn, P. M.; Held, G. A. *Phys. Rev. B*. **1989**, *40*, 8872-8877.
- 103) Axe, J.D.; Moudden, A. H.; Hohlwein, D.; Cox, D. E.; Mohanty, K. M.; Moodenbaugh, A. R.; Xu, Y. W. *Phys. Rev. Lett.* **1989**, *62*, 2751-2754.
- 104) Subramanian, M. A.; Gopalakrishnan, J.; Torardi, C. C.; Askew, T. R.; Flippen, R. B.; Sleight, A. W.; Lin, J. J.; Poon, S. J. *Science*. **1988**, *240*, 495-497.
- 105) Kenjo, T.; Yajima, S. *Bull. Chem. Soc. Jpn.* **1977**, *50*, 2847-2850.
- 106) Lightfoot, P.; Pei, S.; Jorgensen, J. D.; Tang, X. X.; Manthiram, A.; Goodenough, J. B. *Physica C*. **1990**, *169*, 15-22.
- 107) Maeno, Y.; Lichtenberg, F.; Williams, T.; Karpinski, J.; Bednorz, J. G. *Jpn. J. Appl. Phys. Part 2 - Lett.* **1989**, *28*, L926-L929.
- 108) Ikeda, Y.; Yamada, K.; Kusano, Y.; Takada, J. *Physica C*. **2002**, *378*, 395-398.
- 109) Fujita, T.; Maeno, Y.; *Physica C*. **1988**, *152*, 121.
- 110) Jorgensen, J. D.; Dabrowski, B.; Pei, S. Y.; Hinks, D. G.; Soderholm, L.; Morosin, B.; Schirber, J. E.; Venturini, E. L.; Ginley, D. S. *Phys. Rev. B*. **1988**, *38*, 11337-11345.
- 111) James, A.; Zahurak, S. M.; Murphy, D. W. *Nature*. **1989**, *338*, 240-241.
- 112) Kwei, G. H.; Cheong, S. W.; Fisk, Z.; Garzon, F. H.; Goldstone, J. A.; Thompson, J. D. *Phys. Rev. B* **1989**, *40*, 9370-9373.
- 113) Takayamamuro-machi, E.; Izumi, F.; Uchida, Y.; Kato, K.; Asano, H. *Physica C*. **1989**, *159*, 634-638.
- 114) Aronson, M. C.; Cheong, S. W.; Garzon, F. H.; Thompson, J. D.; Fisk, Z. *Phys. Rev. B*. **1989**, *39*, 11445-11448.

- 115) Soorie, M.; Skinner, S.J. *Solid State Ionics*. **2006**, *177*, 2081-2086.
- 116) Singh, K. K.; Ganguly, P.; Rao, C. N. R. *Mater. Res. Bull.* **1982**, *17*, 493-500.
- 117) Wang, E.; Tarascon, J. M.; Greene, L. H.; Hull, G. W.; McKinnon, W. R. *Phys. Rev. B*. **1990**, *41*, 6582-6590.
- 118) Mombro, A. W.; Lappas, A.; Prassides, K. *J. Solid State Chem.* **1998**, *140*, 345-349.
- 119) Wilhelm, H.; Cros, C.; Reny, E.; Demazeau, G.; Hanfland, M. *J. Solid State Chem.* **2000**, *151*, 231-240.
- 120) Bragg W.L.; *The Crystalline State*. **1934**, *1*, 229.
- 121) Rietveld, H. M.; *Acta Crystallographica*. **1967**, *22*, 151-152.
- 122) Rietveld, H. M.; *J. Appl. Crystallogr.* **1969**, *2*, 65-71.
- 123) Rodriguez-Carvajal, J.; *Physica B*. **1993**, *192*, 55
- 124) Larson, A.C.; Dreele, R.B.V.; Technical Report LANSCE, MSH805, Los Alamos National Laboratory, 1985.
- 125) Van der Pauw , L.J. ; *Philips Tech.Rev.* **1958**, *20*, 220-224 .
- 126) Van der Pauw, L.J.; *Philips Res.Rep.* **1958**, *13*, 1-9.
- 127) Irvine, J.T.S.; Sinclair D.C.; West A.R.; *Adv.Mater.* **1990**, *2*, 132-138.
- 128) Bauerle, J. E.; *J. Phys. Chem. Solids*. **1969**, *30*, 2657-.2670.
- 129) Jorgensen, M. J.; Mogensen, M. *J. Electrochem. Soc.* **2001**, *148*, A433-A442.
- 130) Rosseinsky, M. J.; Prassides, K.; Day, P. *Inorg. Chem.* **1991**, *30*, 2680-2687.
- 131) Grande, B.; Mullerbuschbaum, H.; Schweizer, M. *Z. Anorg. Allg. Chem.* **1977**, *428*, 120-124
- 132) George, A.M.; Gopalakrishnan, I.K.; Karhanavala, M.D. *Mat.Res.Bull.* **1979**, *9*, 721-.
- 133) Longo, J. M.; Racciah, P. M. *J.Solid State Chem.* **1973**, *6*, 526
- 134) Luke, G. M.; Le, L. P.; Sternlieb, B. J.; *etal. Phys. Rev. B*. **1990**, *42*, 7981-7988
- 135) Gibson, I. R.; Irvine, J. T. S. *J. Am. Ceram. Soc.* **2001**, *84*, 615-618.

136) Scott, H. G. *J. Mater. Sci.* **1975**, *10*, 1527-1535.